U.PORTO

FEUP FACULDADE DE ENGENHARIA
UNIVERSIDADE DO PORTO

FATIGUE BEHAVIOR OF COLD ROLL-FORMED Z-RAILS FOR RACK STRUCTURES

Carlos Daniel Santos Souto

Dissertation submitted to the
Faculty of Engineering of the University of Porto
for the academic degree of
Master in Computational Mechanics

Supervisor
Prof. Dr. Abílio de Jesus

Co-Supervisors
Dr. José Correia
Eng. Vítor Gomes

Faculty of Engineering of the University of Porto

Porto, 2020

Carlos Daniel Santos Souto

E-mail: csouto@fe.up.pt

ABSTRACT

Nowadays, in the field of logistics engineering, rack structures are prepared to deal with the logistics of large warehouses, where automatic shuttles are responsible for the intensive transportation and storage of various goods and products. In order to move through the rack structure, these shuttles run on cold-formed steel rails. Since these shuttles are usually automated, they can work non-stop (24 hours a day, 7 days a week), and as a consequence of this, the rails are subjected to cyclic loading caused by the passage of shuttles. Because of this, the rails experience fatigue phenomena, moreover, cracks due to material fatigue have already been observed in these types of rails.

The mentioned rails are fabricated through the cold roll-forming fabrication process. In this process, the forming of the material to obtain the final product occurs at room temperatures, much lower than the required temperatures for material recrystallization. On effect, this manufacturing process leaves in the rail internal residual stresses that may play a role in the fatigue performance of these types of elements.

To ensure safety inside a warehouse that contains a rack structure, design codes should include fatigue design curves for these types of structural elements. Currently, the Eurocode 3 does not cover the fatigue behavior of thin cold-formed elements, like the mentioned rails. The Eurocode 3 does cover the subject of thick hot-rolled sections; however, due to material recrystallization, residual stresses are not relevant in these types of structural elements.

In this background, the FASTCOLD project arises with the aim to develop fatigue design rules for cold-formed steel members and their connections. The project also aims to provide a classification of cold-formed structural steel details according to their fatigue strength, similar to the ones from Eurocode 3 for thick hot-rolled steel details.

Some of these cold-formed structural details are of general use in steel structures, while others are specific for applications in rack structures. Nowadays, rack structures are the most relevant industrial application of cold-formed steel details under fatigue loading. However, cold-formed members appear in other engineering fields, like the automotive industry and the railway industry. For this reason, although the FASTCOLD project is aimed at solving relevant problems in the industrial sector of logistics, the research can be further extended to other engineering fields where cold-formed structural elements are used.

This dissertation shares the scope of the FASTCOLD project. In the present work, the fatigue behavior of a specific rail, the Z-rail, is investigated. For this, a new experimental fatigue testing setup for full scale fatigue tests on Z-rail specimens was created at the Faculty of Engineering of the University of Porto. The cold roll-forming fabrication process was also numerically simulated to analyze the residual stresses on the Z-rail. Finally, both stress and fatigue analyses were conducted on this rail to obtain insight on its structural performance and to generate S-N fatigue design curves.

Using the mentioned fatigue testing setup, experimental lifetimes (in terms of number of load cycles endured) were determined for Z-rail specimens, allowing the construction of S-N fatigue design curves, and aiming for the classification of this detail ($\Delta\sigma_C$ and m parameters from Eurocode 3).

The quality of residual stress results obtained through numerical simulations was validated by comparing to residual stress results obtained through experimental procedures.

Finally, the conducted stress analysis on the Z-rail, in the form of a parametric study, presents mathematical equations that facilitate the stress range computation for the construction of S-N curves.

Keywords – Rack Structures; Cold Roll-Forming; Residual Stresses; Fatigue Testing; Stress Analysis; Rail Profiles; Finite Element Analysis.

To my family…

"If I have seen further it is by standing on the shoulders of Giants."

Letter from Isaac Newton to Robert Hooke, 1675

ACKNOWLEDGEMENTS

CONTENTS

LIST OF FIGURES

VIII

Appendix A

Appendix B

Appendix C

Appendix D

Appendix E

Appendix F

LIST OF TABLES

NOMENCLATURE

b	Empirically determined material constant (Coffin-Manson life prediction)
c	Empirically determined material constant (Coffin-Manson life prediction)
d	Distance
e	Nominal strain
m	Inverse slope of fatigue design/strength curve
n	Empirically determined material constant (Swift law)
t	Thickness
E	Young's modulus
K	Empirically determined material constant (Swift law)
L	Length
M	Moment of force
N	Lifetime in terms of number of load cycles endured
P	Load magnitude
R	Load ratio, stress ratio, or radius
R^2	Coefficient of determination
S_1^{max}	Maximum value of the maximum principal stresses
ε	True strain
ε_0	Empirically determined material constant (Swift law)
ε_f'	Empirically determined material constant (Coffin-Manson life prediction)
ε_p	True plastic strain
μ	Friction coefficient
ν	Poisson's ratio
σ	True stress
σ_0	Nominal stress
σ_a	Stress amplitude in the load cycle
σ_{avg}	Average stress
σ_f'	Empirically determined material constant (Coffin-Manson life prediction)
σ_m	Mean stress in the load cycle
σ_{max}	Maximum stress in the load cycle
σ_{min}	Minimum stress in the load cycle
σ_{yield}	Yield stress
$\Delta\varepsilon$	Strain range in the load cycle
$\Delta\sigma$	Stress range in the load cycle
$\Delta\sigma_C$	Detail category
$\Delta\sigma_D$	Constant amplitude fatigue limit

$\Delta\sigma_L$ Cut-off limit

Acronyms

BVP   Boundary Value Problem
CPU   Central Processing Unit
FDM   Finite Difference Method
FEA   Finite Element Analysis
FEM   Finite Element Method
HD   Hole Drilling
PDE   Partial Differential Equation
SIF   Stress Intensity Factor
XRD   X-Ray Diffraction

D   Used in tables to denote a **D**ownward loading scenario
S-N   Stress range vs. lifetime in terms of number of load cycles endured
U   Used in tables to denote an **U**pward loading scenario
ε-N   Strain range vs. lifetime in terms of number of load cycles endured

CHAPTER 1: INTRODUCTION

1.1. Background

Nowadays, in the field of logistics engineering, rack structures prepared for automatic shuttles are designed to deal with the logistics of large warehouses, where these shuttles are responsible for the transportation and storage of various goods and products. In order to move through the rack structure, these shuttles run on steel rails, which are usually produced from thin metal sheets that are cold roll-formed into a specific section. Since the shuttles are usually automated, they can work non-stop, 24 hours a day, 7 days a week, and as a consequence of this, the rails are subjected to cyclic loading caused by the passage of the shuttles. Because of this cyclic loading, the rails are susceptive to fatigue phenomena, on effect, cracks due to material fatigue are being observed in these types of rails. The current situation is also aggravated due to the competitiveness of the European industrial sector, which is pushing the design of these rails to lower thicknesses, further increasing concerns about their fatigue performance.

To ensure safety inside a warehouse that contains a rack structure, design codes should include fatigue design curves for these types of structural elements. Currently, the Eurocode 3 (EN1993-1-9, 2014) does not cover the fatigue behavior of thin cold-formed elements, like the mentioned rails. These thin cold-formed elements have residual stresses left over from their fabrication process that may play a role in their fatigue performance. The Eurocode 3 (EN1993-1-9, 2014) does cover the subject of thick hot-rolled sections, however, the residual stresses are not relevant in these types of structural elements due to material recrystallization.

Within the presented background, the FASTCOLD European project has been carried out, whose research plan consists in developing fatigue design rules for the mentioned applications, which, again, are not covered by existing design codes.

Figure 1 shows an empty rack structure that is prepared for automatic pallet-carrying shuttles. In the figure, it is possible to see the shuttle's tracks (cold-formed steel rails). Figure 2 shows cracking that developed in one of these rails due to material fatigue caused by the passage of shuttles.

Figure 1 - Rack structure prepared for automatic pallet-carrying shuttles.

Figure 2 - Observed cracking due to material fatigue in a cold-formed steel rail.

1.2.   FASTCOLD European Project

The FASTCOLD (**FA**tigue **ST**rength of **COLD**-formed structural steel details) European project is a 48-month long research project funded by the Research Fund for Coal and Steel (RFCS) of the European Commission (FASTCOLD-RFCS, 2020).

The aim of this project is to develop fatigue design rules for cold-formed steel members and their connections, with a specific focus on the field of logistics engineering (i.e. rack structures). The project also aims to provide a classification of cold-formed structural steel details according to their fatigue strength, similar to the ones from Eurocode 3 (EN1993-1-9, 2014) for thick hot-rolled steel details. As stated, considerations for cold-formed elements are missing from said design codes and are needed for present and future demands to account for fatigue in the design of rack structures (FASTCOLD-RFCS, 2020).

Some of the structural details covered by the FASTCOLD project are of general use in steel structures, while other details are specific for applications in rack structures. Nowadays, rack structures are the most relevant industrial application of cold-formed steel details under fatigue loading. However, cold-formed members appear in other engineering fields, like the automotive industry and the railway industry (FASTCOLD-RFCS, 2020).

For the above stated reason, although the FASTCOLD project is aimed at solving relevant problems in the industrial sector of logistics, the research can be further extended to other engineering fields where cold-formed structural elements are used.

The FASTCOLD project relies on close to 20 partners, from universities to industrial and commercial companies. The Faculty of Engineering of the University of Porto worked, in the scope of this dissertation, more relevantly with Fincon Consulting Italia S.r.l., data M Sheet Metal Solutions GmbH, RWTH Aachen University, and the University of Burgos.

1.3.   Objectives

The present work incorporates four main objectives:

1. To develop a new fatigue testing setup for thin cold-formed steel rails in order to obtain full scale fatigue testing data which can be used to build S-N fatigue design curves. Complementary to this objective, numerical simulations replicating said setup must also be carried out in order to identify

2

potential problems. Processing of the experimental data must also be done in order to analyze the fatigue behavior of the rails;

2. To numerically simulate the cold roll-forming fabrication process in order to obtain the mentioned thin cold-formed steel rail with internal residual stresses. The real roll-forming machine must also be used in the numerical simulations in order to obtain the rail with its internal residual stresses as closely as possible to reality. A parametric study must also be carried out to determine what differences in results can arise by changing different parameters in the simulation (for example, using isotropic or kinematic material hardening rules);

3. To execute a stress analysis on the mentioned rail in order to obtain easy-to-use mathematical equations that can be used to relate certain parameters to the obtained stresses caused by structural/fatigue loading. With these equations, one can use them instead of numerically simulate said structural/fatigue loadings, since the latter is a much harder procedure;

4. Finally, to combine the results from the above objectives in a fatigue analysis of the rails. With this analysis, more insight on their fatigue/structural performance can be obtained.

1.4.   Methodology and Planning

For the various presented numerical simulations in this dissertation, the Finite Element Method was applied through the use of commercially available computer programs. In most simulations, Abaqus® was used since it is a very popular option in the academic environment. For the roll-forming simulations, COPRA®, a specialized software for these types of simulations, was used instead.

As mentioned, to obtain experimental fatigue data of the mentioned rails, full scale tests were conducted at the Faculty of Engineering of the University of Porto, made possible by the creation of a new experimental fatigue testing setup.

In order to generate S-N fatigue design curves for the mentioned rails, the experimental fatigue life data was combined with numerical simulations to obtain the relevant stress ranges. The ASTM E739-91 standard was used to obtain the mean S-N curves, the standard deviations, and the coefficients of determination, as well as to establish confidence bands.

The planning of activities was comprised of the following tasks (see Table 1):

- Task 1: Learning and running test simulations on the specialized COPRA® software;
- Task 2: Development of the experimental fatigue testing setup combined with numerical simulations to identify problems with said setup. Gathering and processing of fatigue test data;
- Task 3: Roll-forming simulations and residual stress analysis;
- Task 4: Numerical simulations for the rail's stress analysis (no residual stress considerations);
- Task 5: Fatigue analysis of the rail;
- Task 6: FASTCOLD reports and writing/structuring of this dissertation.

Table 1 - Planning of activities.

	2019									2020					
	Apr	May	Jun	Jul	Aug	Sep	Oct	Nov	Dec	Jan	Feb	Mar	Apr	May	Jun
Task 1	▧	▧	▧	▧	▧										
Task 2						▧	▧	▧	▧	▧					
Task 3					▧	▧						▧	▧	▧	
Task 4													▧	▧	
Task 5														▧	▧
Task 6				▧						▧					▧

1.5.   Dissertation Layout

Chapter 1: Introduction – The background, scope, and objectives of this dissertation, as well as of the FASTCOLD project are presented.

Chapter 2: Literature Review – A literature review is presented, where the reader has the opportunity to delve into the basic and fundamental concepts of the cold roll-forming fabrication process, the fatigue analysis, and the finite element method topics. The understanding of these three topics are crucial in order to follow along this dissertation.

Chapter 3: The Z-Rail – The Z-rail, which is a case study for this whole dissertation, is presented. Its geometric properties are stated, and the elastoplastic properties of its material are defined for further use in FEA models.

Chapter 4: Fatigue Testing Setup for Z-Rails – The complete process of creating and refining the experimental fatigue testing setup for full scale fatigue tests on Z-rail specimens is presented. Obtained experimental fatigue life data is also presented.

Chapter 5: Roll-Forming Simulation of the Z-Rail – The procedures to simulate the cold roll-forming fabrication process to obtain the Z-rail with internal residual stresses are presented. A base finite element analysis model for these simulations is defined and presented, and further parametric studies are conducted on the roll-forming process.

Chapter 6: Z-Rail Stress Analysis - Parametric Study – A stress analysis on the Z-rail is conducted and presented through a parametric study.

Chapter 7: Fatigue Analysis of the Z-Rail – A fatigue analysis on the Z-rail is presented, where S-N curves are shown based on statistical and regression analyses. A Coffin-Manson fatigue life prediction is also presented and compared to experimental results.

Chapter 8: Conclusions – Conclusions are presented about the results of the previous chapters.

CHAPTER 2:   LITERATURE REVIEW

In this chapter, a review on available literature is presented. This review is divided into three sections, each one relative to an important topic in the scope of this dissertation:

- Cold roll-forming fabrication process;
- Structural fatigue analysis;
- Finite element analysis.

2.1.   Cold Roll-Forming Fabrication Process

The metal roll-forming process is a fabrication process used to obtain certain metal parts, like tubes with various sections (e.g. square and circular sections), U-channels, Z-rails, open sections for uprights, and many others. In this process, the raw material, usually in the form of a metal strip, is fed onto a production line where rolls gradually form and shape the initial strip's section to obtain the desired part. Usually, the final product is a metal part with a constant section along its length, however, in more complex production lines, it is possible to obtain parts with a variable section.

The cold roll-forming fabrication process arises as an option to metal roll-forming, where forming occurs below the recrystallization temperature of the material (usually at room temperatures). The alternatives to this process are the warm and hot roll-forming processes, where forming occurs near and above the recrystallization temperature of the material, respectively.

As stated above, in the cold roll-forming fabrication process, forming occurs below the recrystallization temperature of the material, which means that the end product contains internal residual stresses left over from the fabrication process. These residual stresses are usually divided into transversal (due to transversal bending of the strip's section) and longitudinal (due to longitudinal bending of the strip). Moreover, in the cold roll-forming fabrication process, the raw material is usually in the form of a tightly coiled metal strip, further increasing the stress history of the end product. The material suffers various coiling-uncoiling cycles before entering the roll-forming mill.

As stated previously, in the cold roll-forming process, the strip's section is gradually formed. Usually, to achieve this continuous gradual deformation, depicted in Figure 3, the roll-forming machine is divided into stations. Each station usually has at least two horizontal shafts (one on top and another below the strip's location) where rolls are mounted to. Due to the geometry of the rolls, each station is responsible to enforce a specific section on the strip. By superimposing these sections, a roll-forming flower diagram can be created, as shown in Figure 4 (Halmos, 2006).
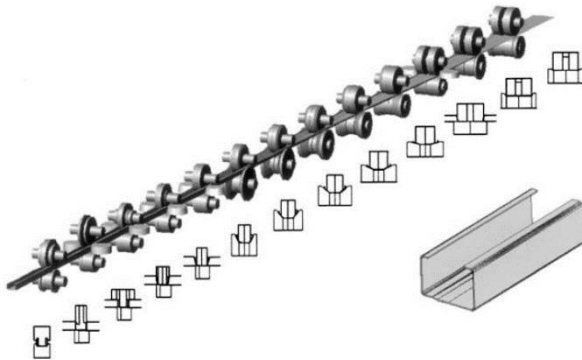
Figure 3 - The cold roll-forming fabrication process where the strip's section is gradually formed (Halmos, 2006).
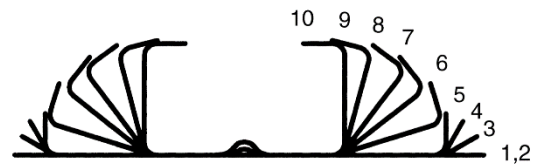
Figure 4 - Roll-forming flower diagram obtained by superimposing the station sections (Halmos, 2006).

In order to save space and tolling/machine costs, the roll-forming machine should have the minimum required number of stations (which is the same as saying: it should have the minimum required number of forming steps). However, if too few stations are used, the final product will be severely distorted, since generated stresses in the material reach unacceptable levels during the process (Figure 5) (Halmos, 2006).
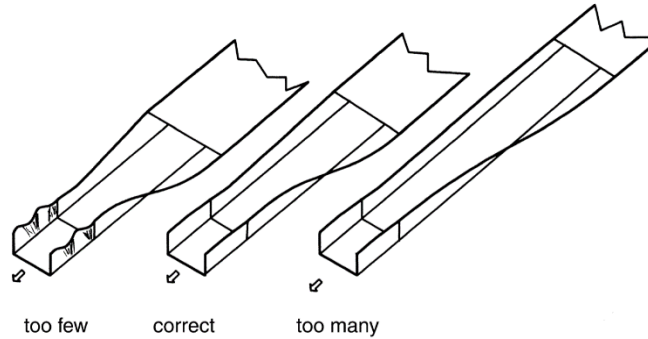
Figure 5 - Too few vs. too many roll-forming steps (Halmos, 2006).

As stated before, in the roll-forming process, the initial metal strip is subjected to various types of deformations. The fundamental deformation of this process is the transversal bending of the strip's section (Figure 6) (Halmos, 2006).
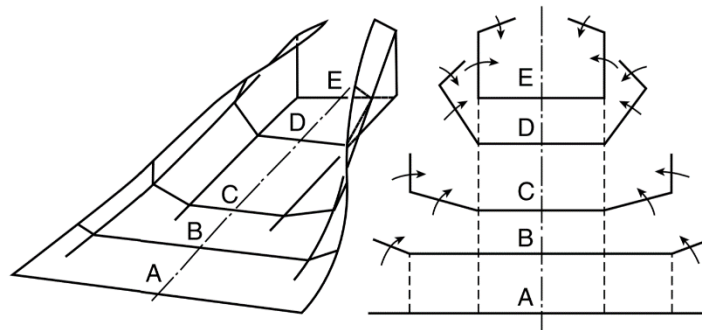
Figure 6 - Transversal bending during the roll-forming process (Halmos, 2006).

As shown in Figure 7, a typical cold roll-forming setup starts off with a coiled metal strip, which is then uncoiled, flattened and fed into the roll-forming mill. This is considered a redundant type of deformation (Halmos, 2006). The coiling and uncoiling processes further increase the complexity of the stress history of the final product. Moreover, a closed-form analytical solution to take into consideration the coiling and uncoiling residual stresses of steel sheets has already been presented (Quach, Teng, & Chung, 2004).
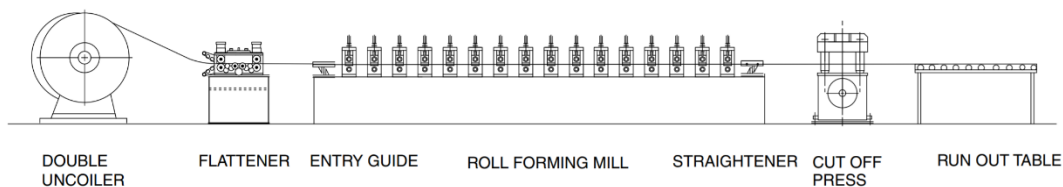
Figure 7 - Typical cold roll-forming setup (Halmos, 2006).

Even without considering the effects of coiling and uncoiling, redundant longitudinal and transversal deformations are still present in the roll-forming fabrication process, as show in Figure 8. These redundant deformations are usually responsible for final defects on the end product (Halmos, 2006).
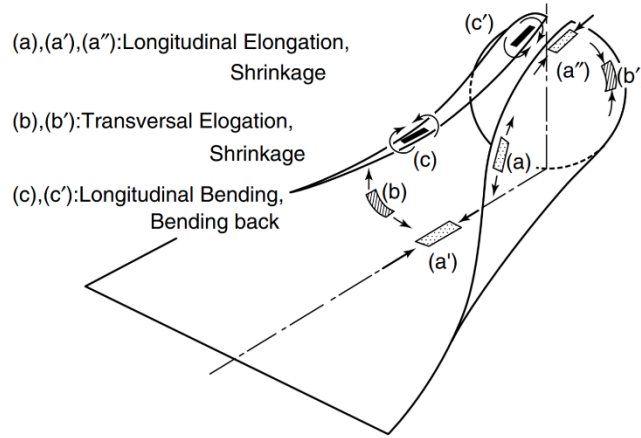
Figure 8 - Redundant deformations during the roll-forming process (Halmos, 2006).

As stated before, redundant deformations are usually responsible for final defects on the end product. The most common defects are shown in Figure 9 (Halmos, 2006).
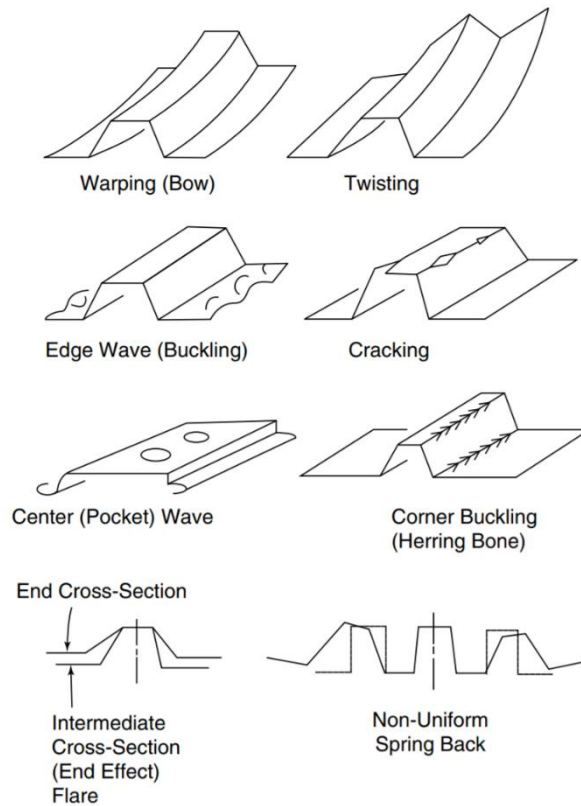
Figure 9 - Common roll-forming defects (Halmos, 2006).

Towards the end of the cold roll-forming process, the continuously deformed strip must be cut into sections of a determined length. This end cut can also induce flaring of the end product (Figure 10) (Halmos, 2006).
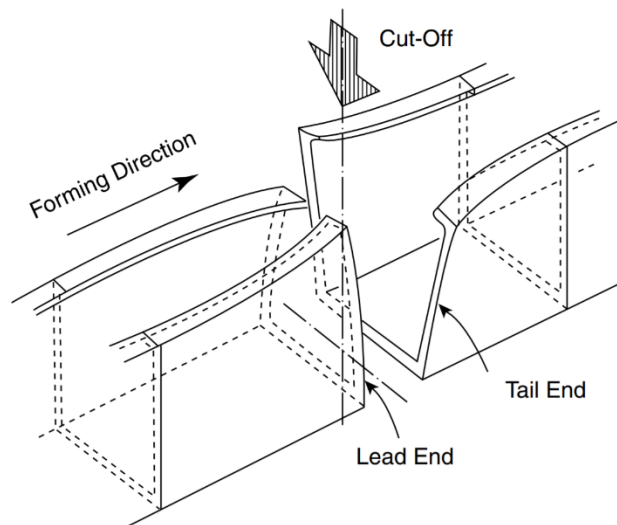
Figure 10 - Flaring due to the end cut on the roll-forming process (Halmos, 2006).

As shown in Figure 11, after the cold roll-forming fabrication process, when the strip is free of the roll's constraints, material spring back can occur and ruin the end-product. Usually, roll-forming machines have stations which induce "over-deformations" on the metal strip to compensate for material spring back (Halmos, 2006).
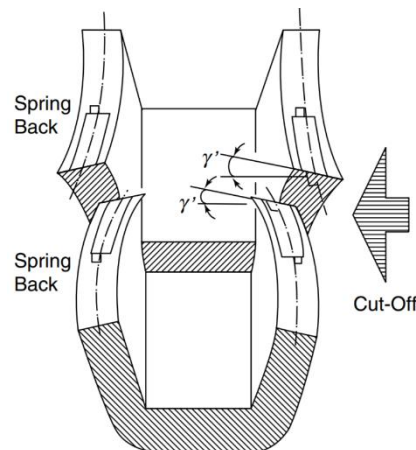
Figure 11 - Material spring back after the end cut (Halmos, 2006).

As stated before, in more complex cold roll-forming production lines, it is possible to obtain parts with a variable cross section. This process is called flexible roll-forming (also known as 3D roll-forming) and it is mostly used in the automotive industry. Even the simplest case study of flexible roll-forming (a variable width U-channel, Figure 12) can be quite a complex problem. In flexible roll-forming, the rolls must be able to translate and/or rotate during forming in order to obtain parts with a variable cross section (Gülçeken, Abeé, Sedlmaier, & Livatyali, 2007).
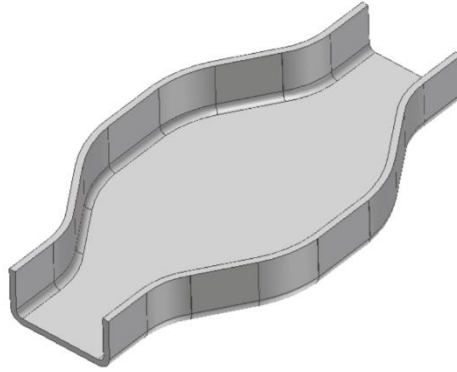
Figure 12 - Variable width U-channel obtained through flexible roll-forming (Gülçeken, Abeé, Sedlmaier, & Livatyali, 2007).

Finally, resorting to finite element analyses, the cold roll-forming fabrication process can be simulated by most well-known commercial FEA programs, like Abaqus®. However, specialized programs like COPRA® make the construction of the FEA model much easier and faster through the automation of various repetitive tasks (Figure 13 to Figure 16).
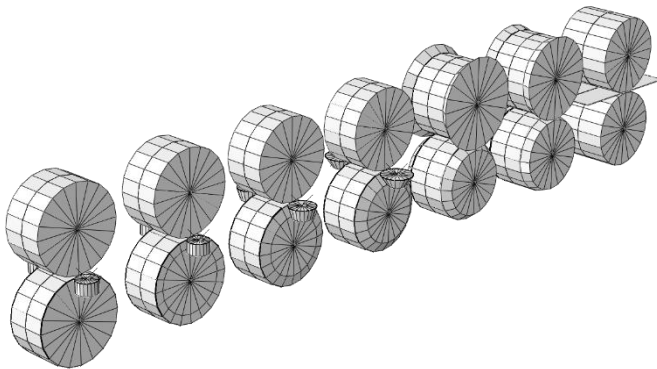
Figure 13 - Cold roll-forming FEA model in Abaqus®.
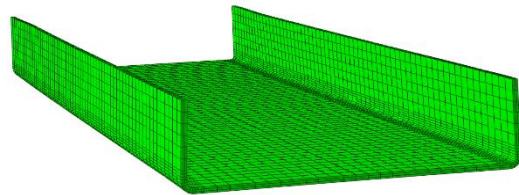
Figure 14 - Obtained U-channel in Abaqus®.
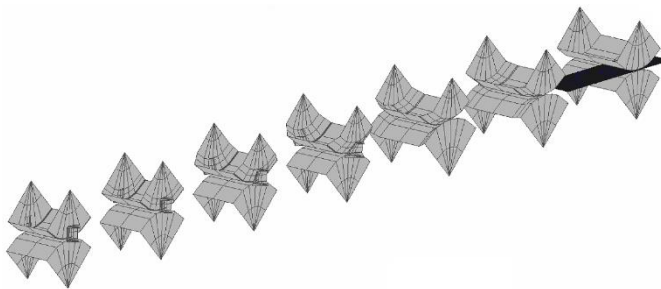
Figure 15 - Cold roll-forming FEA model in COPRA®.
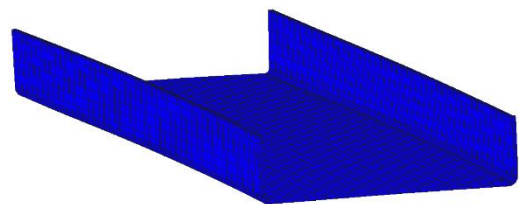
Figure 16 - Obtained U-channel in COPRA®.

2.2.   **Structural Fatigue Analysis**

Since the 19th century, failures due to material fatigue have been reported and investigations have been conducted in laboratories in order to understand this technical problem. At this time, failure due to fatigue damage seemed to occur without any apparent warning, hence, material fatigue was a mysterious

phenomenon since it could not be clearly observed. Nowadays, it is well understood that applying a single static load to a structure, whose magnitude is below the static strength of said structure, does not induce any structural damages. However, if the same load is applied repeatedly over time, fatigue damage can accumulate in the structure, leading to severe structural failures. Today, material fatigue is a serious subject which must be accounted for when designing structures, machinery, vehicles, aircrafts, etc. The past has already shown how catastrophic failures due to fatigue damage accumulation can be, from pressure vessel explosions to the collapse of large structures, such as bridges. Finally, accounting for fatigue in the design of structures is a multidisciplinary problem, as shown by Figure 17 (Schijve, 2008).
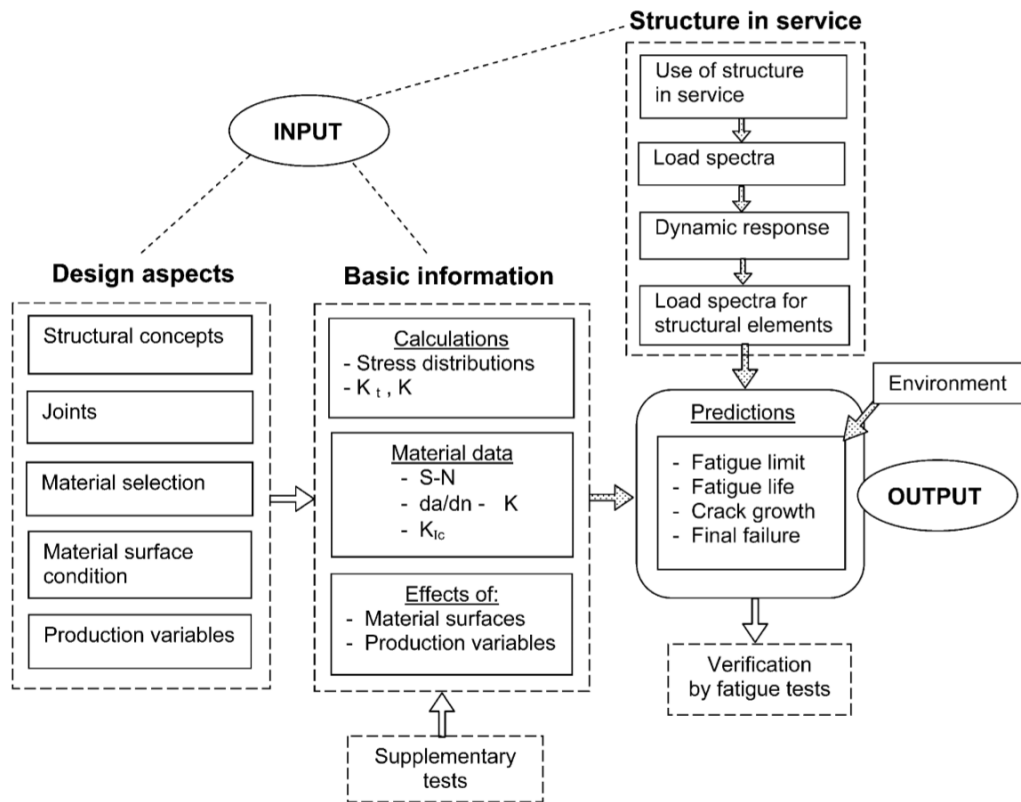
Figure 17 - Accounting for fatigue in the design of structures, a multidisciplinary problem (Schijve, 2008).

Regarding the mentioned repetitive loads, these are usually treated as load cycles. Load cycles can be categorized as:

- Constant amplitude load cycles, which induce constant amplitude stress cycles in the material, as shown in Figure 18;
- Variable amplitude load cycles, which induce variable amplitude stress cycles in the material.

For each stress cycle, the mean stress can be calculated as the arithmetic mean between the cycle's maximum and minimum stresses:

$$\sigma_m = \frac{\sigma_{max} + \sigma_{min}}{2}$$

                                                                             Equation 1

The stress range can be calculated, for each stress cycle, as:

$$\Delta\sigma = \sigma_{max} - \sigma_{min} \qquad\qquad \textbf{Equation 2}$$

For each stress cycle, the stress amplitude is given as:

$$\sigma_a = \frac{\Delta\sigma}{2} = \sigma_{max} - \sigma_m \qquad\qquad \textbf{Equation 3}$$

One can also define the stress ratio as:

$$R = \frac{\sigma_{min}}{\sigma_{max}} \qquad\qquad \textbf{Equation 4}$$

Therefore:

$$\Delta\sigma = \sigma_{max} \cdot (1 - R) \qquad\qquad \textbf{Equation 5}$$
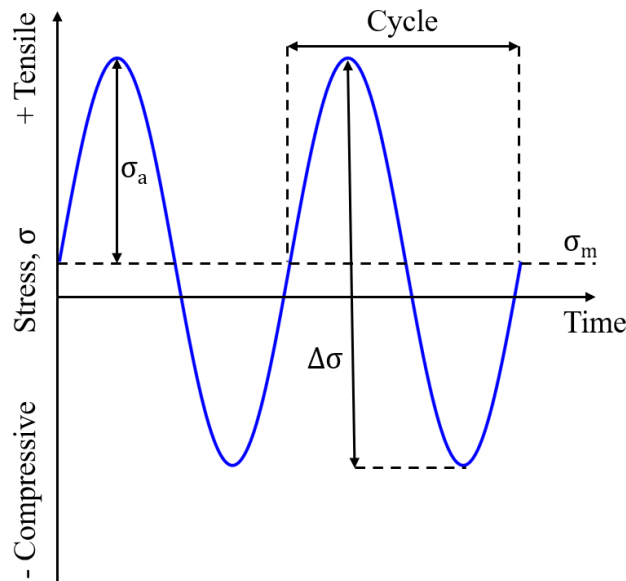
Figure 18 - Stress cycles induced by constant amplitude load cycles.

It is very common to present experimental fatigue results in the form of Wöhler's S-N curves. These S-N curves are also used in the fatigue design of structures. In a typical S-N curve (Figure 19), the lifetime of the structural element, in terms of number of load cycles endured, is placed on the horizontal axis, while the stress range at which the structural element is subjected is placed on the vertical axis (EN1993-1-9, 2014).

According to the EN1993-1-9 standard, the fatigue design curves for constant amplitude loading are given by the following expressions:

For $m = 3$ and $N \leq 5 \times 10^6$ $\quad \rightarrow \quad \Delta\sigma^m \cdot N = \Delta\sigma_C^m \cdot 2 \times 10^6$ **Equation 6**

$$\Delta\sigma_D = (2/5)^{1/3} \cdot \Delta\sigma_C = 0.737 \cdot \Delta\sigma_C$$ **Equation 7**

and for variable amplitude loading:

For $m = 3$ and $N \leq 5 \times 10^6$ $\quad \rightarrow \quad \Delta\sigma^m \cdot N = \Delta\sigma_C^m \cdot 2 \times 10^6$ **Equation 8**

For $m = 5$ and $5 \times 10^6 \leq N \leq 10^8$ $\quad \rightarrow \quad \Delta\sigma^m \cdot N = \Delta\sigma_D^m \cdot 5 \times 10^6$ **Equation 9**

$$\Delta\sigma_L = (5/100)^{1/5} \cdot \Delta\sigma_D = 0.549 \cdot \Delta\sigma_D$$ **Equation 10**

where m is the inverse slope of the S-N curve, N is the number of load cycles to failure, $\Delta\sigma_C$ is the detail category, $\Delta\sigma_D$ is the contant amplitude fatigue limit, and $\Delta\sigma_L$ is the cut-off limit.

When variable amplitude loading is present, a damage accumulation rule is required, such as the linear Miner's rule (Miner, 1945). Also, cycle counting techniques must be applied.

For variable amplitude stress ranges, the current author developed a recent computer software which is available to calculate the fatigue damage accumulation through the Miner's rule (Miner, 1945) by knowing the stress range history of the structure or structural element. In this software, a standardized (ASTM E1049-85, 2017) rainflow counting algorithm (Matsuishi & Endo, 1968) is employed to calculate the fatigue damage accumulation as a sum of the fatigue damage caused by each individual stress band present in the stress history (Souto, Correia, De Jesus, & Calçada, 2019).
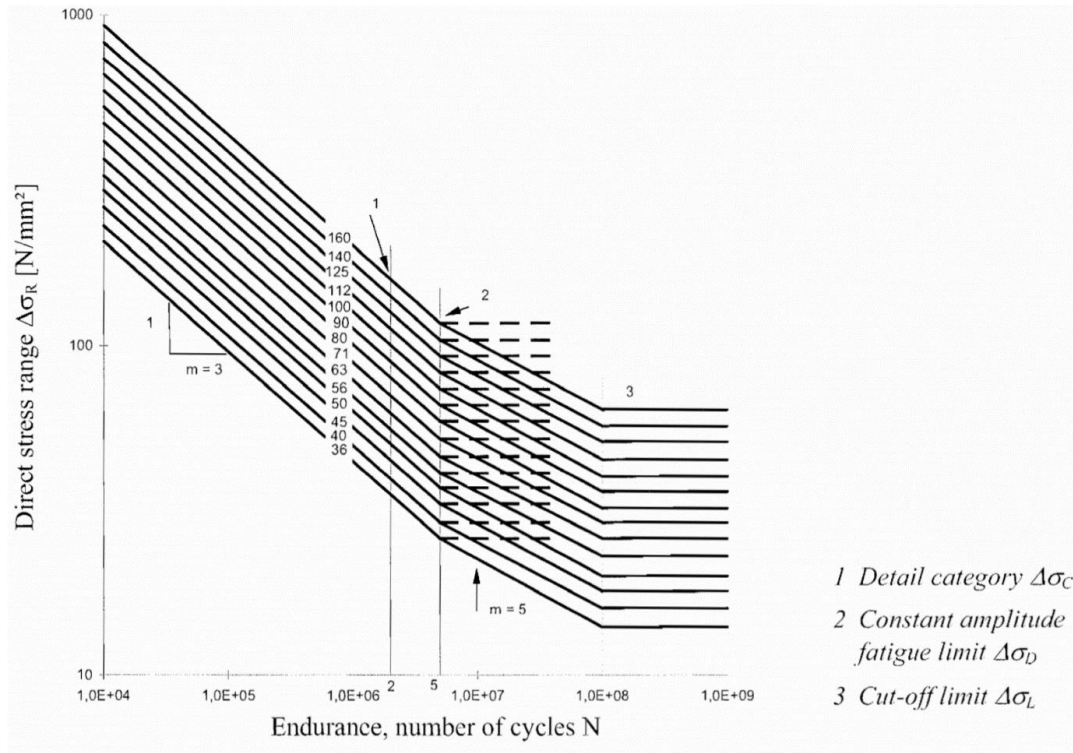
Figure 19 - Design S-N curves according to the EN1993-1-9 standard.

Using these S-N curves, for a known stress range at which the structure or structural element is subjected, a prediction of a lifetime, in terms of number of load cycles, can be made (EN1993-1-9, 2014).

When constructing a new S-N curve based on experimental data, the ASTM E739-91 standard can be used to obtain the mean S-N curve of the data, the standard deviation, the coeffcient of determination, and to establish confidance bands (ASTM E739-91, 2004).

An alternative to the mentioned S-N global approach (also known as Wöhler approach), one can use local approaches to account for fatigue damage. One of these approaches is the Coffin-Manson approach, where fatigue life prediction can be determined through empirically determined material constants by the use of Equation 11 (Coffin, 1954) (Manson, 1954).

$$\frac{\Delta\varepsilon}{2} = \frac{\sigma_f' - \sigma_m}{E} \cdot (2N)^b + \varepsilon_f' \cdot (2N)^c \qquad\qquad \textbf{Equation 11}$$

Where:

- $\Delta\varepsilon = \varepsilon_{max} - \varepsilon_{min}$ is the strain range within the load cycle, to be evaluated at critical spots of components;
- $\sigma_m = 0.5 \cdot (\sigma_{max} + \sigma_{min})$ is the mean stress of the load cycle at the same critical spot;
- N is the estimated lifetime in terms of load cycles;
- E is the Young's modulus of the material;
- σ_f', ε_f', b and c are empirically determined material constants, based on fatigue tests of smooth specimens.

The mentioned empirically determined material constants are available for the S355 structural steel, which is useful in the context of this dissertation (De Jesus, et al., 2012).

As stated in the previous section, the cold roll-forming fabrication process leaves in the final product internal residual stresses. As the cold roll-forming fabrication process consists in the forming/bending of a thin metal strip's section, in the bend zones of the strip, a concentration of residual stresses is expected. It is also expected that, for any particular bend in the section, one surface of the bend contains transversal tensile residual stresses, while the opposite surface contains transversal compressive residual stresses. As a result, fatigue life of the final product can be affected by its residual stresses and deformed microstructures. The residual stresses can also work against or in favor of endurance, depending how the section bend is being deflected (Martins, 2018).

Currently, the Eurocode 3 does not cover the fatigue behavior of thin cold roll-formed elements, which have internal residual stresses left over from their fabrication process, which may play a role on their fatigue/structural performance. The Eurocode 3 does cover the subject of thick hot-rolled elements; however, the residual stresses are not relevant in these types of structural elements due to recrystallization of the material (EN1993-1-9, 2014).

As seen by Figure 19, the highest available class ($\Delta\sigma_C$) in Eurocode 3 is 160 MPa, which is the recommended class for plain material, meaning that it is the recommended class for the mentioned cold-formed steel rails.

2.3.   Finite Element Analysis

Kuna (2012) stated that "The finite element method (FEM) is currently one of the most efficient and universal methods of numerical calculation for solving partial differential equations from engineering and scientific fields".

The FEM evolved from the works of Ritz and Galerkin in the beginning of the 20th century. Nowadays, this powerful numerical tool is used to solve partial differential equations (PDEs) in boundary value problems (BVPs), by discretizing a physical (geometric) domain with finite elements. The FEM can also be combined with the Finite Difference Method (FDM) to solve time dependent PDEs. The FDM is responsible for the temporal discretization on dynamic analyses. The dynamic analysis is either implicit or explicit depending on the chosen FDM formulation. If the BVP is not time dependent, the FEM can be used alone in static (or quasi-static) analyses.

In the FEM, the partial differential equations are transformed into systems of algebraic equations. Modern-day computers (even personal ones) can easily solve systems of algebraic equations with tens of thousands of equations and variables.

In the context of Solid Mechanics and Structural Mechanics, the FEM can be used to determine the displacements, strains, and stresses that occur in a structure or structural element when subjected to point, surface, and/or body loads. It can also be used to determine the modes of vibration in a complex structure (natural or forced) in the context of Mechanics of Vibrations. In the context of Fracture Mechanics, the FEM can also be used to calculate Stress Intensity Factors (SIFs).

The current author is also responsible for developing a new standalone Finite Element Analysis (FEA) software, capable of structural static and modal analysis (Souto, Omicron - A Free Finite Element Analysis Software, 2019).

The FEM also shines in other scientific fields, like Heat Transfer, Electromagnetism, and others.

Today, FEA programs are used in the development and design of new structures, machines, vehicles, aircrafts, etc. FEA is inexpensive and can give insight during the development process of a new product, even before the creation of prototypes and scale models, which can be expensive.

In the context of cold roll-forming, COPRA® arises as the global leader in specialized FEA software for roll-forming. With this software, the development of numerical models to simulate the roll-forming process is made easier and faster, optimizing workflow by the automatization of repetitive tasks in the construction of said models (data M Sheet Metal Solutions GmbH, 2020).

When simulating the cold roll-forming fabrication process with the FEM, a common simplification of the process is to fix the strip in space, impeding any rigid-body movements, and moving the rolls towards the strip. With this simplification, the hard contact interactions between the rolls and the strip are frictionless and the rolls do not actually roll. Because of this, the roll-forming simulation can be much faster and still present good results (Lindgren, 2013).

Not very common on the current literature is the numerical simulation of the cold roll-forming fabrication process combined with additional load cases for structural/fatigue loading simulations and analyses. Martins (2018) simulated the cold roll-forming process to obtain cold-formed elements with internal residual stresses and combined these results with additional load cases for structural/fatigue loading. This work was also conducted under the FASTCOLD project.

CHAPTER 3:   THE Z-RAIL

This short chapter introduces a specific Z-rail which will be used throughout the whole dissertation as a case study. The Z-rail's dimensions and its material will remain constant unless some changes are explicitly stated.

The Z-rail is fabricated through the cold roll-forming fabrication process. The rail starts off as a thin, coiled steel strip, which is then uncoiled onto a roll-forming machine. The machine then rolls the strip, forming and shaping its section. This process leaves internal residual stresses in the rail which can play an important role on the rail's fatigue performance and are the subject of investigation on this dissertation.

The Z-rail is used in rack structures, where pallet-carrying shuttles use these as tracks to move around while carrying various goods and products. Since these shuttles are usually automated, they can work non-stop, and because of this, the rails are subjected to cyclic loads caused by the passage of a shuttle. Because of these cyclic loads, that can be of high intensity, the rails experience fatigue phenomena; moreover, cracks due to material fatigue have already been observed in these types of rails, creating concerns about their fatigue performance.

Figure 20 shows a rack structure prepared for shuttles, where Z-rails are used as tracks. Figure 21 shows a shuttle being placed onto Z-rails. Figure 22 shows a loaded shuttle moving along Z-rails.

Figure 20 - Z-rails in a rack structure prepared for shuttles (courtesy of NEDCON).

Figure 21 - A shuttle being placed onto its tracks, Z-rails (courtesy of NEDCON).

Figure 22 - A loaded shuttle moving along Z-rails (courtesy of NEDCON).

3.1.   Dimensions and Section Geometry

The Z-rail gets its name due to the geometry of its section, which resembles the letter Z. Figure 23 shows the dimensions of the specific Z-rail used as a case study in this dissertation. The corner with a radius of 8 mm, sometimes called R8 corner or web-flange corner, is a critical location of the rail's section and it will be referenced several times. During experimental fatigue testing, the rail is loaded through its 61 mm flange, so the mentioned corner, due to the rail's section geometry, will have a great concentration of stresses, furthermore, cracks did develop in the web-flange corner during fatigue testing.
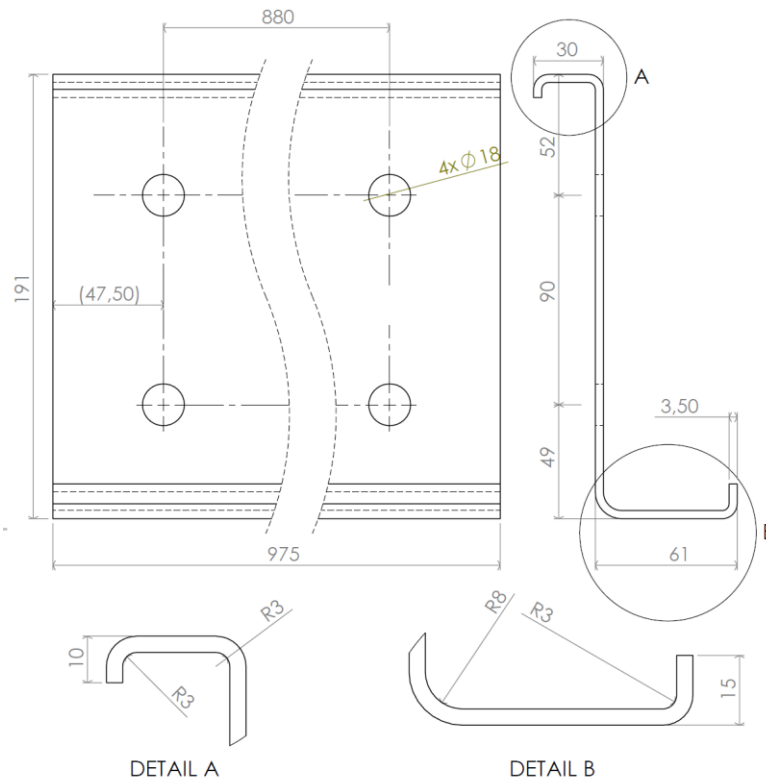
Figure 23 - Z-rail's technical drawing (dimensions in mm).

3.2.   Material

The Z-rail is composed by a mild steel, denoted S355MC. To obtain its elastoplastic properties for numerical simulations, experimental material testing was conducted both at UPorto (FEUP) and at RWTH Aachen University, both partners in the FASTCOLD project, using dog-bone type specimens.

Table 2 shows the elastic properties of the S355MC material as reported from Aachen, while the elastoplastic curve in terms of nominal stresses and strains obtained through experimental testing is shown in Figure 24. To correctly use the information presented in Figure 24, first it is necessary to convert the data from nominal strains, e, and nominal stresses, σ_0, to true strains, ε, and true stresses, σ, by the use of Equation 12 and Equation 13. The result of this conversion is shown in Figure 25.

$$\varepsilon = \ln(1 + e)$$ **Equation 12**

$$\sigma = \sigma_0 \cdot (1 + e)$$ **Equation 13**

Table 2 - S355MC elastic properties.

Young's Modulus, E [MPa]	Poisson's Ratio, ν
200,000	0.3
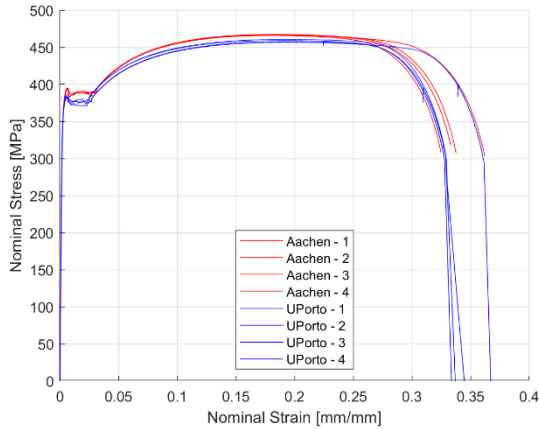
Figure 24 - S355MC experimental tensile curves in terms of nominal stresses and strains.
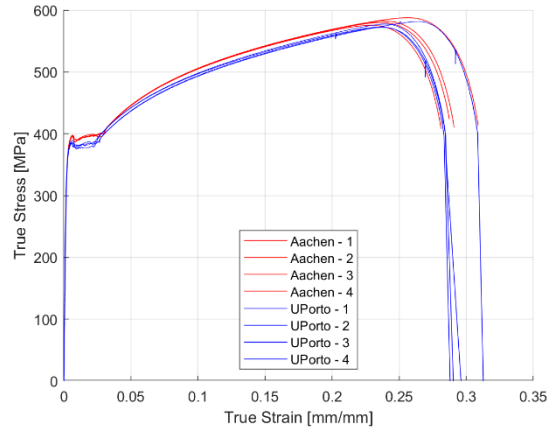
Figure 25 - S355MC experimental tensile curves in terms of true stresses and strains.

To obtain points for the material's hardening curve, the Swift law (Hosford, 2005) was employed up to the maximum load and then used to extrapolate additional points:

$$\sigma = K \cdot (\varepsilon_0 + \varepsilon_p)^n \qquad\qquad \textbf{Equation 14}$$

where σ is the true stress, ε_p is the true plastic strain, and K, n, and ε_0 are material constants determined from a uniaxial tensile test.

The Swift law (Equation 14) was used as a curve fitting model in order to extract points from the experimental data. These points are later used as an input for numerical models. Table 3 shows the Swift law's parameters used. Figure 26 shows the points that where selected to define the hardening curve of the material in numerical models. It should be noted that 197 points were used, where the true plastic strain ranged from 0 to 1.

It should also be noted that, as show in Figure 26, the first point of the extracted points from the Swift law was modified in the hopes of capturing the yield plateau of the experimental yield curves.

Table 3 - Swift law's parameters used.

K [MPa]	ε_0	n
750	0.005	0.175
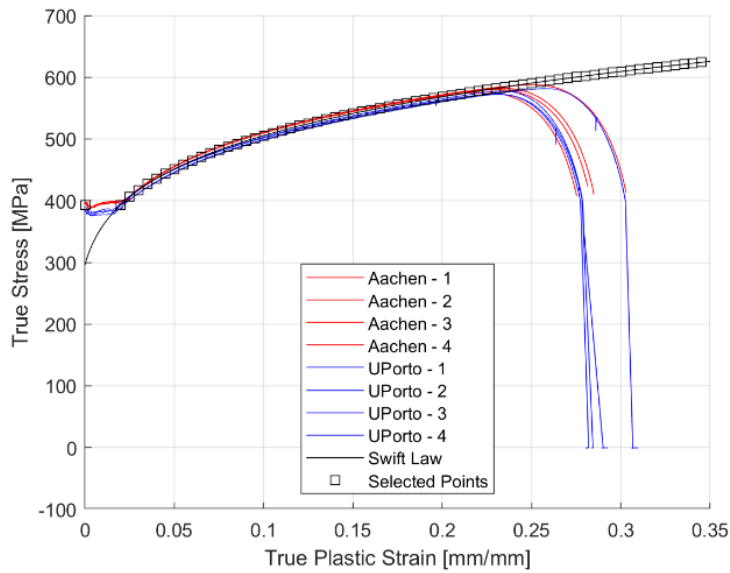
Figure 26 - Selected points for the definition of the S355MC hardening curve in numerical models.

To verify that the selected points model correctly the S355MC material, a uniaxial test was simulated in both Marc® and Abaqus®. These classic finite element models are composed of a unitary 3D cube with isostatic boundary conditions subjected to a uniaxial load. Both models are using the elastic material properties presented in Table 2, as well as the hardening curve defined by the selected points shown in Figure 26.

Figure 27 shows the results for the mentioned uniaxial test simulations. As shown by the figure, a very good match is visible between the numerical models in Marc® and Abaqus® and the experimental results, meaning that the material's elastoplastic behavior is being correctly modeled.
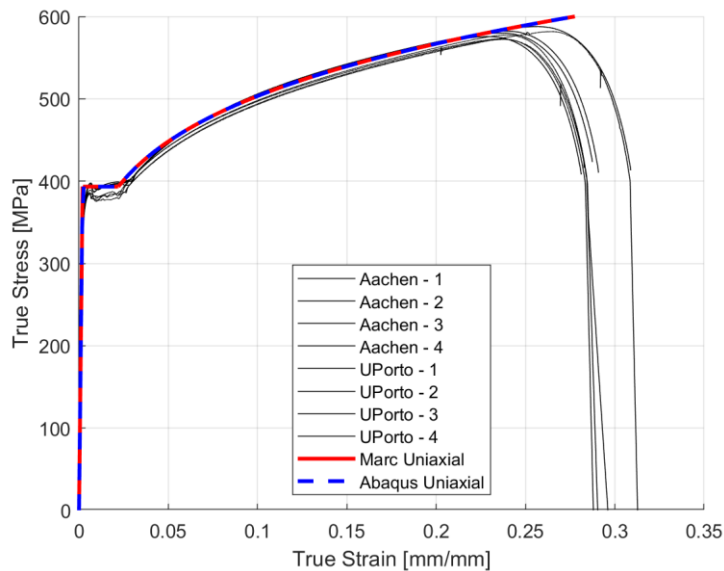
Figure 27 - Results for the uniaxial test simulations.

CHAPTER 4:   FATIGUE TESTING SETUP FOR Z-RAILS

In this chapter, the development of a new fatigue testing setup for Z-rails is presented. This new testing setup was developed and improved successively throughout thoughtful trial and error in order to obtain the best possible experimental results, i.e., the setup is able to generate representative fatigue cracks at the rail's web-flange corner due to the shuttle's cyclic loads (example in Figure 31). Numerical simulations were also conducted to replicate the experimental setup. These simulations helped in identifying problems with the setup and allowed it to be improved.

Since the real-life cyclic loads due to the passage of a shuttle are impractical to replicate at the laboratory, these loads were reproduced by placing a loading device at the mid-span of the rail, on the flange, exerting an up and down motion. The loading device was also developed in such a way that it allows for different load actuator geometries (the part that contacts the rail and transfers the load). The rails are clamped at both ends and, for optimal results, a mid-span support was also included to represent a rail-upright connection. Fatigue testing is done through load control, while strain information is gathered through a strain gauge placed near the rail's web-flange corner. Loading cycles were applied with a loading ratio of $R = 0.1$, i.e., the minimum load of the load cycle is equal to 10% of the maximum load.

In this setup, depicted in Figure 28 and shown in Figure 30, two rail specimens are tested at the same time, which is made possible due to the pin-joint connection between the loading device and the load cell, as depicted in Figure 29, allowing for an even load distribution between the two rails, as well as a constant load amplitude during testing.
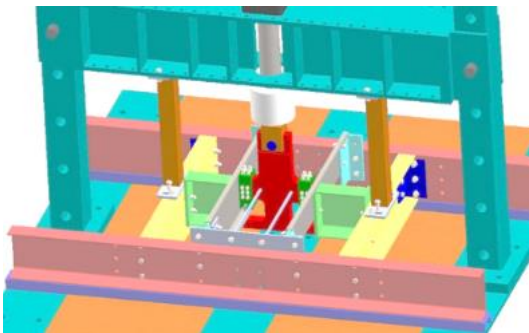
Figure 28 - Experimental fatigue testing setup for Z-rails (CAD).
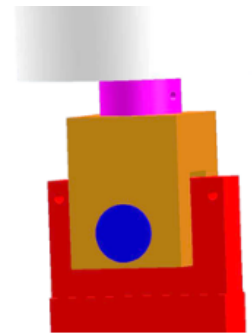
Figure 29 - Pin-joint connection between the loading device and the load cell.

Figure 30 - Experimental fatigue testing setup for Z-rails (laboratory).

Figure 31 - Representative fatigue cracks (example).

In order to better understand the importance of the residual stresses left over on the rail from its fabrication process, the experimental setup for fatigue testing allows for two loading scenarios: a downward loading

scenario, where the rail is loaded through the top of its flange, and an upward loading scenario, where the rail is loaded through the bottom of its flange. Figure 32 and Figure 33 show the final downward loading setup, while Figure 34 and Figure 35 show the final upward loading setup.
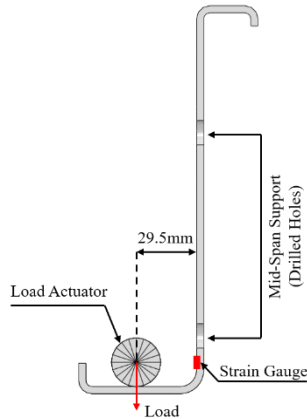
Figure 32 - Final downward loading setup.

Figure 33 - Experimental setup used on a downward loading scenario.
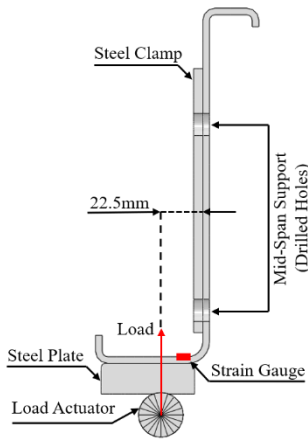
Figure 34 - Final upward loading setup.

Figure 35 - Experimental setup used on an upward loading scenario.

After fatigue testing, it is necessary to process the experimental data obtained through each specimen's strain gauges to determine the lifetime for each specimen in terms of number of load cycles. The strain gauges were placed in a free region allowing crack monitorization. As an example, Figure 36 shows the strain gauge's data obtained for specimen 7. For plotting purposes, strains were converted into stresses through the following constitutive law:

$$\sigma = E \cdot \varepsilon$$

Equation 15

Then, a stress range was calculated for each load cycle, as shown in Figure 37. This step is helpful since the collected strain gauge's data treats the variable "Cycles" as a real variable when it should be an integer variable. For each load cycle, the stress range is given as the difference between its maximum and minimum registered stresses.

The lifetime of a specimen is usually determined by a 10% load decrease on the stress range plot, as shown in Figure 37. As an example, specimen 7 had a lifetime of around 325,000 cycles. For some specimens, the

obtained data from the strain gauge was not so well-behaved. In these cases, common sense was used to determine the lifetime of the specimen, combined with visual inspections and written records on crack development from the laboratory staff.
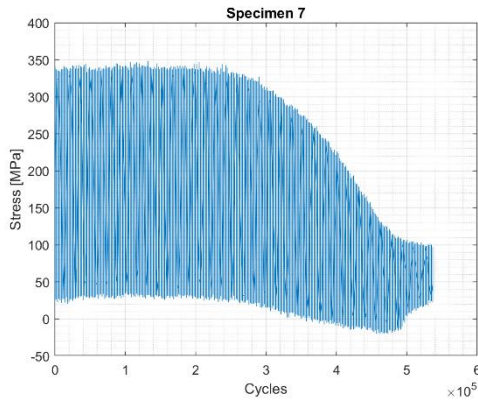
Figure 36 - Stress vs. load cycles (specimen 7 example).
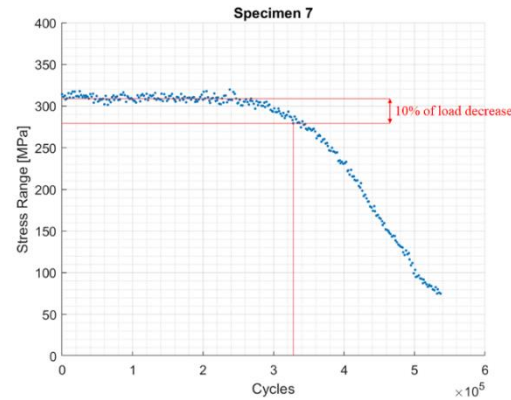
Figure 37 - Stress range per load cycle (specimen 7 example).

Finally, Appendix A shows the obtained experimental data from each specimen's strain gauges, and Appendix B shows photographs of the cracks that developed in the rail specimens.

In the following sections, the history of the testing setups is presented, allowing readers to have a better understanding of the whole fatigue testing setup development process.

4.1. Downward Loading Setup Development

4.1.1. Setup #1

The first experimental setup for fatigue testing considering a downward loading scenario consisted in the following characteristics:

- Steel load actuators with a 5×10 mm^2 contact area, as shown in Figure 38, placed at the mid-span of the rail, on top of its flange;
- Rails clamped at both ends (without a mid-span support);
- Cycling was done through displacement control;
- Rigid connection between the loading device and the load cell;
- Strain gauge placed at the web, near the web-flange corner, as shown in Figure 39;
- Specimens 1 and 2 were tested.

Figure 38 - Load actuators for downward loading scenario setup #1.

Figure 39 - Strain gauge's placement (downward setup #3; in setup #1 the shown drilled hole is not present).

21

With this setup, in both used specimens, material failure occurred in the opposite side of the load actuator's contact zone, as shown in Figure 40 to Figure 43, while it was expected to occur in the local web-flange corner.

| **Figure 40 - Specimen 1 (top view).** | **Figure 41 - Specimen 1 (bottom view).** | **Figure 42 - Specimen 2 (top view).** | **Figure 43 - Specimen 2 (bottom view).** |

Figure 44 shows the registered load cell's load during the experiment. Notice that the plot shows half of the load's magnitude, since two specimens are being tested at the same time. A visible trend in the decrease of the load's magnitude is noticeable. This is expected since, in this setup, cycling was done through displacement control, so as the number of cycles increases, the required load to obtain the constant displacement decreases, due to material fatigue.
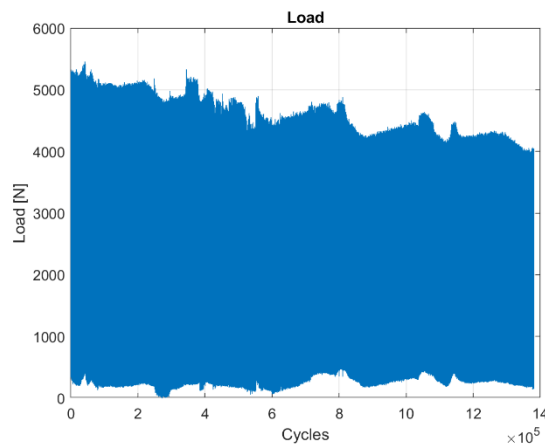
Figure 44 - Registered load for specimens 1 and 2.

Figure 45 shows the strain gauge's data obtained for the specimens during testing. As stated before, strains were converted into stresses using the constitutive law shown in Equation 15. The figure shows that the cracks that developed on the other side of the load actuator's contact zone did not affect the strain gauge's readings in a noticeable manner.
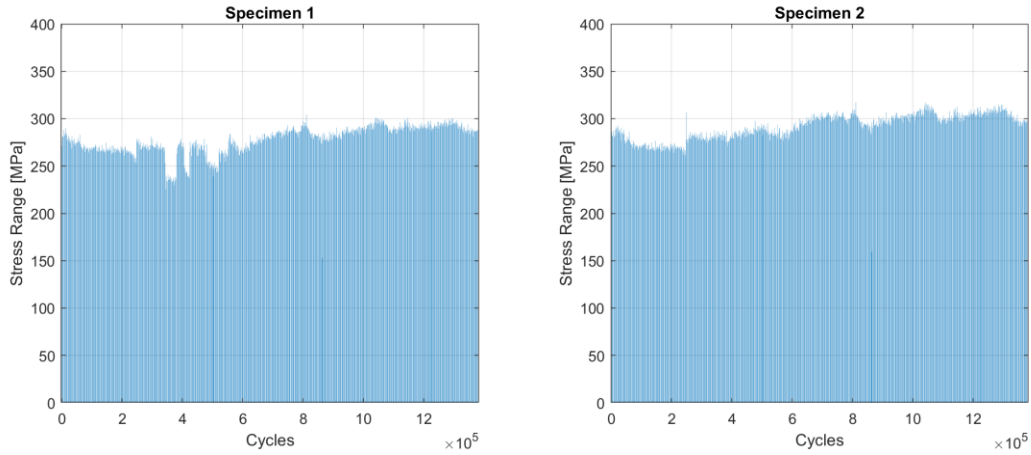
Figure 45 - Strain gauge's data obtained for specimens 1 and 2.

A numerical simulation replicating the current experimental setup was conducted in Abaqus®. The simple 3D finite element model consists on the Z-rail clamped at both ends, using the elastoplastic material model presented in Chapter 3. The numerical model also includes hard contact, with a friction coefficient of $\mu = 0.2$, between the steel actuator and the rail's flange, as well as non-linear geometry effects. To replicate the experimental setup, the actuator was advanced until a reaction force of 5000 N was achieved. The actuator is also free to rotate along the rail's length axis, and it is considered a non-deformable rigid part. The rail was discretized with the C3D8 element, a continuum hexahedral element with 8 nodes and 8 integration points (full integration).

Figure 46 presents the results of the mentioned simulation. The figure shows the absolute maximum principal stresses (also known as major principal stresses). As shown by the figure, a significant concentration of stresses can be seen on the bottom of the flange, opposite side of the contact zone, where cracks developed during fatigue testing. This concentration of stresses is not ideal and may be the reason for why results using this setup were not satisfactory. Moreover, this stress concentration tends to be aggravated as the test continues due to fretting and local indentations on the rail's flange due to the hard contact between it and the steel actuator.
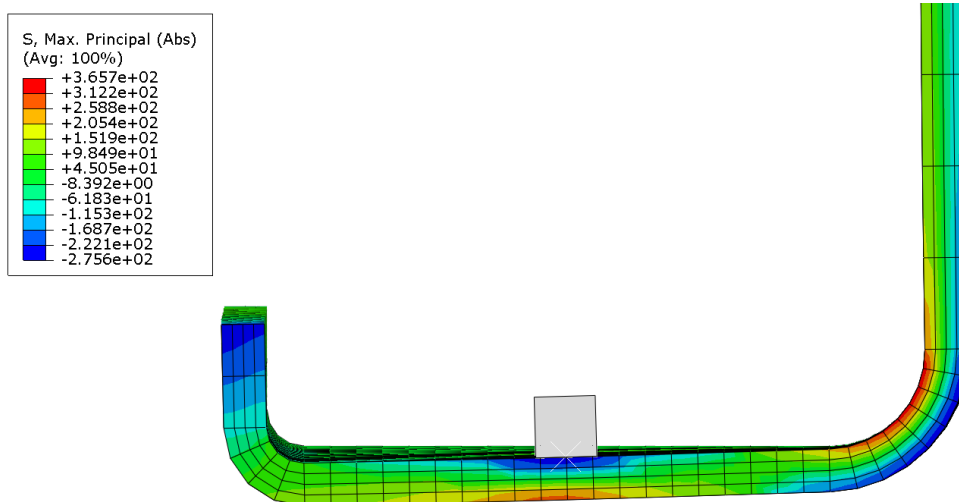
Figure 46 - Numerical simulation of the downward loading scenario setup #1 ($P = 5000$ N).

23

4.1.2. Setup #2

The second experimental setup for fatigue testing considering a downward loading scenario was prepared based on the following characteristics:

- The same load actuators as in the previous setup;
- Rails clamped at both ends, but now with an added mid-span support to improve the local stiffness of the rail and to simulate the worst-case scenario (a shuttle wheel passing through the rail-upright connection);
- Cycling was done through displacement control (same as last setup);
- Rigid connection between the loading device and the load cell (same as last setup);
- Strain gauge placed in the same location as the previous setup;
- Specimens 3 and 4 were tested.

With this setup, results were similar to previous ones. In both used specimens, material failure occurred in the opposite side of the load actuator's contact zone, as shown in Figure 48, while expected to occur in the local web-flange corner. Figure 47 and Figure 49 show some local indentations and fretting due to the hard contact.

Figure 47 - Specimen 3 (top view).   **Figure 48 - Specimen 3 (bottom view).**   **Figure 49 - Specimen 4 (top view).**

Figure 50 shows the registered load cell's load during the experiment. Again, a visible trend in the decrease of the load's magnitude is noticeable. This is expected since, in this setup, cycling was done through displacement control, so as the number of cycles increases, the required load to obtain the constant displacement decreases, due to material fatigue.

Figure 51 shows the strain gauge's data obtained for the specimens during testing. As stated before, strains were converted into stresses using the constitutive law shown in Equation 15. The figure shows that the cracks that developed on the other side of the load actuator's contact zone did not significantly affect the strain gauge's readings. One can see a decreasing trend that is likely due to the load reduction.
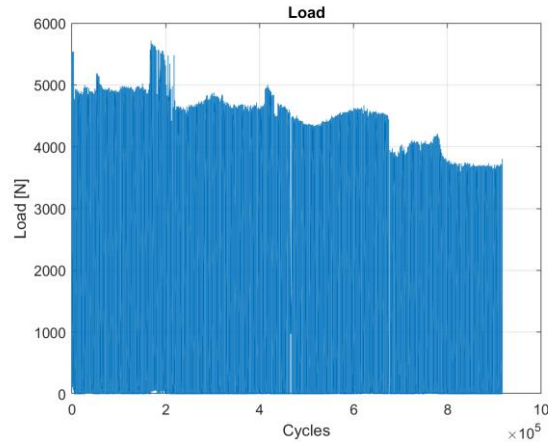
Figure 50 - Registered load for specimens 3 and 4.

Figure 51 - Strain gauge's data obtained for specimens 3 and 4.

Like in the previous setup, a numerical simulation replicating the current experimental setup was conducted in Abaqus®. The numerical model was reused from the previous setup, with the addition of the new mid-span support.

Figure 52 presents the results of the mentioned simulation. The figure shows the absolute maximum principal stresses (also known as major principal stresses). Comparing Figure 46 and Figure 52, the concentration of stresses at the bottom of the flange is reduced due to higher stress values at the rail's web-flange corner. However, experimental results using this setup were still not satisfactory, since an undesired cracking pattern was obtained, probably due to local indentations and fretting observed in the experiments.

Figure 52 - Numerical simulation of the downward loading scenario setup #2 ($P = 5000$ N).

4.1.3. Setup #3

The third experimental setup for fatigue testing considering a downward loading scenario consisted in the following conditions:

- New load actuators with a larger $16{\times}30$ mm^2 contact area, as shown in Figure 53;
- Rails clamped at both ends with an added mid-span support (same as last setup);
- Cycling was done through displacement control (same as last setup);
- Rigid connection between the loading device and the load cell (same as last setup);
- Strain gauge placed in the same location as the previous setup (Figure 53);
- Specimens 5 and 6 were tested.

With this setup, results were similar to previous ones. In both used specimens, material failure occurred in the opposite side of the load actuator's contact zone, as shown in Figure 54 to Figure 56, while it was expected to occur in the local web-flange corner. However, with this setup, cracks were perpendicular to the rail's length axis, with some crack bifurcation.

Figure 57 shows the registered load cell's load during the experiment. Again, a visible trend in the decrease of the load's magnitude is noticeable. This is expected since, in this setup, cycling was done through displacement control, so as the number of cycles increases, the required load to obtain the constant displacement decreases, due to material fatigue.

Figure 58 shows the strain gauge's data obtained for the specimens during testing. As stated before, strains were converted into stresses using the constitutive law shown in Equation 15. The figure shows that the cracks that developed on the other side of the load actuator's contact zone did not affect the strain gauge's readings in a decisive way to identify fatigue cracking.

Figure 53 - Load actuators for downward loading scenario setup #3 (strain gauge marked in red).

Figure 54 - Specimen 5 (top view).

Figure 55 - Specimen 6 (top view).

Figure 56 - Specimen 5 and 6 (bottom view).
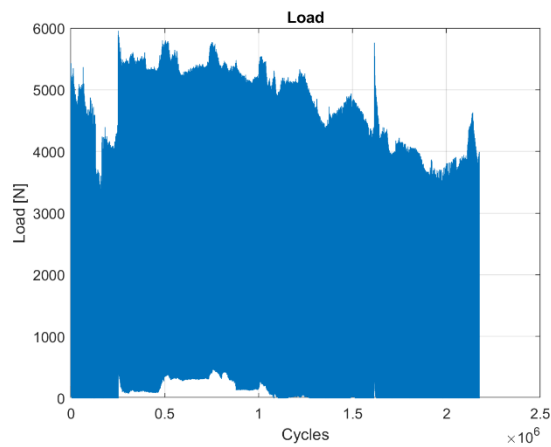
Figure 57 - Registered load for specimens 5 and 6.

Figure 58 - Strain gauge's data obtained for specimens 5 and 6.

Like in the previous setup, a numerical simulation replicating the current experimental setup was conducted in Abaqus®. The numerical model was reused from the previous setup, with the updated load actuator's geometry.

Figure 59 presents the results of the mentioned simulation. The figure shows the absolute maximum principal stresses (also known as major principal stresses). Comparing Figure 59 to Figure 46 and Figure 52, it is possible to visualize that the concentration of stresses at the flange has disappeared. However, experimental results using this setup were still not satisfactory due to peak contact stresses from imperfect contact between the loading facet and flange.
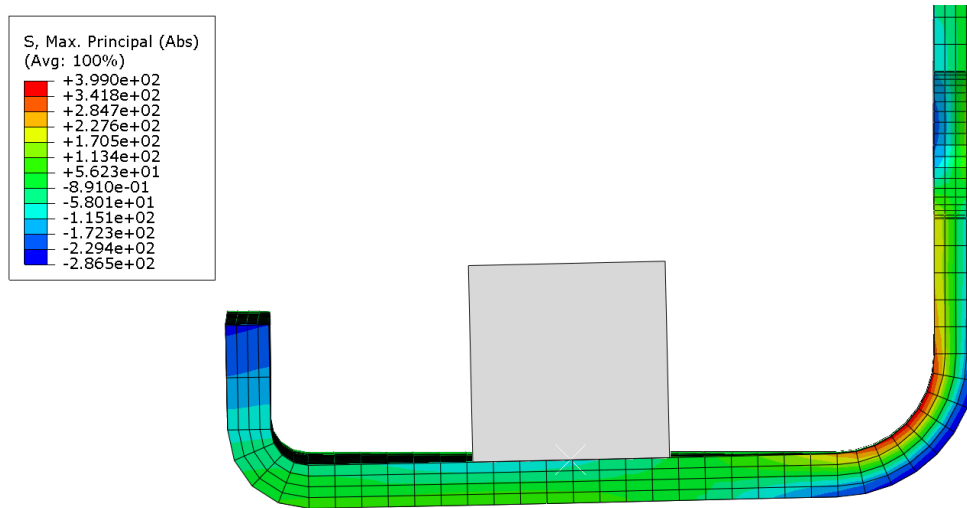
Figure 59 - Numerical simulation of the downward loading scenario setup #3 ($P = 5000$ N).

4.1.4. Setup #4

The fourth and final experimental setup for fatigue testing considering a downward loading scenario consisted in the following characteristics:

- New steel cylindrical actuators with hemispherical ends, as shown in Figure 60 and Figure 61 (also shown previously in Figure 32 and Figure 33);
- Rails clamped at both ends with an added mid-span support (same as setup #2 and #3);
- Cycling is now done through load control instead of displacement control;
- New pin-joint connection between the loading device and the load cell allowing for an even load distribution between the two rails and a constant load amplitude during testing (Figure 29);
- Strain gauge placed in the same location as the previous setup;
- Specimens 7 to 10 were tested at 5 kN of maximum load;
- Specimens 49 and 50 were tested at 5.5 kN of maximum load;
- Specimens 19, 20, 23 and 24 were tested 6.25 kN of maximum load;
- Specimens 11 to 14 were tested at 7.5 kN of maximum load;
- Specimens 17, 18, 21 and 22 were tested at 9 kN of maximum load;
- Specimens 15 and 16 were tested for monotonic loading (useful for calibrating numerical models).

Figure 60 - Load actuators for downward loading scenario setup #4.
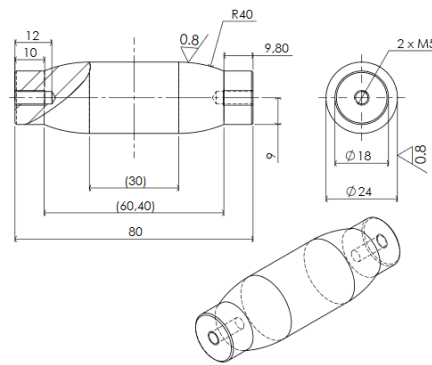
Figure 61 - Load actuators for downward loading scenario setup #4 (CAD).

With this setup, results were now optimal, i.e., the setup is now able to generate representative fatigue cracks at the rail's web-flange corner due to the shuttle's cyclic loads, show in Figure 62 (specimen 12 example).

Figure 62 - Representative fatigue cracks (specimen 12 example).

Figure 63 shows the registered load cell's load during experiments (example for specimens 11 and 12). The load amplitude is constant during testing, which is expected since, in this setup, fatigue testing is done through load control.

Figure 64 shows the strain gauge's data obtained for the specimens during testing (example for specimens 11 and 12). As stated before, strains were converted into stresses using the constitutive law shown in

Equation 15. Also as stated before, the lifetime of a specimen is usually determined by a 10% load decrease on the stress range plot. As an example, specimen 11 and 12 had a lifetime of around 160,000 and 120,000 load cycles, respectively. Again, for some specimens, the obtained data from the strain gauge was not so well-behaved. In these cases, common sense was used to determine the lifetime of the specimen, combined with visual inspections and written records on crack development from the laboratory staff.

As stated above, the strain gauge's data for all specimens is shown in Appendix A. Photographs of the cracked specimens can be seen in Appendix B.

Figure 63 - Registered load for specimens 11 and 12 (example).
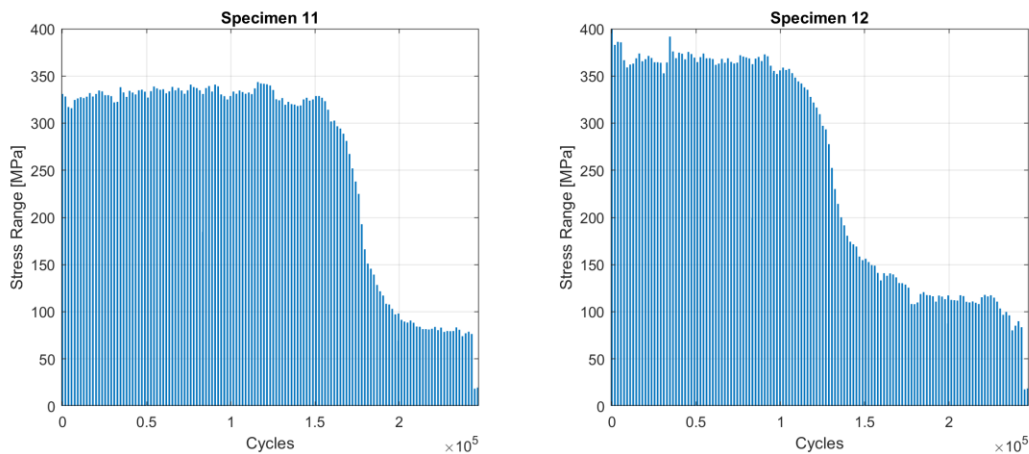
Figure 64 - Strain gauge's data obtained for specimens 11 and 12 (example).

Like in the previous setup, a numerical simulation replicating the current experimental setup was conducted in Abaqus®. The numerical model was reused from the previous setup, with the updated load actuator's geometry.

Figure 65 presents the results of the mentioned simulation. The figure shows the absolute maximum principal stresses (also known as major principal stresses). Comparing Figure 65 to Figure 59, an ever so slight increase on concentration of stresses in the rail's flange is visible. However, partially due to the smooth nature of the load actuator's geometry, which reduces fretting, experimental results are now very satisfactory.

30
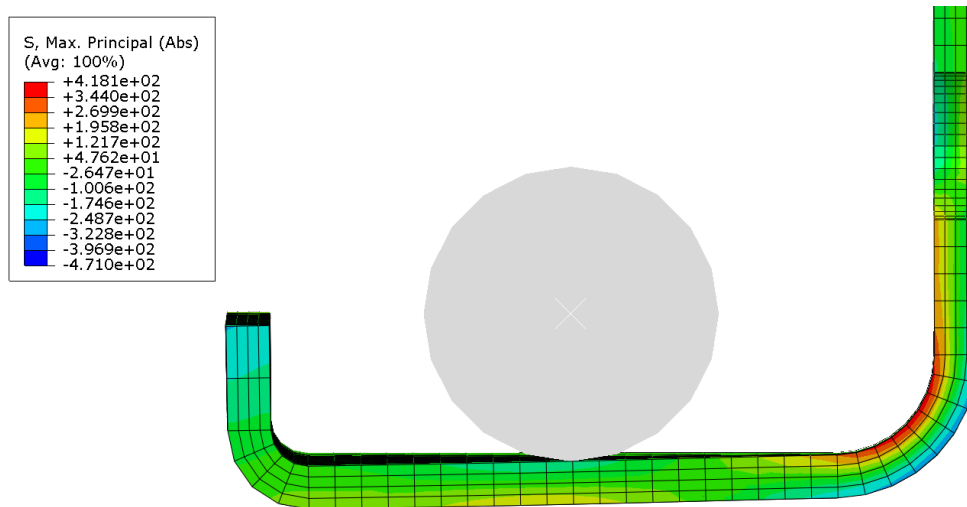
Figure 65 - Numerical simulation of the downward loading scenario setup #4 ($P = 5000$ N).

4.2. Upward Loading Setup Development

4.2.1. Setup #1

The first experimental setup for fatigue testing considering an upward loading scenario consisted in the following:

- The same load actuators from the final experimental setup considering a downward loading scenario (Figure 60), but now placed underneath the flange, as shown in Figure 66;
- Rails clamped at both ends with an added mid-span support (same as last setup);
- Cycling done through load control (same as last setup);
- Pin-joint connection between the loading device and the load cell (same as last setup);
- Strain gauge now placed underneath the rail's flange, between the load contact zone and the web-flange corner (Figure 67);
- Specimens 25 and 26 were tested at 9 kN of maximum load;
- Specimens 27 and 28 were tested for monotonic loading (useful for calibrating numerical models).

Figure 66 - Load actuators for upward loading scenario setup #1.

Figure 67 - Strain gauge's placement for upward loading scenario setup #1.

With this setup results were not satisfactory. In specimen 25, a single crack developed on the opposite side of the load actuator's contact zone (Figure 68), while in specimen 26 two cracks appeared, the first on the opposite side of the load actuator's contact zone and then the second in the web-flange corner (Figure 69).

Figure 68 - Specimen 25 (top view).

Figure 69 - Specimen 26 (top view).

Figure 70 shows the strain gauge's data obtained for the specimens during testing. As stated before, strains were converted into stresses using the constitutive law shown in Equation 15. The figure shows that the developed cracks affected the strain gauge's readings with a sudden increase in strain values.
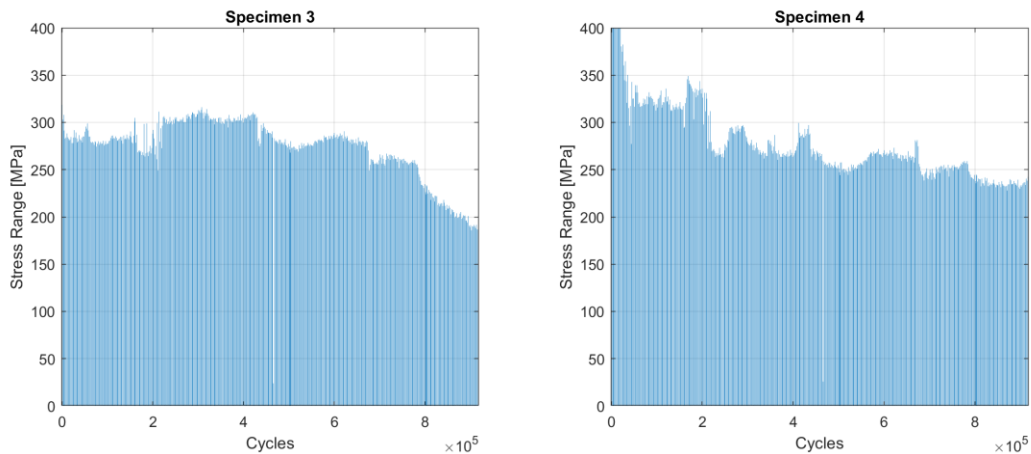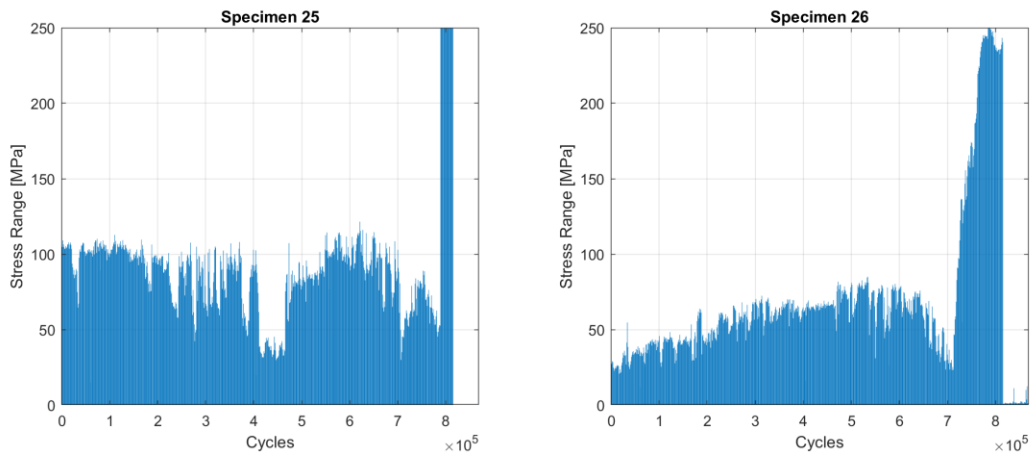

Figure 70 - Strain gauge 's data obtained for specimens 25 and 26.

Again, a numerical simulation replicating the current experimental setup was conducted in Abaqus®. The numerical model was reused from the previous setup, with the updated load actuator's placement, as well as an updated load of 9000 N.

Figure 71 presents the results of the mentioned simulation. The figure shows the absolute maximum principal stresses (also known as major principal stresses). Comparing Figure 71 to Figure 65, an interesting phenomenon can be seen. When the load actuator is placed on the bottom of the rail's flange, a significant

concentration of stresses now appears on the opposite side of the flange. This concentration of stresses on the top of the flange may explain why experimental results were not satisfactory (cracks appeared on the top of the flange).
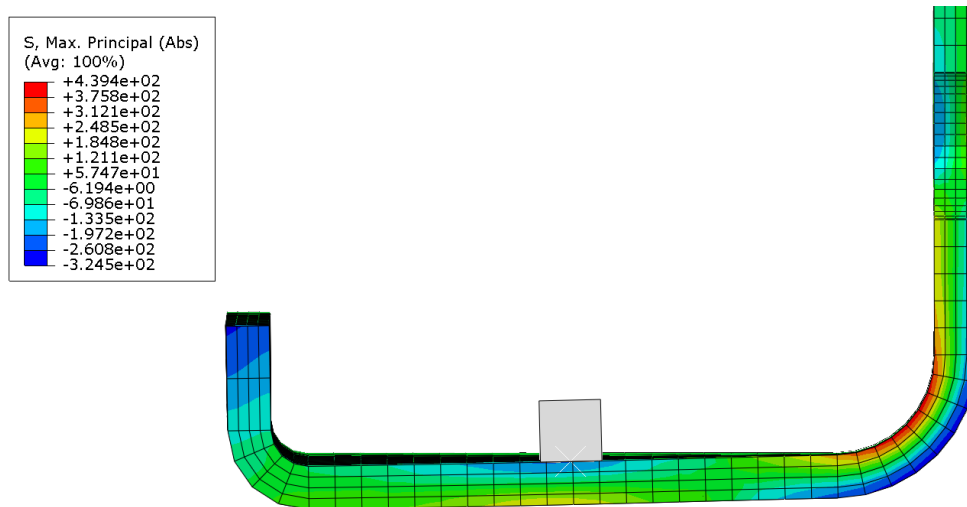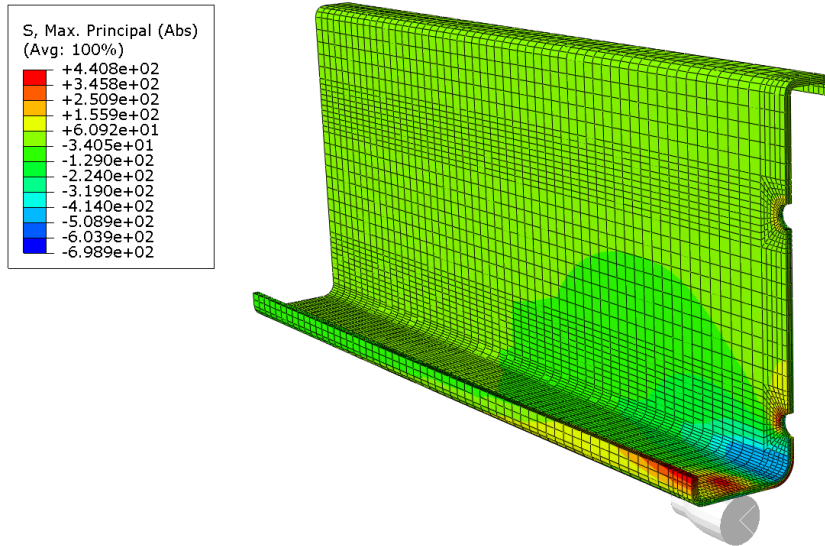

Figure 71 - Numerical simulation of the upward loading scenario setup #1 ($P = 9000$ N).

4.2.2. Setup #2

The second experimental setup for fatigue testing considering an upward loading scenario consisted in the following:

- The same load actuators from the last setup, but now with an added aluminum plate (with a 24×40 mm^2 contact area) between the load actuator and the rail's flange (Figure 72). The idea is to reduce the concentration of stresses in the rail's flange by increasing the contact area;
- Rails clamped at both ends with an added mid-span support (same as last setup);
- Cycling done through load control (same as last setup);
- Pin-joint connection between the loading device and the load cell (same as last setup);
- Strain gauge re-placed in the same position as the downward setups;
- Specimens 29 and 30 were tested at 9 kN of maximum load.

Figure 72 - Load actuators for upward loading scenario setup #2.

With this setup, material failure occurred opposite to the load actuator's plate contact zone, along the edge closest to the web-flange corner (Figure 73 to Figure 75).

Figure 73 - Specimen 29 (bottom view).

Figure 74 - Specimen 30 (top view).

Figure 75 - Specimen 30 (bottom view).

Figure 76 shows the strain gauge's data obtained for the specimens during testing. As stated before, strains were converted into stresses using the constitutive law shown in Equation 15. The figure shows that the cracks that developed on the other side of the load actuator's plate contact zone did not affect the strain gauge's readings significantly, therefore, the strain gauges cannot be used as a cracking detection method for this setup.
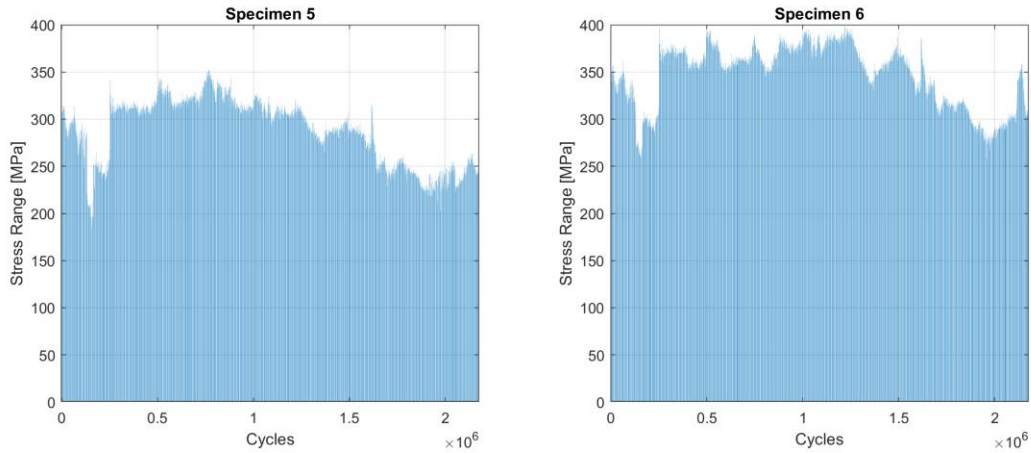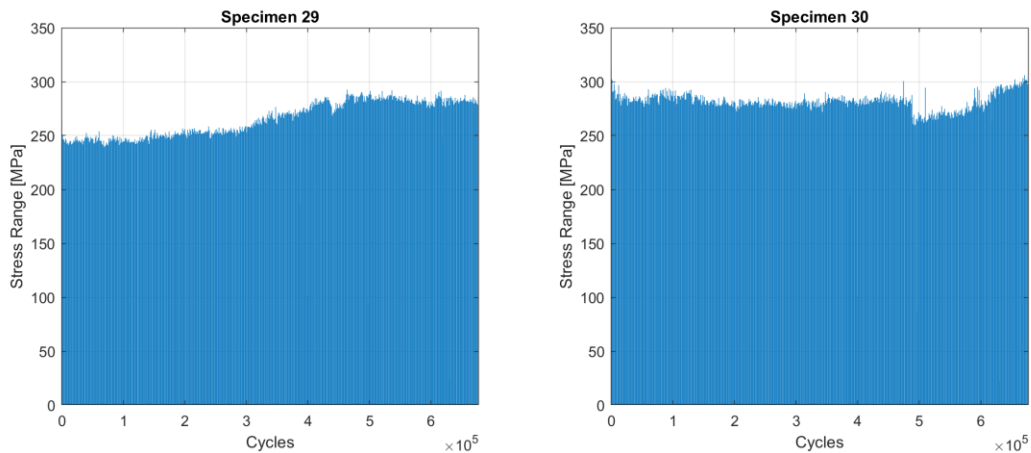

Figure 76 - Strain gauge's data obtained for specimens 29 and 30.

Again, a numerical simulation replicating the current experimental setup was conducted in Abaqus®. The numerical model was reused from the previous setup, with the updated load actuator's plate.

Figure 77 presents the results of the mentioned simulation. The figure shows the absolute maximum principal stresses (also known as major principal stresses). Comparing Figure 77 to Figure 71, the

concentration of stresses on the rail's flange is significantly reduced. However, experimental results using this setup were still not optimal.
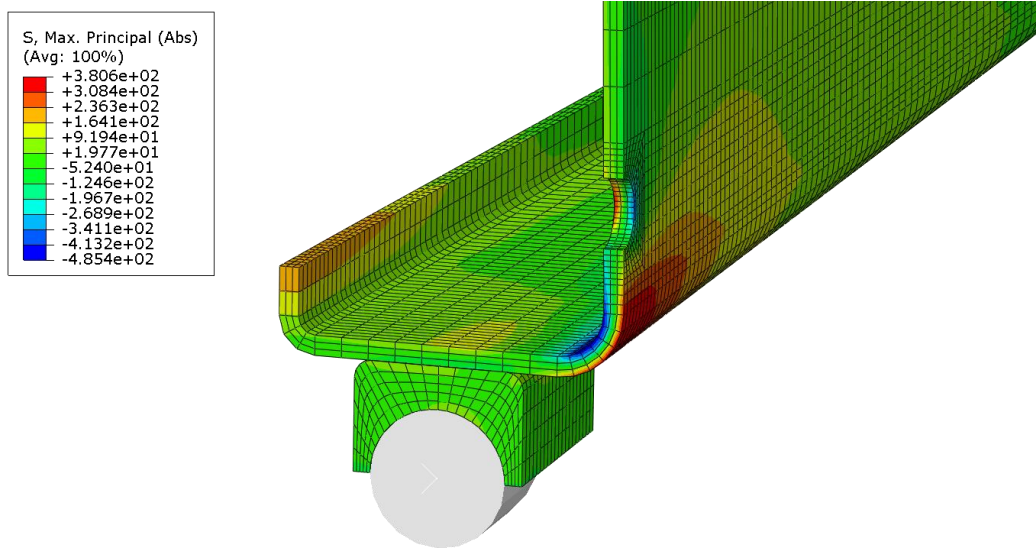
Figure 77 - Numerical simulation of the upward loading scenario setup #2 ($P = 9000$ N).

4.2.3. Setup #3

The third and final setup for fatigue testing considering an upward loading scenario consisted in the following:

- The same load actuators from the last setup, but with an updated steel plate (with a 26×50 mm² contact area) between the load actuator and the rail's flange (Figure 78, Figure 34 and Figure 35). Since this plate is now larger, it is expected a reduction in the concentration of stresses in the rail's flange due to a larger contact area;
- Rails clamped at both ends with an added mid-span support, but now with an added course steel plate ($142\times30\times5$ mm³) to clamp the rail's web at the mid-span support (Figure 79, Figure 34 and Figure 35);
- Cycling done through load control (same as last setup);
- Pin-joint connection between the loading device and the load cell (same as last setup);
- Strain gauge now placed on the top of the rail's flange (Figure 80);
- Specimens 31 and 32 were tested at 9 kN of maximum load;
- Specimens 33 to 36 were tested at 17.5 kN of maximum load;
- Specimens 37, 38, 41 and 42 were tested at 15 kN of maximum load;
- Specimens 39, 40, 43, and 44 were tested at 12.5 kN of maximum load;
- Specimens 45 to 48 were tested at 10 kN of maximum load;
- Specimens 31 and 32 were reused for monotonic loading (useful for calibrating numerical models).

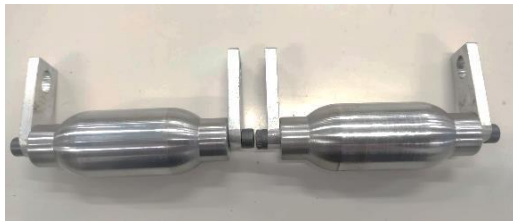With this setup, results were now optimal, i.e., the setup is now able to generate representative fatigue cracks at the rail's web-flange corner due to the shuttle's cyclic loads, shown in Figure 80 (specimen 34 example).

Figure 78 - Load actuators for upward loading scenario setup #3.
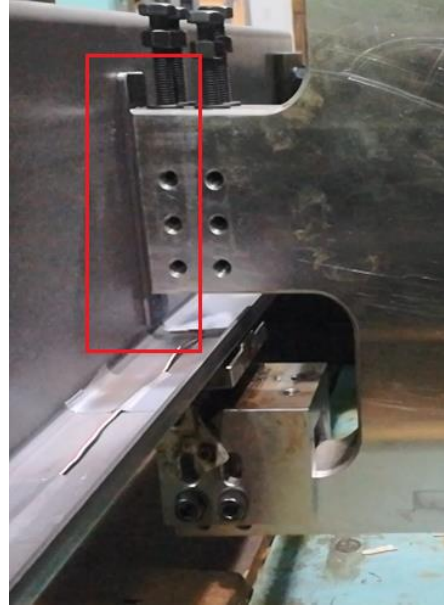
Figure 79 - New steel plate/clamp (red) for upward loading scenario setup #3.

Figure 80 - Representative fatigue cracks (specimen 34 example).

Figure 81 shows the strain gauge's data obtained for the specimens during testing (example for specimens 41 and 42). As stated before, strains were converted into stresses using the constitutive law shown in Equation 15. Also as stated before, for some specimens, the obtained data from the strain gauge was not so well-behaved. In these cases, common sense was used to determine the lifetime of the specimen, combined with visual cues and notes from the laboratory staff (daily visual observations, inspections, and written records on crack development). As an example, in the case of specimens 41 and 42, a lifetime of 180,000 and 240,000 load cycles was determined for each specimen, shown by a significant stress range variation in Figure 81 combined with laboratory staff notes (visual cues on crack development).

As stated above, the strain gauge's data for all specimens is shown in Appendix A. Photographs of the cracked specimens can be seen in Appendix B.
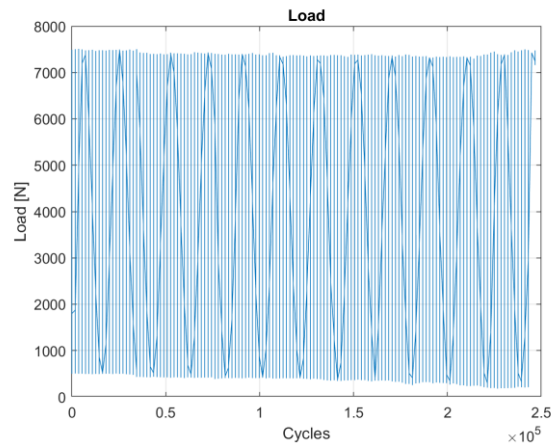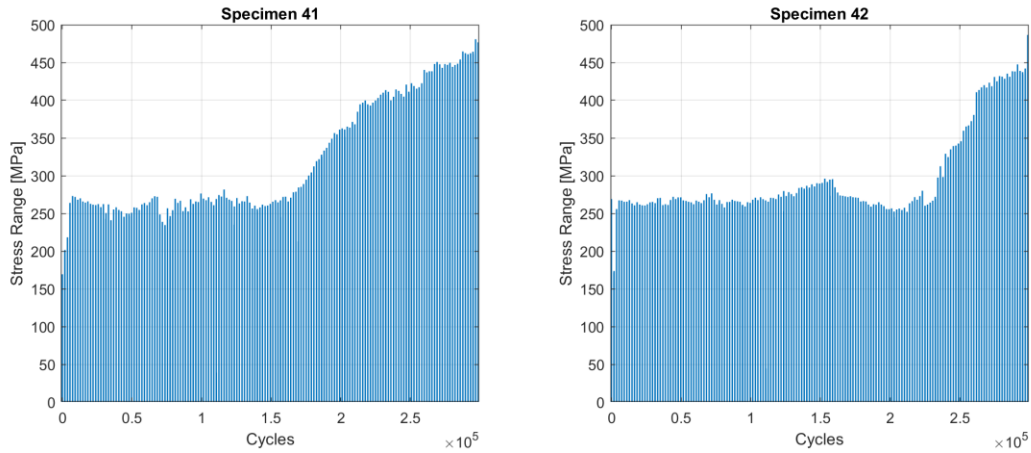
Figure 81 - Strain gauge's data obtained for specimens 41 and 42 (example).

Finally, as done for all the other setups, a numerical simulation replicating the current experimental setup was conducted in Abaqus®. The numerical model was reused from the previous setup, with the updated load actuator's plate and the added steel plate to clamp the rail's web.

Figure 82 presents the results of the mentioned simulation. The figure shows the absolute maximum principal stresses (also known as major principal stresses). Comparing Figure 82 to Figure 77, a slight decrease in the concentration of stresses on the rail's flange is noticeable. Experimental results using this setup were now optimal.
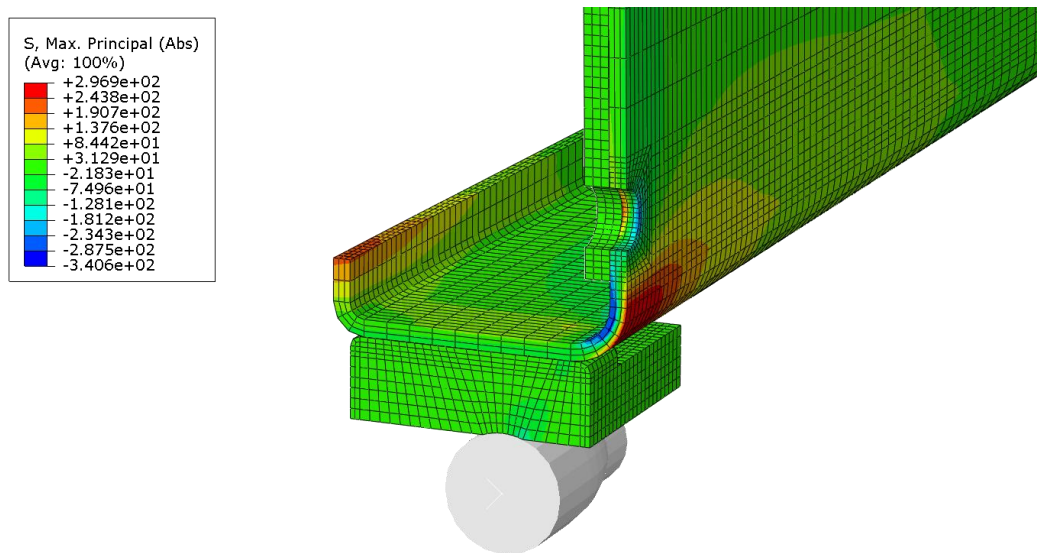
Figure 82 - Numerical simulation of the upward loading scenario setup #3 ($P = 9000$ N).

4.3.   Experimental Fatigue Testing Results

As stated before, Appendix A shows the data gathered by all the specimen's strain gauges, while Appendix B shows photographs of the developed cracks in the rails. Table 4 shows the experimental fatigue testing results for each specimen. Notice that in this table's "Setup" column, the letter D stands for a downward loading scenario setup, while the letter U stands for an upward loading scenario setup.

37

Table 4 - Experimental fatigue testing results.

Setup	Specimen	Maximum Load [N]	Minimum Load [N]	Frequency [Hz]	Load Cycles	Comments
D #1	1	-	-	-	-	Bad results
D #1	2	-	-	-	-	Bad results
D #2	3	-	-	-	-	Bad results
D #2	4	-	-	-	-	Bad results
D #3	5	-	-	-	-	Bad results
D #3	6	-	-	-	-	Bad results
D #4	7	5,000	500	3	325,000	Outlier
D #4	8	5,000	500	3	5,000,000	Run out
D #4	9	5,000	500	3	5,000,000	Run out
D #4	10	5,000	500	3	5,000,000	Run out
D #4	11	7,500	750	3	160,000	-
D #4	12	7,500	750	3	120,000	-
D #4	13	7,500	750	3	200,000	-
D #4	14	7,500	750	3	95,000	-
D #4	15	-	-	-	-	Monotonic
D #4	16	-	-	-	-	Monotonic
D #4	17	9,000	900	2	75,000	-
D #4	18	9,000	900	2	42,500	-
D #4	19	6,250	625	3	580,000	-
D #4	20	6,250	625	3	325,000	-
D #4	21	9,000	900	2	90,000	-
D #4	22	9,000	900	2	45,000	-
D #4	23	6,250	625	3	220,000	-
D #4	24	6,250	625	3	120,000	-
D #4	49	5,500	550	3	550,000	-
D #4	50	5,500	550	3	800,000	-
U #1	25	-	-	-	-	Bad results
U #1	26	-	-	-	-	Bad results
U #1	27	-	-	-	-	Monotonic
U #1	28	-	-	-	-	Monotonic
U #2	29	-	-	-	-	Bad results
U #2	30	-	-	-	-	Bad results
U #3	31	9,000	900	2	5,000,000	Run out
U #3	32	9,000	900	2	5,000,000	Run out
U #3	31	-	-	-	-	Monotonic

U #3	32	-	-	-	-	Monotonic
U #3	33	17,500	1,750	1	45,000	-
U #3	34	17,500	1,750	1	62,000	-
U #3	35	17,500	1,750	1	22,000	-
U #3	36	17,500	1,750	1	64,000	-
U #3	37	15,000	1,500	2	200,000	-
U #3	38	15,000	1,500	2	255,000	-
U #3	39	12,500	1,250	3	850,000	-
U #3	40	12,500	1,250	3	700,000	-
U #3	41	15,000	1,500	2	180,000	-
U #3	42	15,000	1,500	2	240,000	-
U #3	43	12,500	1,250	3	550,000	-
U #3	44	12,500	1,250	3	645,000	-
U #3	45	10,000	1,000	3	550,000	-
U #3	46	10,000	1,000	3	650,000	-
U #3	47	10,000	1,000	3	700,000	-
U #3	48	10,000	1,000	3	900,000	-

CHAPTER 5:   ROLL-FORMING SIMULATION OF THE Z-RAIL

The current chapter presents the numerical simulations of the cold roll-forming fabrication process to obtain the Z-rail with internal residual stresses. These simulations were carried out using COPRA® and Marc®.

The COPRA® software is mostly responsible for defining the geometric properties of the roll-forming machine, i.e., in COPRA®, the user defines all the stations of the machine, including the geometry of all the rolls, as well as the distances between each station. With this information, COPRA® then creates a Marc® model where the roll-forming machine is put in place, as well as the metal strip to be roll-formed. COPRA® also discretizes (or meshes) the strip and defines contact interactions between it and the rolls. Finally, COPRA® also creates all the necessary load cases for the simulation.

The Marc® software uses the Finite Element Method to numerically simulate the cold roll-forming fabrication process. As stated above, Marc® uses the roll-forming machine (rolls) and the already discretized (or meshed) metal strip from COPRA®. COPRA® is also responsible for defining the contact interactions between the strip and the rolls, as well as all necessary load cases for the base simulation. In Marc®, the user can further specify the strip's material, as well as various other parameters, like isotropic or kinematic material hardening rules, element type to be used, extra load cases, solver options, etc.

5.1.   Base Model

The first step to establish the base model for the numerical simulations of the cold roll-forming fabrication process is to define the roll-forming machine stations and rolls. For this step, the manufacturer made available the CAD drawings of each individual station. These drawings were then referenced when drawing the roll-forming stations and their rolls in COPRA®, replicating the real roll-forming machine. Appendix C presents all stations and rolls that were defined in COPRA®. Using these stations and rolls, Figure 83 presents the obtained Z-rail's roll-forming flower. It should be noted that special care was taken to guarantee that the strip's width (279.21 mm, calculated by COPRA®) and thickness (3.5 mm) remained constant for all stations. Finally, Table 5 shows additional details for the roll-forming machine stations.
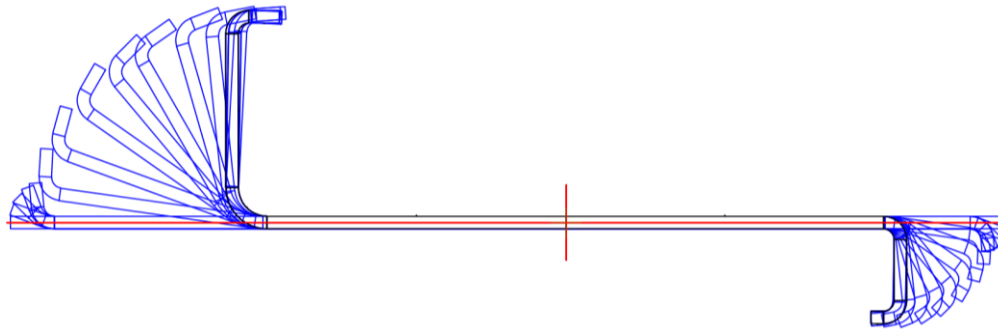
Figure 83 - Z-rail's roll-forming flower.

Table 5 - Roll-forming machine stations.

Station Number	Station Type	Distance to Last [mm]	Distance to First [mm]
1	Entry guide	0	0
2	Forming	500	500
3	Forming	500	1,000
4	Forming	500	1,500
5	Forming	500	2,000

40

6	Forming	500	2,500
7	Forming	500	3,000
8	Forming	500	3,500
9	Forming	500	4,000
10	Forming	500	4,500
11	Forming	500	5,000
12	Forming	500	5,500
13	Forming	500	6,000
14	Calibrating	1,000	7,000
15	Calibrating	700	7,700
16	Forming	300	8,000
17	Calibrating	300	8,300
18	Calibrating	348	8,648

The base model also consists on an initial strip with twice the length of the intended rail's final length. After the roll-forming process, the 1800 mm strip is cut to obtain the 900 mm rail (Figure 90).

After defining every station of the machine and the strip's initial length, the next step in COPRA® is to mesh the strip. The strip is meshed according to four parameters:

- Number of subdivisions of straight entities;
- Number of subdivisions of arc entities;
- Number of subdivisions in the roll-direction;
- Number of element layers across the thickness.

The straight and arc entities of the strip's section can be obtained considering the section at any specified station or considering all stations simultaneously, the latter option was used (Figure 84). Figure 85 shows a slice of the meshed strip, which shows a higher mesh refinement in the bend-zones. The mesh is comprised of continuum hexahedral elements with 8 nodes and 8 integration points (full integration). Finally, in the base model, 3 element layers were used across the thickness of the strip, which results in 31,365 elements and 42,848 nodes.

Figure 84 - Strip's straight (red) and arc (blue) entities considering all stations simultaneously.
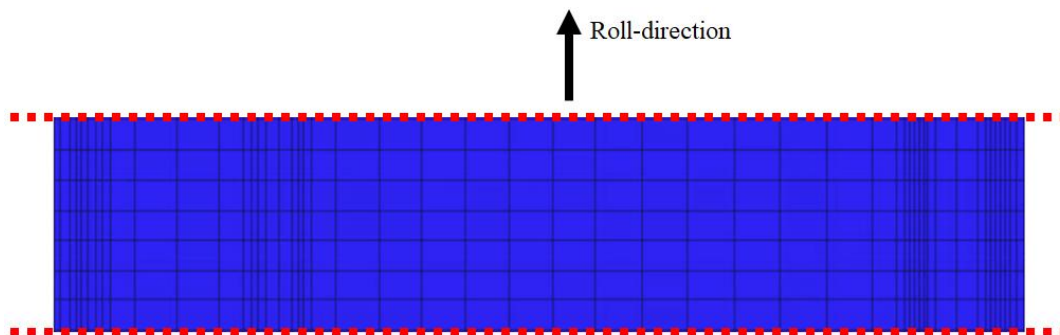
Figure 85 - Slice of the meshed strip.

The base model also consists in the S355MC material, whose elastoplastic properties have been presented in Chapter 3. The von Mises yield criterion was considered, as well as an isotropic hardening rule.

In the numerical model, the rolls are considered as non-deformable rigid analytical parts. The normal hard contact interactions between the strip and the rolls are automatically defined by COPRA®. The tangential contact was also considered frictionless since the strip is fixed in place and the rolls move towards the strip without rolling (a common simplification of the roll-forming fabrication process).

Finally, COPRA® automatically defines the boundary conditions necessary to eliminate any rigid-body movements of the strip. These three boundary conditions consist in the following:

- In the first 3 rows of nodes on the end of the strip, the middle nodes of the rows are constrained to not move in the *x* direction (total of 12 nodes, Figure 86);
- In the first 3 rows of nodes on the end of the strip, the middle nodes on the bottom are constrained to not move in the *y* direction (total of 3 nodes, Figure 87);
- Displacement in the *z* direction (rolling-direction) is constrained on both ends of the strip (Figure 88).
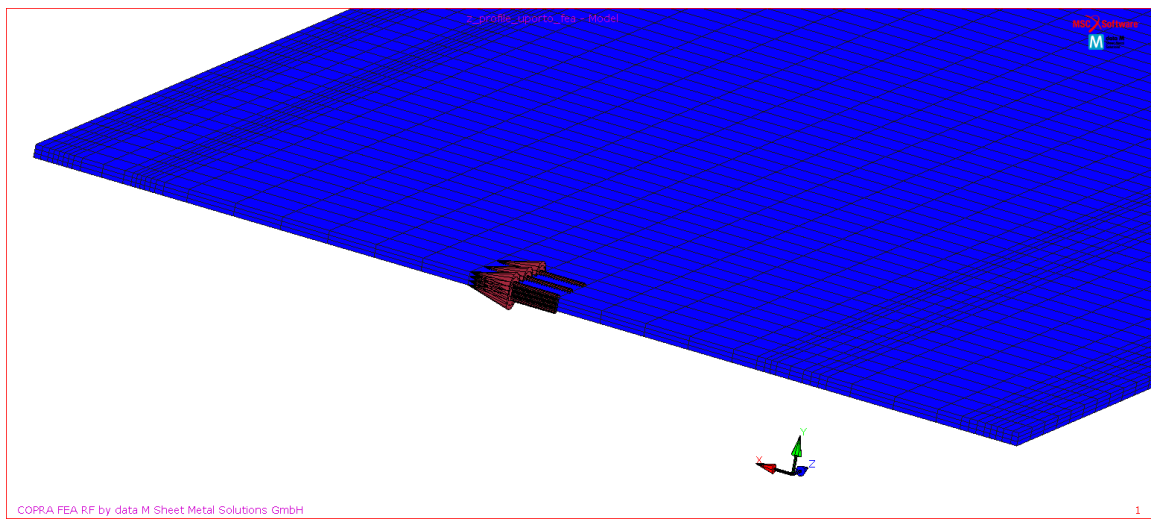
Figure 86 - Constrained U1 on the end of the strip (12 nodes).
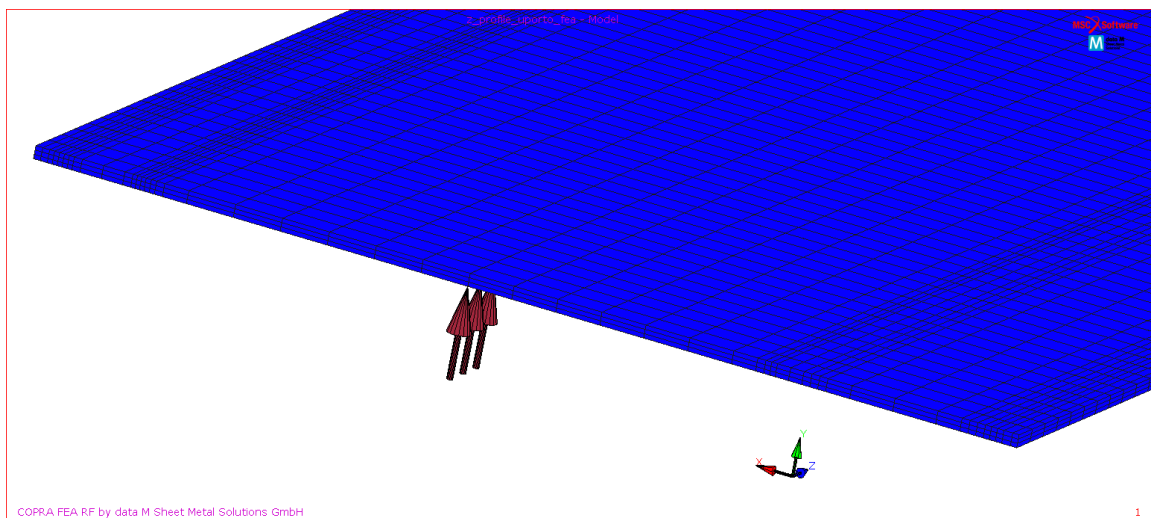
Figure 87 - Constrained U2 on the end of the strip (3 nodes).
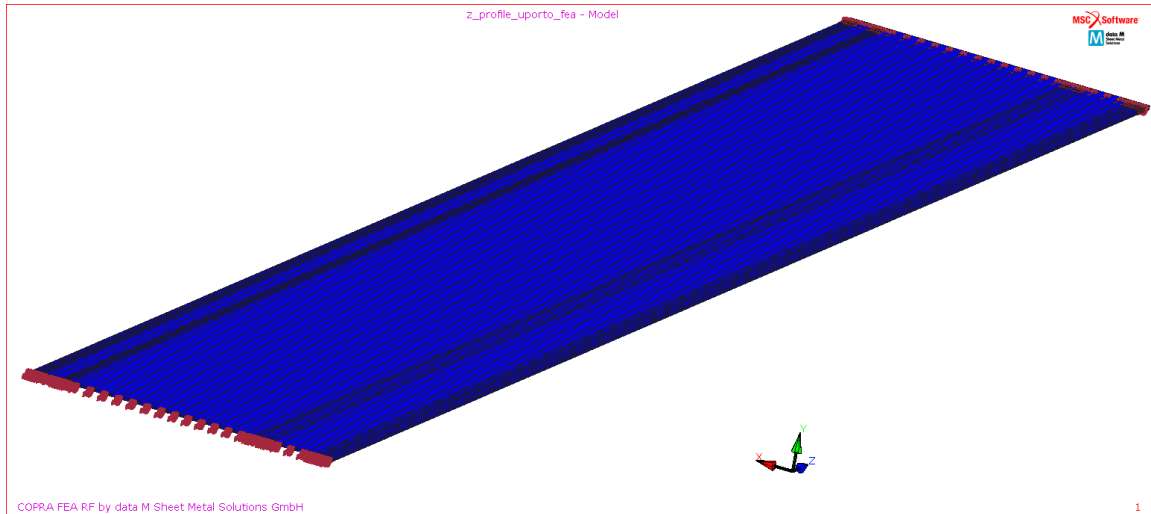
Figure 88 - Constrained U3 on both ends of the strip.

The base model is now established, and simulations are ready to run. Figure 89 shows the numerical model of the roll-forming fabrication process to obtain the Z-rail in its initial state.
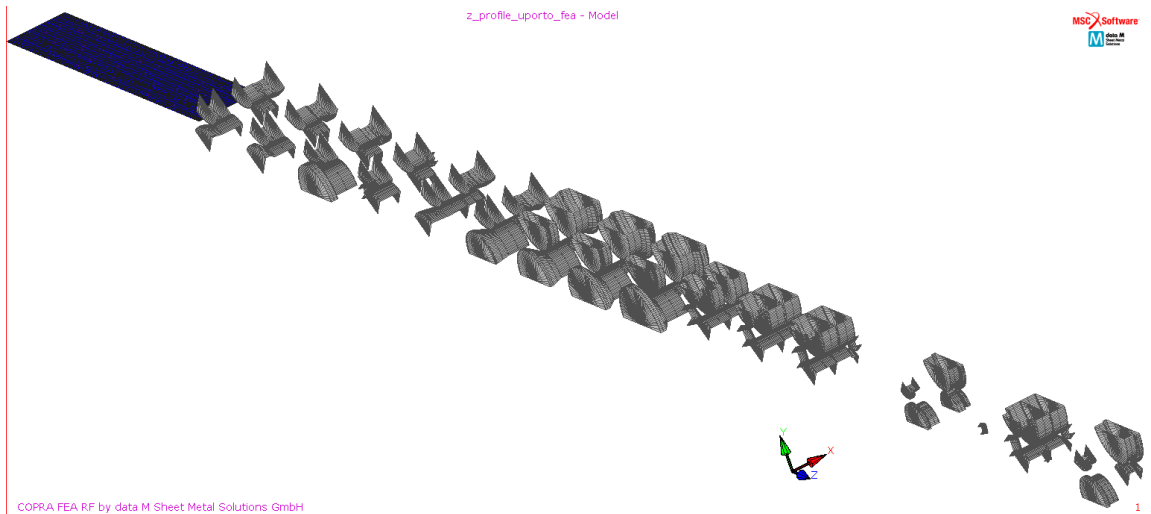
Figure 89 - Numerical model of the roll-forming fabrication process to obtain the Z-rail.

Figure 90 and Figure 91 show the obtained Z-rail from the presented model. As mentioned before, a final load step to cut the Z-rail is done in order to eliminate unwanted deformations in the strip's ends (as done in real life). In Figure 90, the total equivalent plastic strain is shown. This scalar field shows that the parts of the strip most plasticized were the bends, as expected. Figure 91 shows the section of the obtained Z-rail.

For future plotting purposes, Figure 93 shows the paths defined along the rail's section thickness, at the rail's web-flange corner, while Figure 94 shows the paths defined along the section's inner and outer surfaces.

The most relevant residual stresses to be analyzed are the tangential (also called transversal) and longitudinal residual stresses. To obtain these residual stresses, an element-local coordinate system was

used for each element (Figure 92). Referencing this coordinate system, residual tangential stresses are the ones along the *x* axis, and residual longitudinal stresses are the ones along the *z* axis.
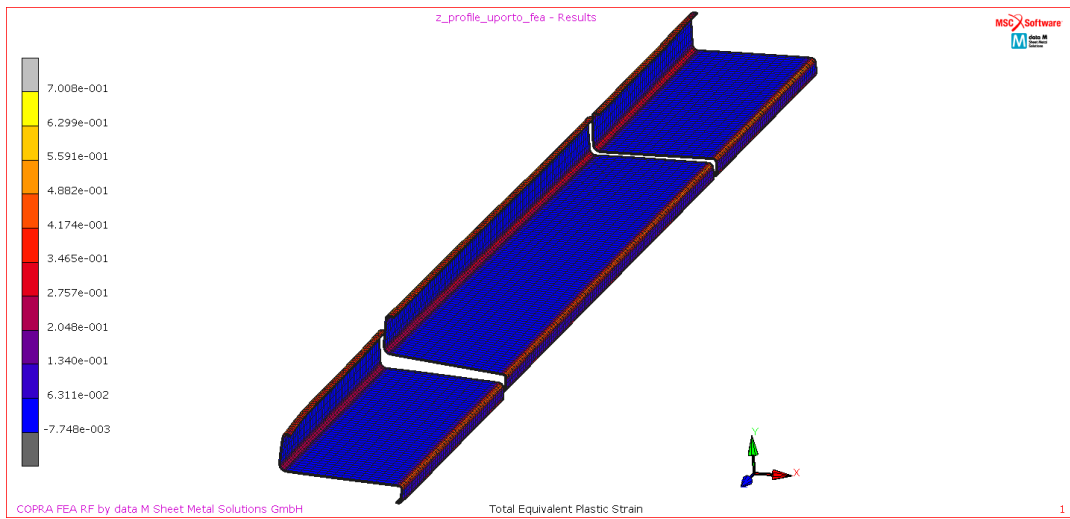
Figure 90 - Obtained Z-rail.
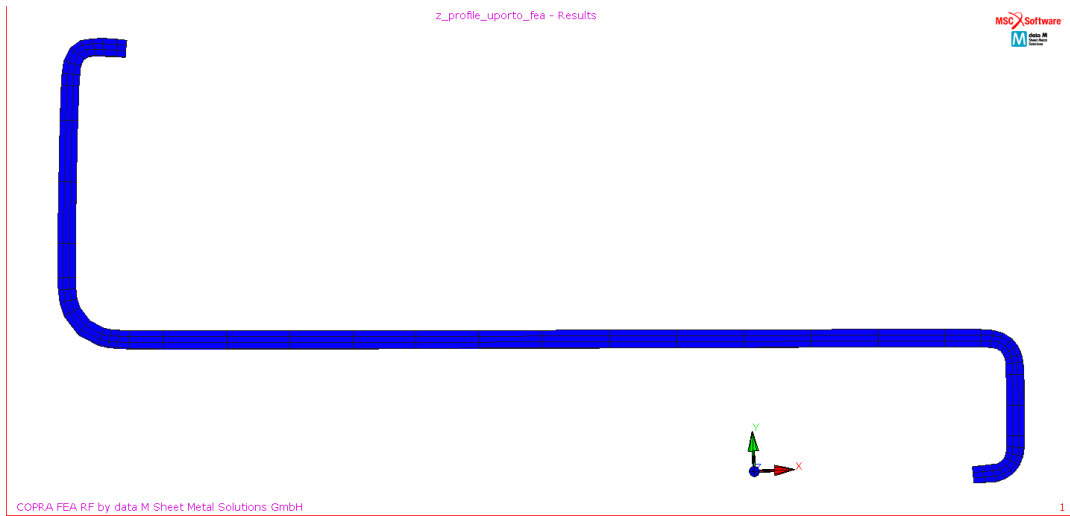
Figure 91 - Obtained Z-rail's section.
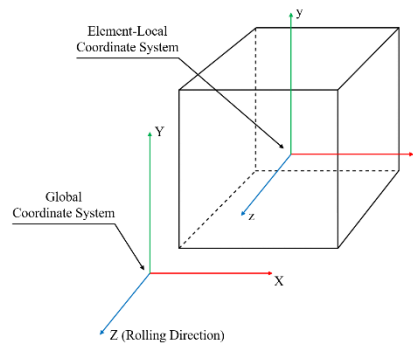
Figure 92 - Global and element-local coordinate systems (pre-forming).
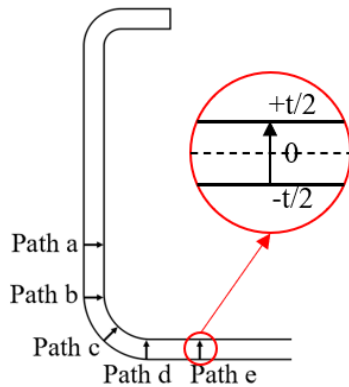
Figure 93 - Definition of paths along the section thickness (web-flange corner).
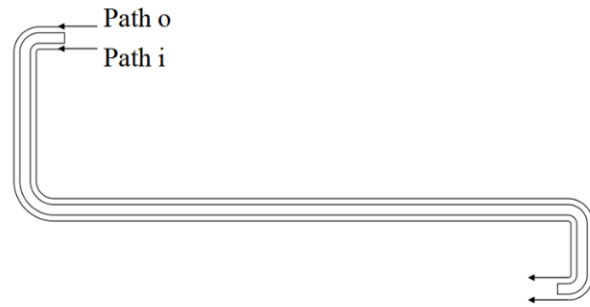
Figure 94 - Definition of paths along the section's inner and outer surfaces.

5.2. Number of Element Layers

The first set of simulations based on the presented base model were used to determine the optimal number of element layers to use on the meshed strip. Three models were constructed, with strips of 2, 3, and 4 element layers.

5.2.1. Results Across the Thickness

Referencing Figure 93, Figure 95 to Figure 100 present the results for the tangential and longitudinal residual stresses across the rail's web-flange corner, where fatigue failure occurred during experimental testing.

As shown by Figure 95 and Figure 96, 2 element layers is not enough to fully capture the residual stresses across the thickness. However, reasonable results are obtained on the surfaces (-0.5 and +0.5 of the normalized thickness).

As shown by Figure 97 and Figure 98, the model with 3 element layers presents the best results, where a smooth transition of stress values can be seen between the various paths. This model also presents similar results between paths a and e, and paths b and d, which is expected due to the symmetry of the corner. Finally, in this model, paths a and e present the lowest absolute stress values, paths b and d present the second lowest absolute stress values, and path c presents the highest absolute stress values. This is also expected considering the symmetry and distance from the paths to the middle of the corner (where path c passes right through the middle).

Lastly, as shown by Figure 99 and Figure 100, the model with 4 element layers presents more unwanted scatter in the results compared to the model with just 3 element layers, which was not expected.

Figure 95 - Tangential residual stresses across the thickness (2 element layers).

Figure 96 - Longitudinal residual stresses across the thickness (2 element layers).

Figure 97 - Tangential residual stresses across the thickness (3 element layers).

Figure 98 - Longitudinal residual stresses across the thickness (3 element layers).
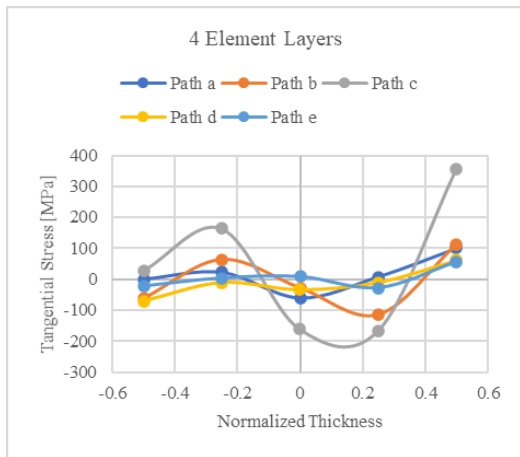
Figure 99 - Tangential residual stresses across the thickness (4 element layers).
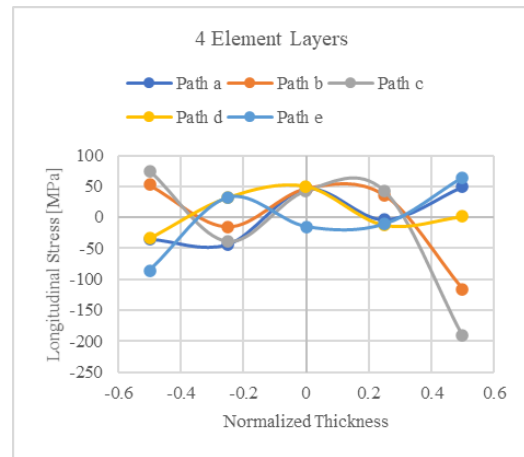
Figure 100 - Longitudinal residual stresses across the thickness (4 element layers).

46

5.2.2. Results Across the Width

Referencing Figure 94, Figure 101 to Figure 104 show the results for the tangential and longitudinal residual stresses across the section's inner and outer surfaces.

As shown by the figures, the three models present roughly the same tendencies of higher absolute stress values in the section's bend-zones.
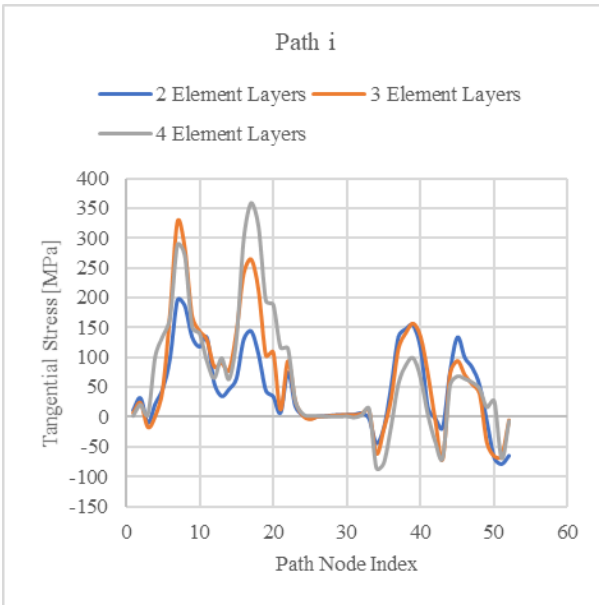
Figure 101 - Tangential residual stresses across the width (path i).
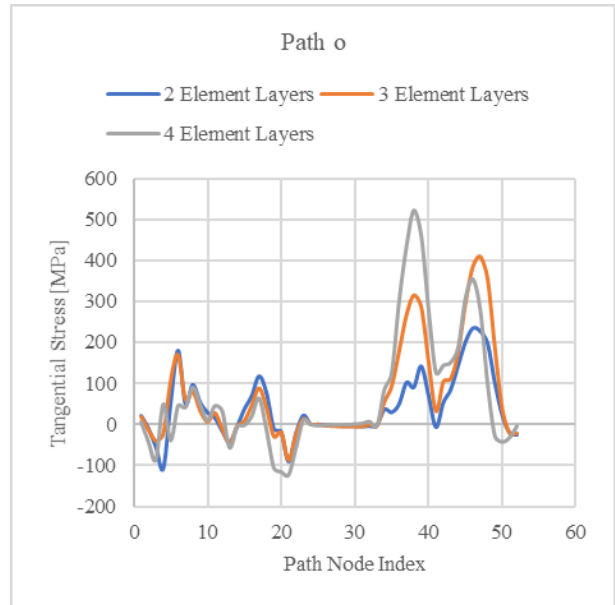
Figure 102 - Tangential residual stresses across the width (path o).
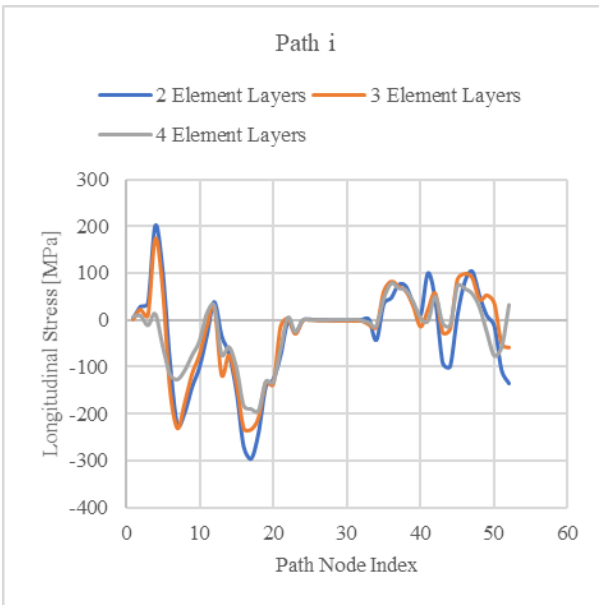
Figure 103 - Longitudinal residual stresses across the width (path i).
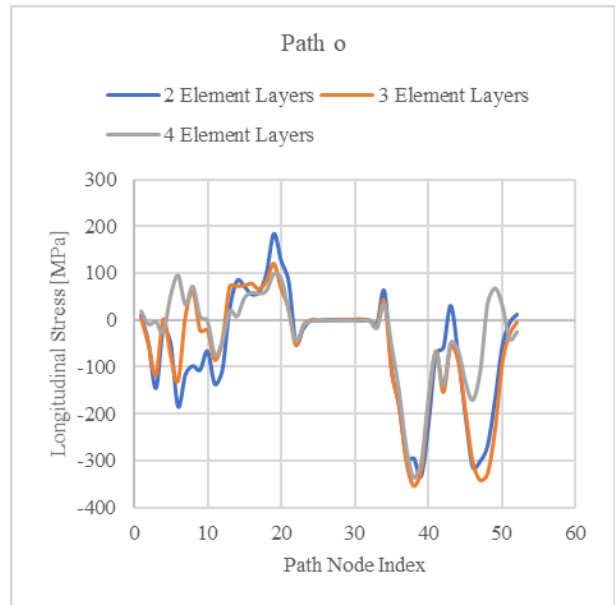
Figure 104 - Longitudinal residual stresses across the width (path o).

5.3.   Isotropic vs. Kinematic Hardening

The next set of simulations conducted based on the presented base model were two simulations to determine the differences in results between using isotropic or kinematic material hardening rules. For this, an additional numerical model was created, identical to the base model, but now considering a kinematic hardening rule.

5.3.1.   Results Across the Thickness

Referencing Figure 93, Figure 105 to Figure 108 present the results for the tangential and longitudinal residual stresses across the rail's web-flange corner. As shown by the images, differences in the results, between isotropic and kinematic hardening rules, are evident. The kinematic hardening rule results in smoother stress values with less distinction between paths.
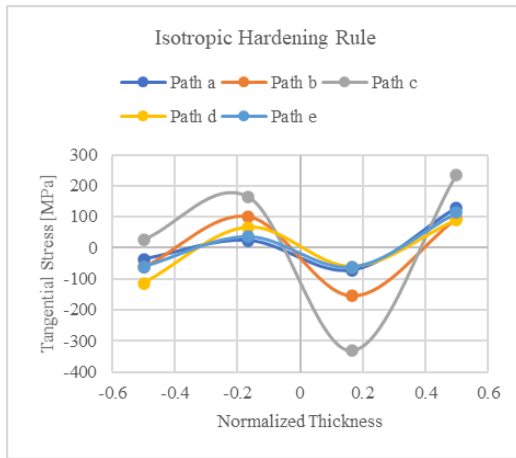
Figure 105 - Tangential residual stresses across the thickness (isotropic hardening rule).
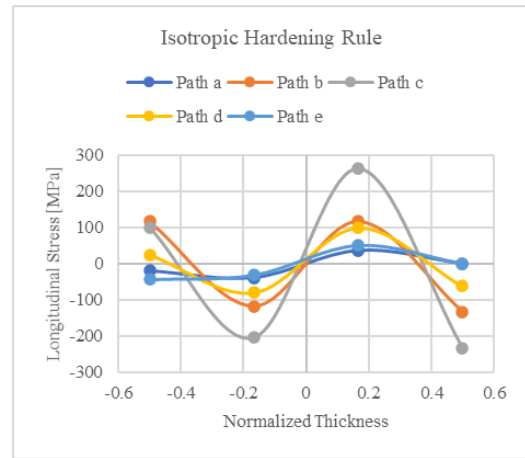
Figure 106 - Longitudinal residual stresses across the thickness (isotropic hardening rule).
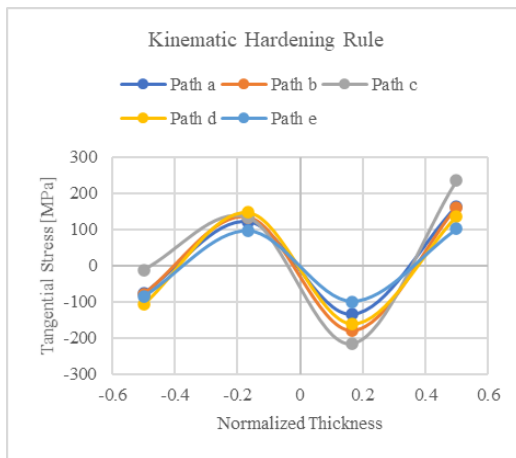
Figure 107 - Tangential residual stresses across the thickness (kinematic hardening rule).
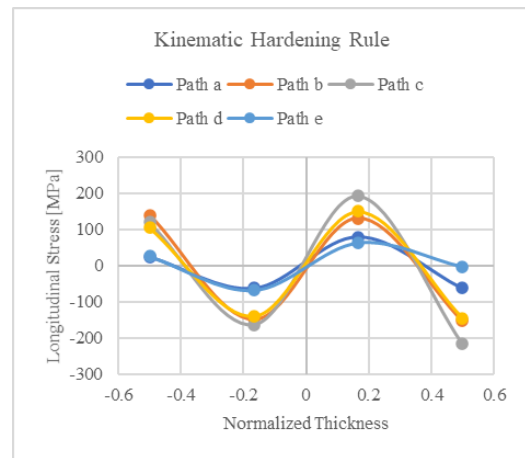
Figure 108 - Longitudinal residual stresses across the thickness (kinematic hardening rule).

5.3.2.   Results Across the Width

Referencing Figure 94, Figure 109 and Figure 110 show the results for the tangential and longitudinal residual stresses across the section's inner and outer surfaces. As shown by the figures, isotropic and

kinematic hardening rules produce similar trends, but for isotropic hardening, higher absolute stress values can be seen in the section's bend-zones.
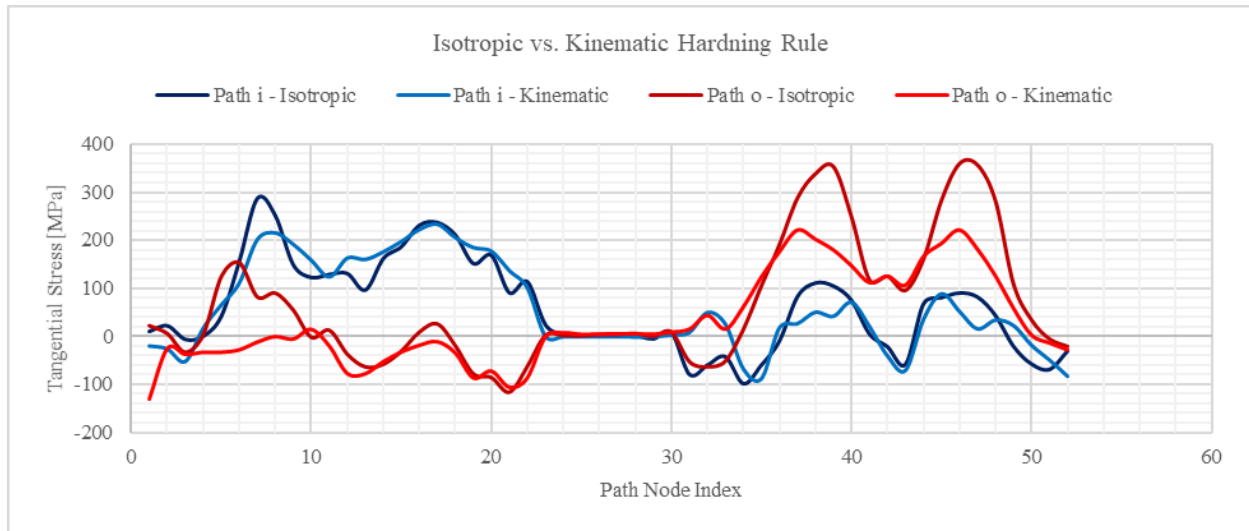
Figure 109 - Tangential residual stresses across the width (isotropic vs. kinematic hardening rules).
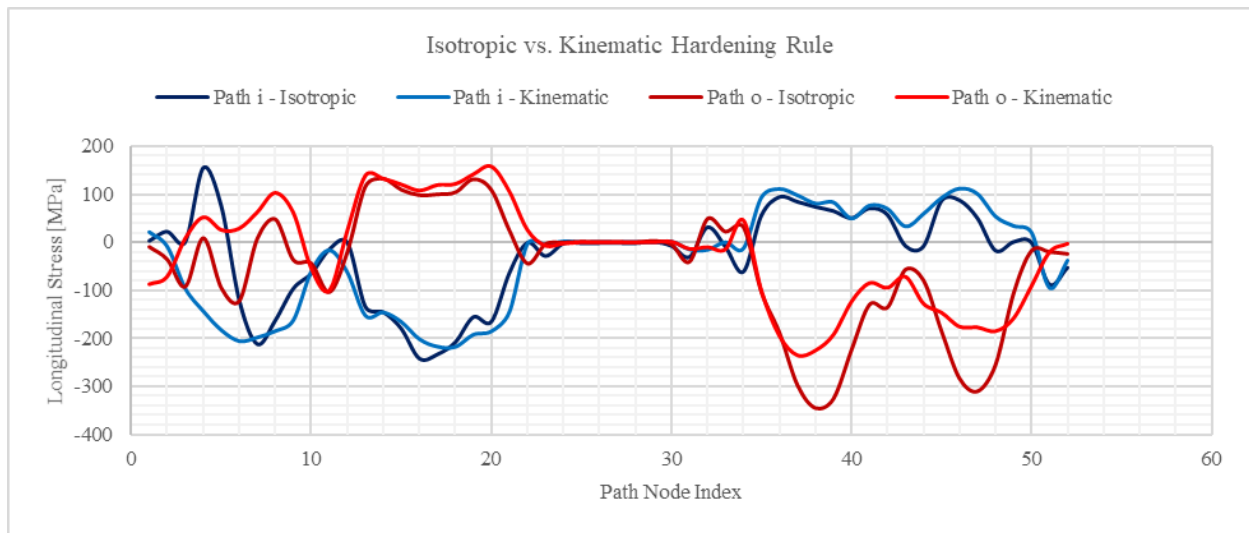
Figure 110 - Longitudinal residual stresses across the width (isotropic vs. kinematic hardening rules).

5.4.   Final Cut vs. Pre-Cut Strip

The next set of simulations consisted in the following models:

- The base model, where the initial strip has twice the length of the intended rail's final length. After the roll-forming process, the 1800 mm strip is cut to obtain the 900 mm rail. As stated before, the strip on this model is meshed with 31,365 elements and 42,848 nodes;
- An identical model, but now the initial strip has already the final length of the rail (900 mm). With this model, the strip is meshed with 15,606 elements and 21,424 nodes. This model will be referenced as the "pre-cut model". In this model, the final cut is avoided.

Using the same CPU, with the base model, the simulation time was around 2 weeks, while using the pre-cut model, the simulation time was greatly reduced to less than 2 days. Obviously, this is a huge advantage for the pre-cut model. However, the pre-cut model is also less numerically stable, for example, for the previous study of isotropic versus kinematic hardening rules, the pre-cut model failed to converge to a solution in Marc® while using a kinematic hardening rule, but the base model converged with no problems. This numerical instability is most likely due to the fact that, in the pre-cut model, the strip is sometimes in contact with just 1 roll-forming station, while in the base model the strip is always in contact with 3 roll-forming stations.

5.4.1. Results Across the Thickness

Referencing Figure 93, Figure 111 to Figure 114 present the results for the tangential and longitudinal residual stresses across the rail's web-flange corner. As shown by the images, differences in the results, between using the base model or the pre-cut model, are not very significant, justifying the lighter model.
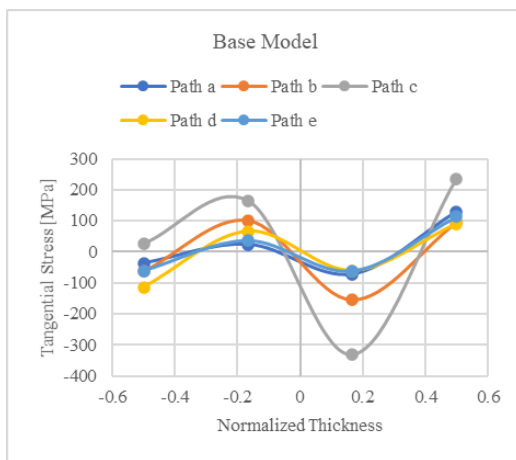
Figure 111 - Tangential residual stresses across the thickness (base model).
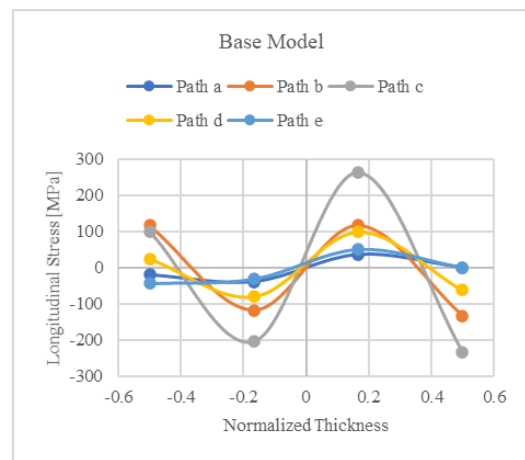
Figure 112 - Longitudinal residual stresses across the thickness (base model).
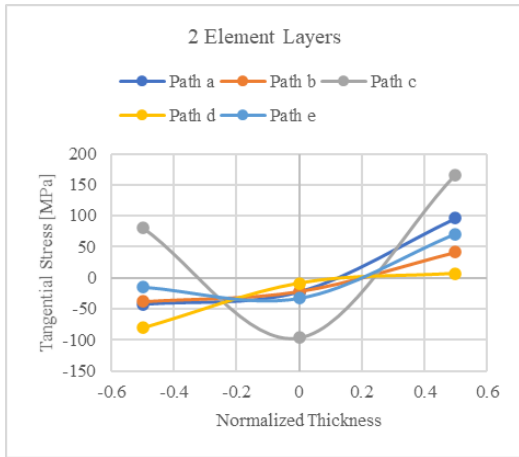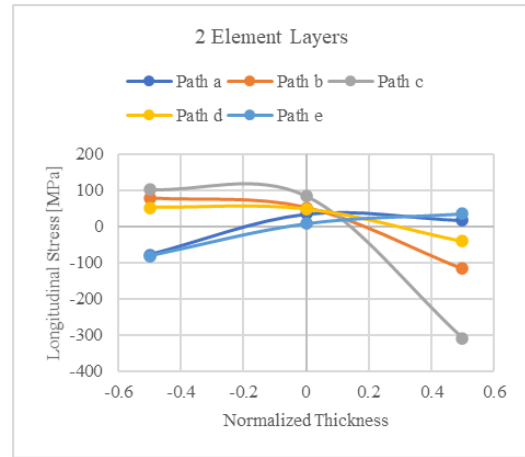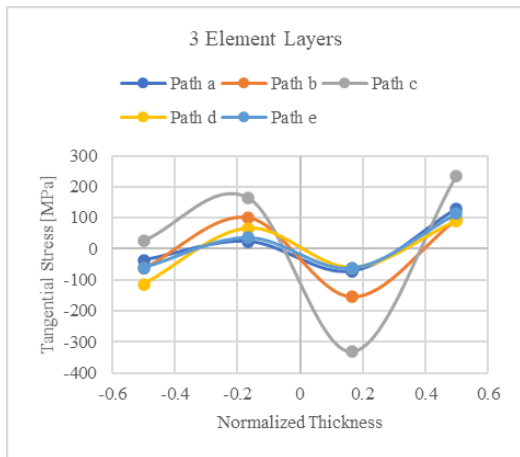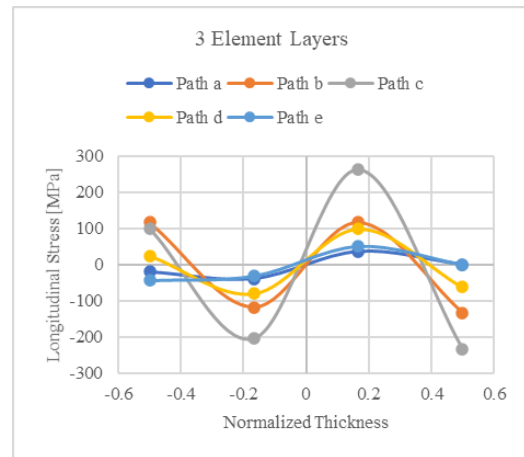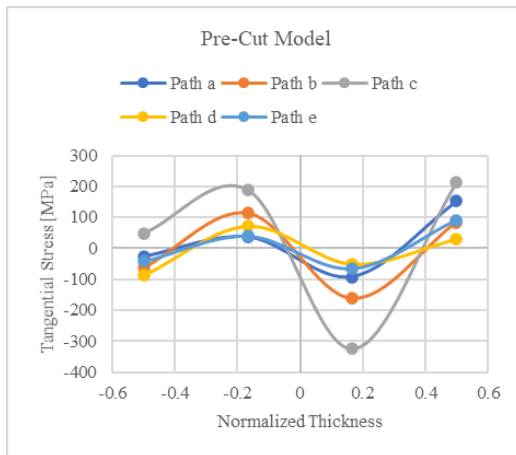

Figure 113 - Tangential residual stresses across the thickness (pre-cut model).
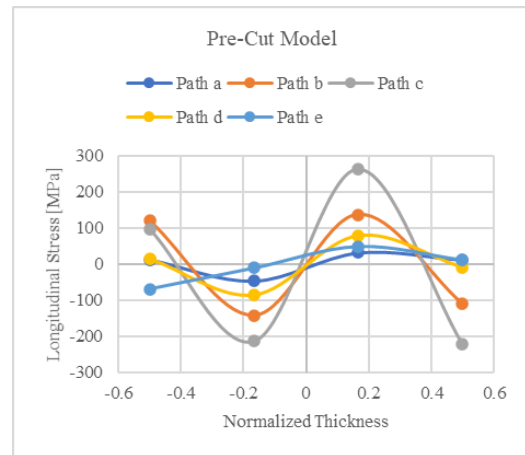
Figure 114 - Longitudinal residual stresses across the thickness (pre-cut model).

5.4.2. Results Across the Width

Referencing Figure 94, Figure 115 and Figure 116 show the results for the tangential and longitudinal residual stresses across the section's inner and outer surfaces. As shown by the figures, differences in the results, between using the base model or the pre-cut model, are not very significant, justifying again the lighter model.
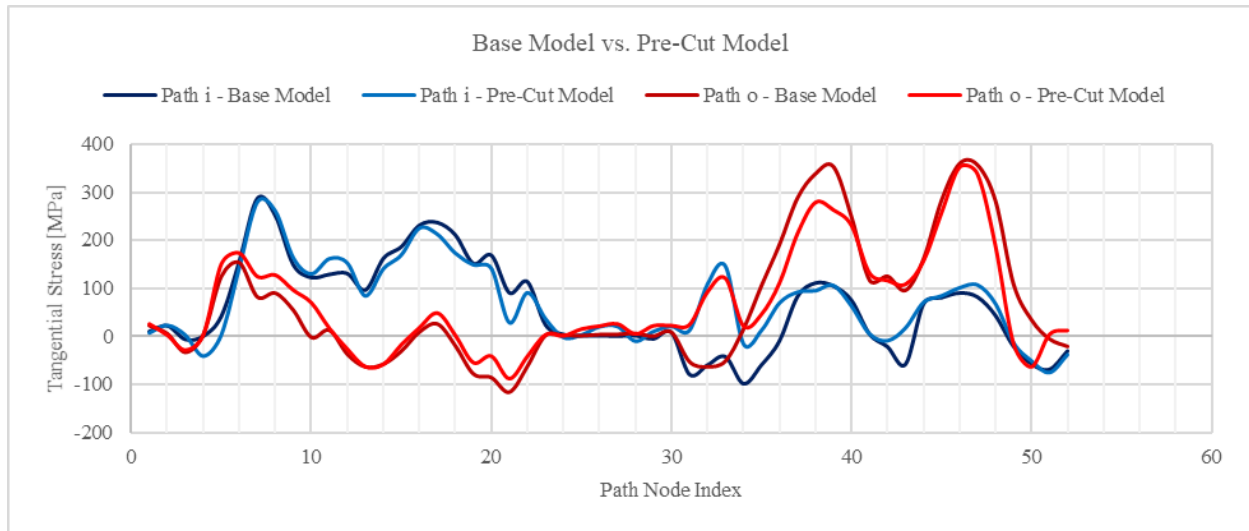
Figure 115 - Tangential residual stresses across the width (base model vs. pre-cut model).
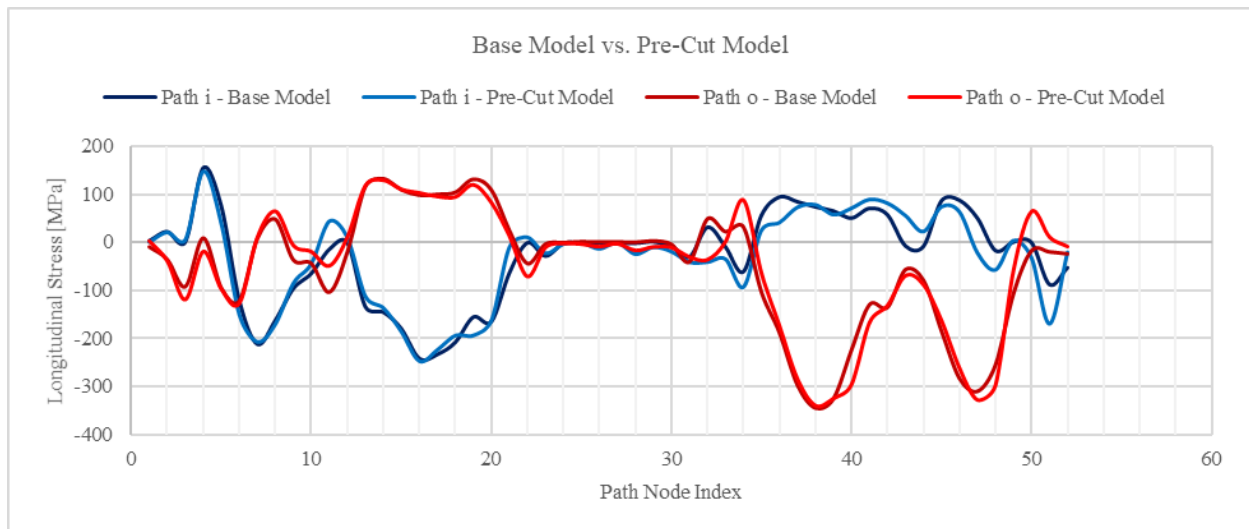
Figure 116 - Longitudinal residual stresses across the width (base model vs. pre-cut model).

5.5.   Numerical vs. Experimental Residual Stress Results (Validation)

Experimental residual stress results were obtained at the University of Burgos (a FASTCOLD project partner) using Hole Drilling (HD) and X-Ray Diffraction (XRD) techniques to obtain the values of the residual stresses of the rail.

The hole drilling technique obtains the residual stress values by drilling in the rail's flange, near the web-flange corner (between paths a and b in Figure 93). The X-ray diffraction technique obtains the residual stress values located in the middle of the web-flange corner (path c in Figure 93), in the outer surface only.

5.5.1. Tangential Residual Stresses

Referencing Figure 93, Figure 117 shows the comparison between tangential residual stresses obtained through numerical and experimental procedures. As shown by the figure, a satisfactory agreement is found between the experimental and the numerical results. However, one may notice some scatter in the experimental data.
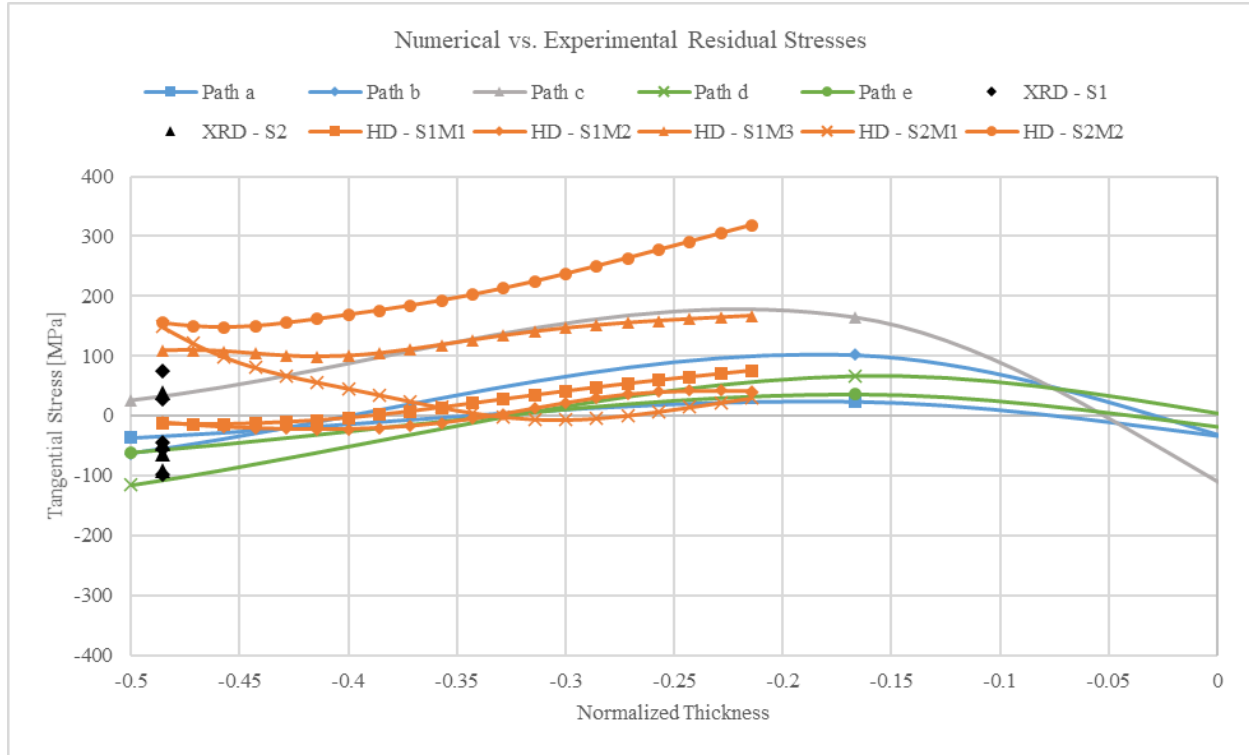
Figure 117 - Tangential residual stresses across the thickness (numerical vs. experimental results, S-Specimen, M-Measurement).

5.5.2. Longitudinal Residual Stresses

Referencing Figure 93, Figure 118 shows the comparison between longitudinal residual stresses obtained through numerical and experimental procedures. As shown by the figure, and contrary to the tangential residual stresses results, with the longitudinal residual stresses, no acceptable correlation can be observed in the results.

This can possibly be explained due to the fact that in the numerical model used to simulate the cold roll-forming fabrication process to obtain the Z-rail, the coiling and uncoiling of the initial metal strip is not considered. It is expected that the coiling and uncoiling of the strip alters the longitudinal residual stresses in the final rail.

However, it must be noted that the tangential residual stresses are the most important ones for future fatigue analyses of the Z-rail, and these stresses correlate well with the obtained experimental data.

In reality, coiling and uncoiling effects are difficult to account for since many coiling-uncoiling cycles are applied to the strip, from the production of the raw material up to the final uncoiling and flattening to the

roll-forming mill. This number of cycles may also vary if the strip is coated or painted before the roll-forming process. However, due to the Poisson effect, longitudinal residual stresses (due to coiling-uncoiling cycles) should affect transversal residual stresses.

Finally, one can see large dispersions between experimental results.
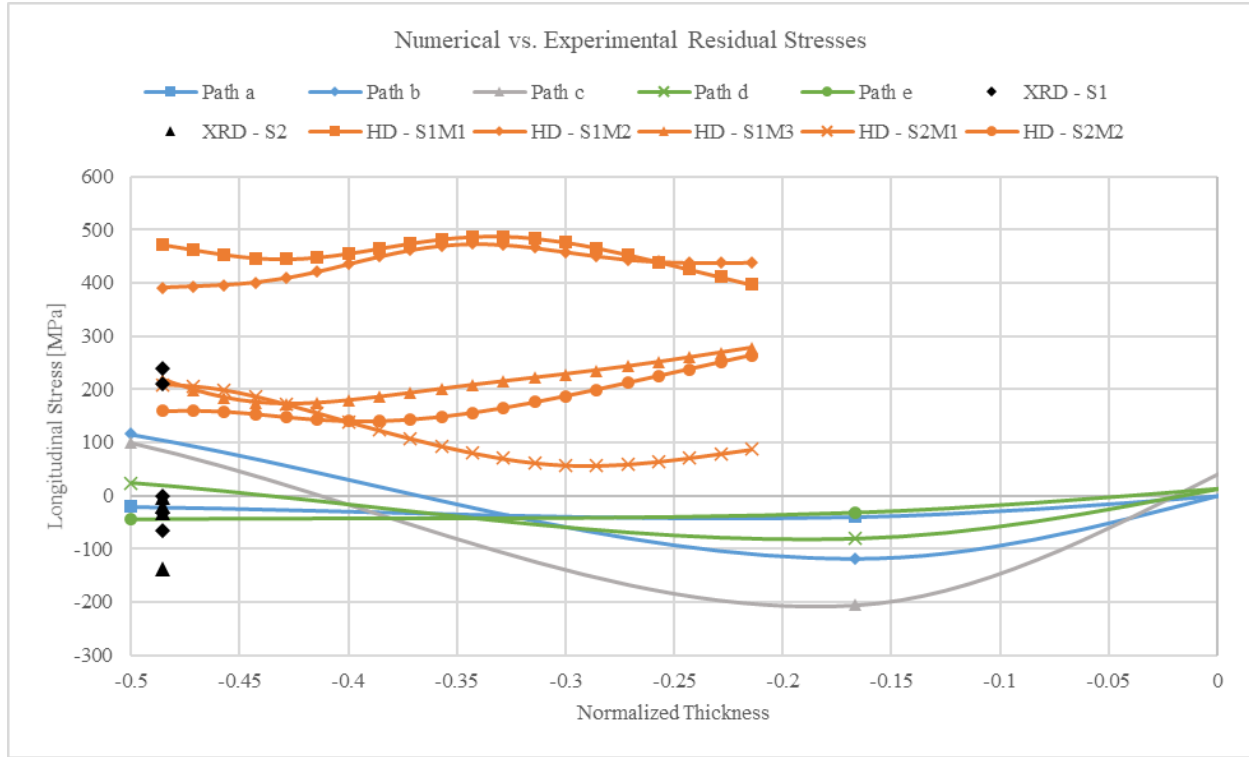
Figure 118 - Longitudinal residual stresses across the thickness (numerical vs. experimental results, S-Specimen, M-Measurement).

CHAPTER 6: Z-RAIL STRESS ANALYSIS - PARAMETRIC STUDY

In this chapter, a parametric study conducted on the Z-rail is presented. The aim of this study is to obtain equations which relate certain parameters with the stresses obtained by loading the Z-rail. The base of this study is a series of numerical simulations conducted in Abaqus®.

The purpose of this study is to provide simple tools (in the form of mathematical equations) to compute the elastic stresses on the profile without accounting for the previous manufacturing residual stresses.

The base 3D finite element model used for these numerical simulations consists on a Z-rail fixed on both ends, with an applied point load at the mid-span of the rail, on its larger flange. The model also considers the symmetry of the rail (only half of the total length is modeled). The S355MC material used was considered elastic (elastic properties presented in Chapter 3). The model also considers non-linear geometry effects. The rail was discretized with the C3D8 element, a continuum hexahedral element with 8 nodes and 8 integration points (full integration). Finally, in the base model, the rail has a total length of 880 mm (distance between holes, Figure 23).

Figure 119 shows the base finite element model in Abaqus®. Figure 120 shows the mesh of the base model, more refined towards the location of the point load.
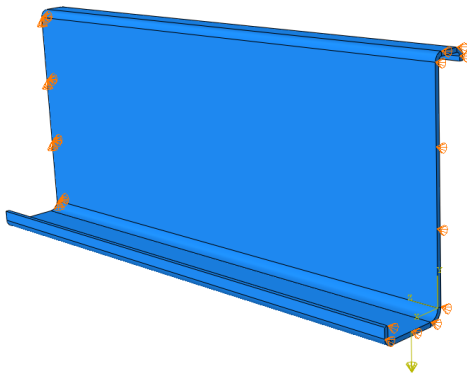
Figure 119 - Base finite element model for the parametric study.
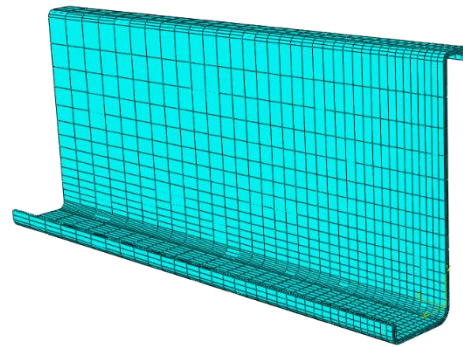
Figure 120 - Base finite element model for the parametric study (mesh).

It should be noted that the model is purposefully simplified, i.e., unlike in the previously presented experimental setups, no load actuator was used (thus, no contact interactions). The boundary conditions were also kept simple (no mid-span support). This is intentional to reduce the number of parameters to be analyzed. Furthermore, after fatigue analysis, it should be interesting to compare results between using a numerical model replicating the experimental conditions versus using the equations obtained through the parametric study based on simpler models.

6.1.   Moment of Force (Force Magnitude and Distance to the Web)

The first parameters to be analyzed were the force magnitude, P, and the distance between it and the rail's web-wall, d, which could be combined as the force moment, M:

$$M = P \cdot d$$

<div align="right">**Equation 16**</div>

While varying these parameters, the presented base model was used to extract the maximum value of the maximum principal stresses, S_1^{max}, located in the web-flange corner, where cracking occurred during experimental fatigue testing.

As usual, two loading scenarios were analyzed, an upward and a downward loading scenario. Figure 121 shows the mentioned parameters for both loading scenarios.
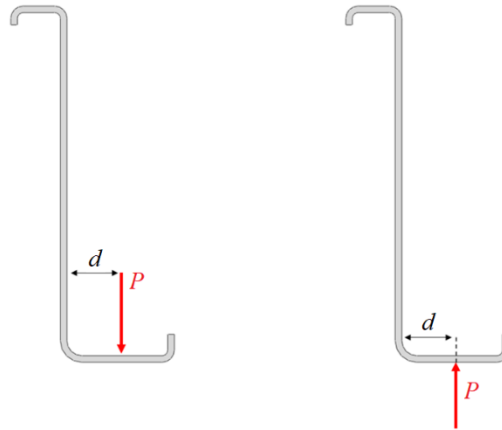
Figure 121 - Downward (left) and upward (right) loading scenarios (parameters *P* and *d*).

6.1.1. Downward Loading Scenario

Table 6 presents the stress results extracted from the mentioned base model. Based on the presented table, Figure 122 and Figure 123 present the relations between the mentioned parameters. As seen by the figures, S_1^{max} is a bi-linear function of P and d:

$$S_1^{max} = S_1^{max}(P, d)$$

Equation 17

As shown by Figure 124, this means that S_1^{max} is a non-linear function of M:

$$S_1^{max} = S_1^{max}(M)$$

Equation 18

Table 6 - Stress results for the downward loading scenario parametric study (moment of force).

S_1^{max} [MPa]		*P* [N]										
		2500	3000	3500	4000	4500	5000	5500	6000	6500	7000	7500
	8	138.7	166.4	194.1	221.8	249.4	277.1	304.7	332.4	360	387.6	415.2
	12.3	148.8	178.5	208.2	237.9	267.6	297.3	326.9	356.6	386.2	415.8	445.4
	16.6	157.8	189.3	220.8	252.3	283.8	315.3	346.8	378.3	409.7	441.2	472.6
	20.9	165.9	199.1	232.3	265.4	298.6	331.8	364.9	398	431.1	464.3	497.4
	25.2	173.5	208.2	242.9	277.6	312.3	347	381.7	416.4	451.1	485.7	520.4
d [mm]	29.5	180.5	216.6	252.8	289	325.1	361.3	397.5	433.7	469.9	506.1	542.4
	33.8	187.3	224.9	262.5	300.2	337.9	375.6	413.3	451.1	488.8	526.6	564.5
	38.1	194.3	233.3	272.3	311.5	350.6	389.8	429.1	468.3	507.7	547	586.4
	42.4	201.2	241.7	282.2	322.8	363.5	404.3	445.1	485.9	526.8	567.8	608.8
	46.7	208.4	250.4	292.5	334.7	376.9	419.3	461.7	504.2	546.8	589.5	632.2
	51	216	259.6	303.3	347.1	391.1	435.2	479.3	523.6	568	612.4	657
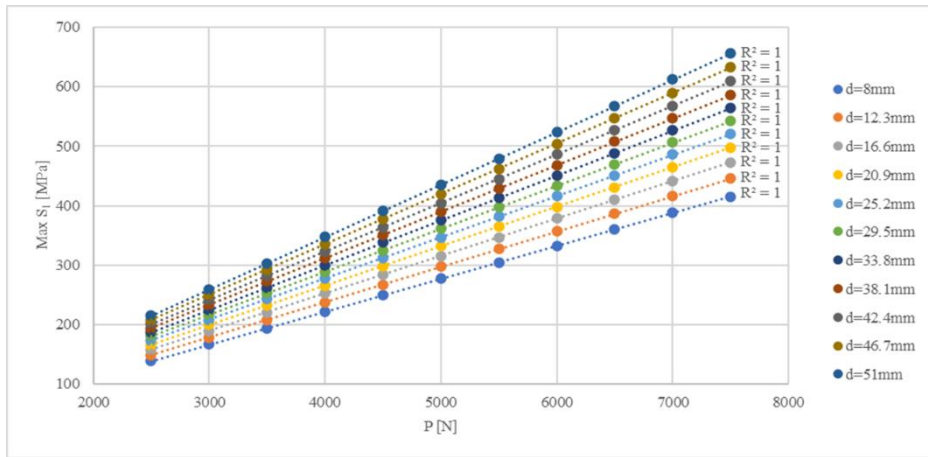
Figure 122 - S_1^{max} vs. P (d series, downward loading scenario).
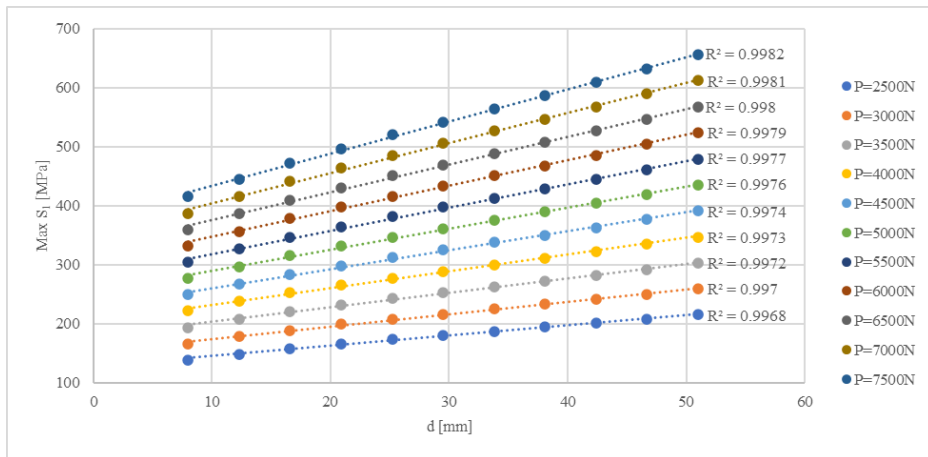
Figure 123 - S_1^{max} vs. d (P series, downward loading scenario).
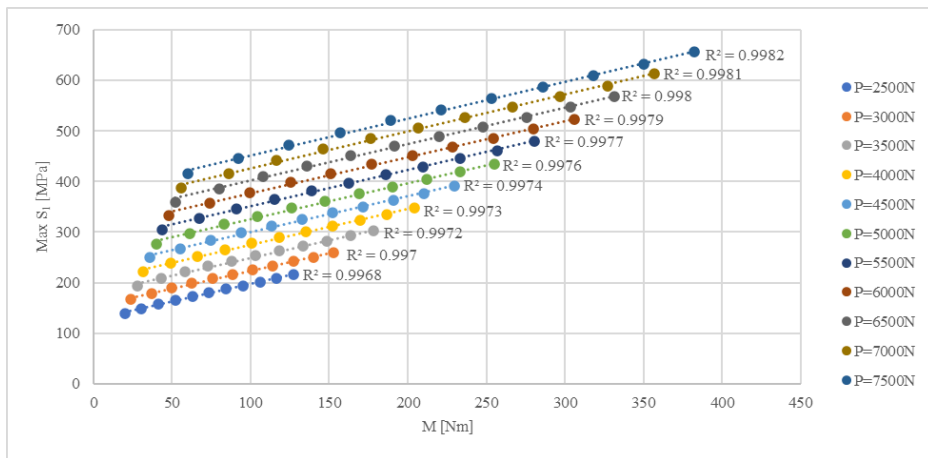
Figure 124 - S_1^{max} vs. M (P series, downward loading scenario).

Each one of the linear polynomials presented in Figure 124 can be written as:

$$S_1^{max} = a(P) \cdot M + b(P)$$

<div align="right">**Equation 19**</div>

where the coefficients a and b can be obtained through linear regression:

<div align="center">
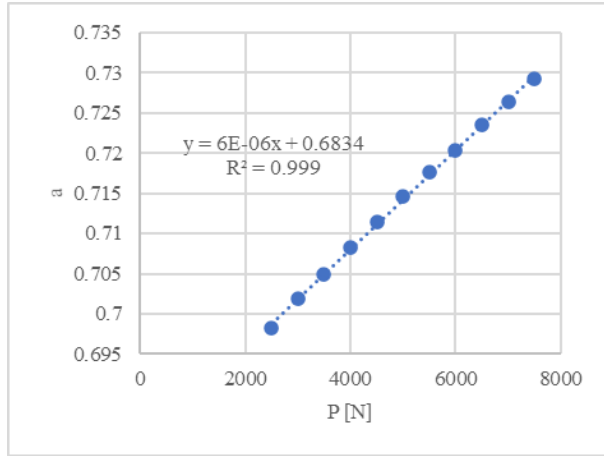
**Figure 125 - Linear regression to obtain coefficient a
(downward loading scenario).**

</div>

<div align="center">
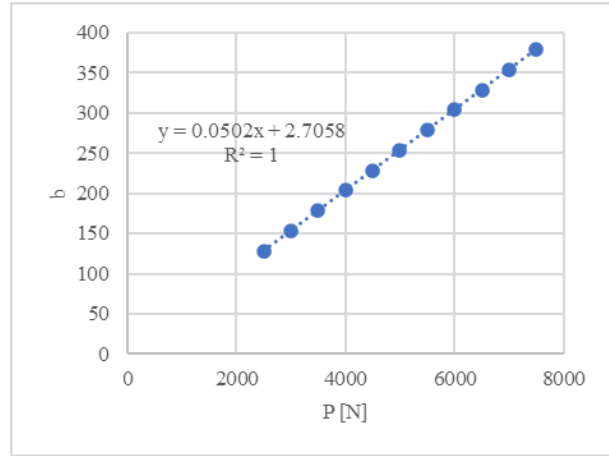
**Figure 126 - Linear regression to obtain coefficient b
(downward loading scenario).**

</div>

Meaning that the coefficients a and b are linear polynomials:

$$a = k_1 \cdot P + k_2$$

<div align="right">**Equation 20**</div>

$$b = k_3 \cdot P + k_4$$

<div align="right">**Equation 21**</div>

whose coefficients are presented in Table 7.

<div align="center">

Table 7 - Results for k_1, k_2, k_3, and k_4 coefficients (downward loading scenario).

</div>

k_1	k_2	k_3	k_4
6.17×10^{-6}	0.6834	0.0502	2.7058

In conclusion, S_1^{max} can be obtained through Equation 19, where a and b are obtained through Equation 20 and Equation 21, respectively, using the values in Table 7. Using Equation 19, a maximum relative difference of 2.5% is achieved when comparing to the results obtained directly from Abaqus® (Table 6).

6.1.2. Upward Loading Scenario

Table 8 presents the results extracted from the mentioned base model. Based on the presented table, Figure 127 and Figure 128 present the relations between the mentioned parameters. As seen by the figures, S_1^{max} varies linearly in P and logarithmically in d (Equation 17). As shown by Figure 129, this means that S_1^{max} is a non-linear function of M (Equation 18).

Table 8 - Stress results for the upward loading scenario parametric study (moment of force).

S_1^{max} [MPa]		P [N]										
		12500	13000	13500	14000	14500	15000	15500	16000	16500	17000	17500
d [mm]	8	354.2	368.6	383	397.5	412	426.5	441	455.6	470.2	484.8	499.4
	12.3	454.3	472.7	491.1	509.6	528.1	546.5	565	583.6	602.1	620.7	639.2
	16.6	527.4	548.7	570	591.3	612.7	634	655.3	676.7	698	719.4	740.8
	20.9	584.3	607.8	631.3	654.7	678.2	701.7	725.2	748.6	772.1	795.6	819.1
	25.2	630.7	655.9	681.1	706.2	731.4	756.6	781.7	806.8	832	857.1	882.2
	29.5	669.9	696.5	723.1	749.6	776.2	802.7	829.2	855.6	882	908.4	934.8
	33.8	704.1	731.8	759.6	787.3	814.9	842.5	870.1	897.6	925.1	952.5	979.9
	38.1	734.6	763.4	792.1	820.7	849.3	877.8	906.3	934.6	963	991.2	1019
	42.4	762.7	792.3	821.8	851.2	880.6	909.8	939	968.1	997	1026	1055
	46.7	789.3	819.6	849.8	879.9	909.9	939.8	969.6	999.2	1029	1058	1087
	51	816.7	847.6	878.4	909	939.5	969.8	999.9	1030	1060	1090	1119
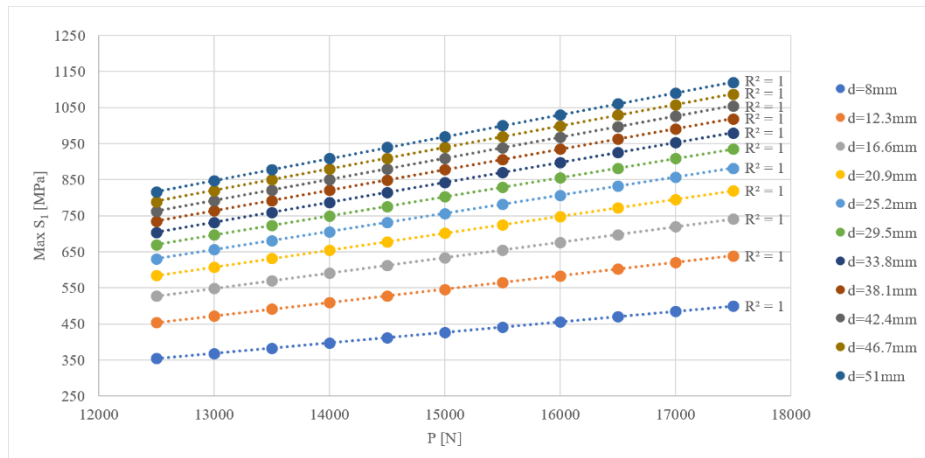
Figure 127 - S_1^{max} vs. P (d series, upward loading scenario)
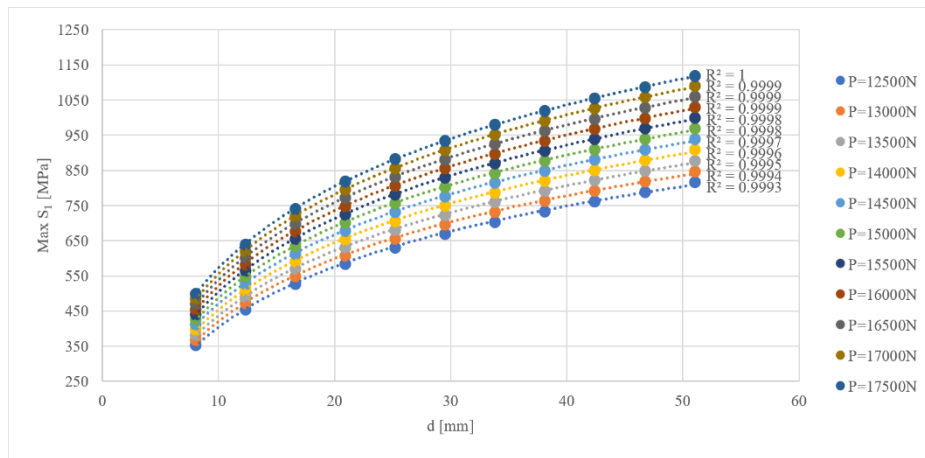
Figure 128 - S_1^{max} vs. d (P series, upward loading scenario).
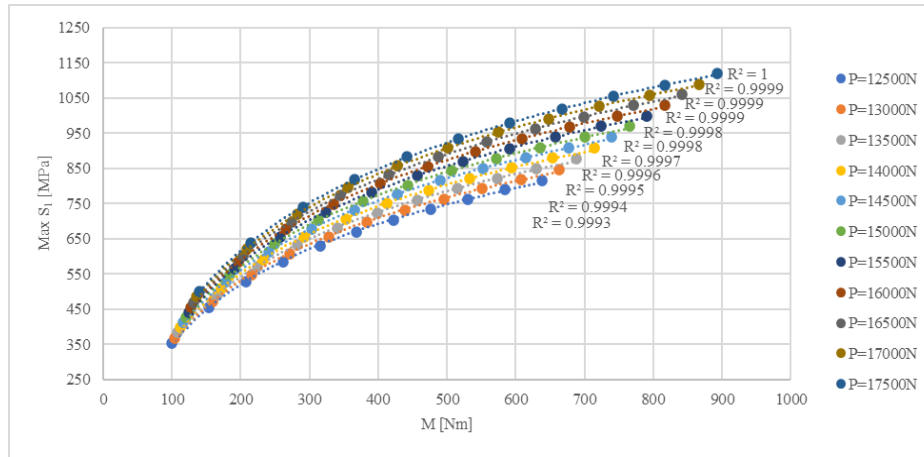
Figure 129 - S_1^{max} vs. M (P series, upward loading scenario).

Each one of the logarithmic functions presented in Figure 129 can be written as:

$$S_1^{max} = a(P) \cdot \ln(M) + b(P)$$

<div align="right">**Equation 22**</div>

where the coefficients a and b can be obtained through linear regression:
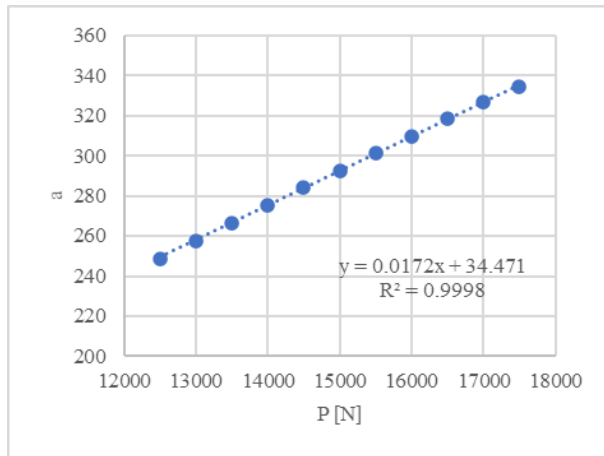
Figure 130 - Linear regression to obtain coefficient a (upward loading scenario).
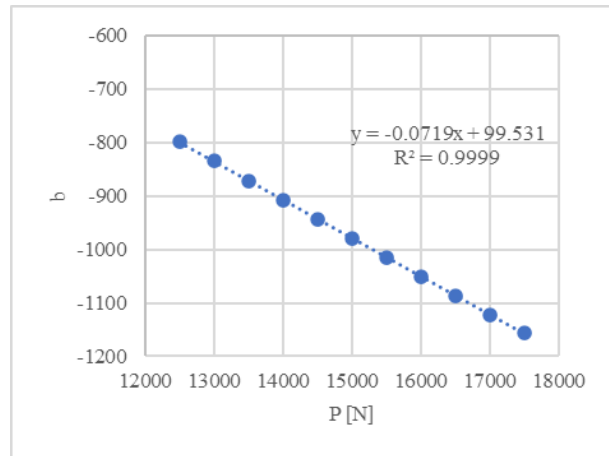
Figure 131 - Linear regression to obtain coefficient b (upward loading scenario).

Meaning that the coefficients a and b are linear polynomials (Equation 20 and Equation 21), whose coefficients are presented in Table 9.

Table 9 - Results for k_1, k_2, k_3, and k_4 coefficients (upward loading scenario).

k_1	k_2	k_3	k_4
0.0172	34.471	-0.0719	99.531

In conclusion, S_1^{max} can be obtained through Equation 22, where a and b are obtained through Equation 20 and Equation 21, respectively, using the values in Table 9. Using Equation 22, a maximum relative difference of 1.5% is achieved when comparing to the results obtained directly from Abaqus® (Table 8).

6.2.   Rail's Length

The next parameter to be analyzed was the rail's length in between holes, L (Figure 23). While varying this parameter, the presented base model was used to extract the maximum value of the maximum principal stresses, S_1^{max} (located in the web-flange corner, where cracking occurred during experimental fatigue testing). Two loading scenarios were analyzed, an upward and a downward loading scenario (Figure 121), where the previous parameters were kept constant:

Table 10 - Constant parameters for the rail's length parametric study.

P [N]	d [mm]
5000	29.5 (middle of the flange)

For plotting purposes, a reference simulation was considered, where $L_{ref} = 880$ mm, which corresponds to the experimental test conditions.

6.2.1. Downward Loading Scenario

Table 11 presents the results extracted from the mentioned base model. Figure 132 shows the plot of the mentioned results.

Table 11 - Stress results for the downward loading scenario parametric study (rail's length).

| L [mm]	S_1^{max} [MPa]	L/L_{ref}	$S_1^{max}/S_{1,ref}^{max}$
352	383.8	0.400	1.0197
418	381.7	0.475	1.0141
484	380.8	0.550	1.0117
550	379.5	0.625	1.0082
616	378.3	0.700	1.0050
682	377.2	0.775	1.0021
748	376.7	0.850	1.0008
814	376.4	0.925	1.0000
880	**376.4**	**1.000**	**1.0000**
946	376.5	1.075	1.0003
1,012	376.7	1.150	1.0008
1,078	376.9	1.225	1.0013
1,144	377.1	1.300	1.0019
1,210	377.2	1.375	1.0021
1,276	377.4	1.450	1.0027
1,342	377.5	1.525	1.0029
1,408	377.6	1.600	1.0032
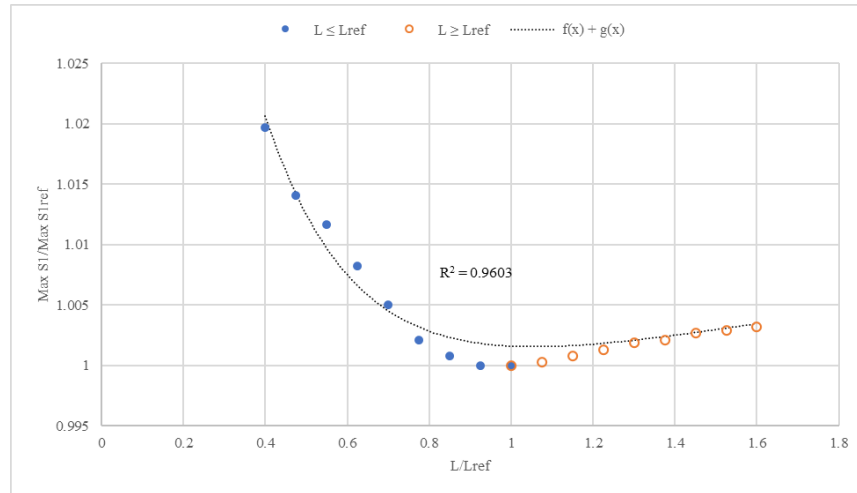
Figure 132 - Adimensional stress vs. adimensional length (downward loading scenario).

As shown by Figure 132, the obtained data can be approximated ($R^2 = 0.9603$) by the addition of two functions: the first relative to the blue points ($L \leq L_{ref}$), an exponential function, g; the second relative to the orange points ($L \geq L_{ref}$), a linear function, f:

$$f(x) = a_f \cdot x + b_f$$ **Equation 23**

$$g(x) = a_g \cdot e^{b_g \cdot x}$$ **Equation 24**

where the coefficients a_f, b_f, a_g, and b_g were obtained through curve fitting (Table 12).

Table 12 - Curve fitting results for the a_f, b_f, a_g, and b_g coefficients (downward loading scenario).

a_f	b_f	a_g	b_g
0.0056	0.9944	0.1456	-4.5059

This means that using the reference simulation of $L_{ref} = 880$ mm, a rail with "infinite length" can be considered, i.e., the stresses are very little affected by increasing the rail's length (varying linearly due to the global deflection of the rail), however, the stresses are more sensitive to the decrease in the rail's length, increasing exponentially.

6.2.2. Upward Loading Scenario

Table 13 presents the results extracted from the mentioned base model. Figure 133 shows the plot of the mentioned results. As shown by the figure, the obtained data can be approximated ($R^2 = 0.9915$) by the addition of two functions: the first relative to the blue points ($L \leq L_{ref}$), an exponential function, g (Equation 24); the second relative to the orange points ($L \geq L_{ref}$), a linear function, f (Equation 23). Where the coefficients a_f, b_f, a_g, and b_g were obtained through curve fitting (Table 14).

As before, this means that using the reference simulation of $L_{ref} = 880$ mm, a rail with "infinite length" can be considered, i.e., the stresses are very little affected by increasing the rail's length (varying linearly due to the global deflection of the rail), however, the stresses are more sensitive to the decrease in the rail's length, increasing exponentially.

Table 13 - Stress results for the upward loading scenario parametric study (rail's length).

L [mm]	S_1^{max} [MPa]	L/L_{ref}	$S_1^{max}/S_{1,ref}^{max}$
352	286.5	0.400	1.0280
418	284.8	0.475	1.0219
484	283.9	0.550	1.0187
550	282.7	0.625	1.0144
616	281.5	0.700	1.0100
682	280.5	0.775	1.0065
748	279.7	0.850	1.0036
814	279.1	0.925	1.0014
880	**278.7**	**1.000**	**1.0000**
946	278.4	1.075	0.9989
1,012	278.1	1.150	0.9978
1,078	277.8	1.225	0.9968
1,144	277.6	1.300	0.9961
1,210	277.3	1.375	0.9950
1,276	277.0	1.450	0.9939
1,342	276.6	1.525	0.9925
1,408	276.3	1.600	0.9914
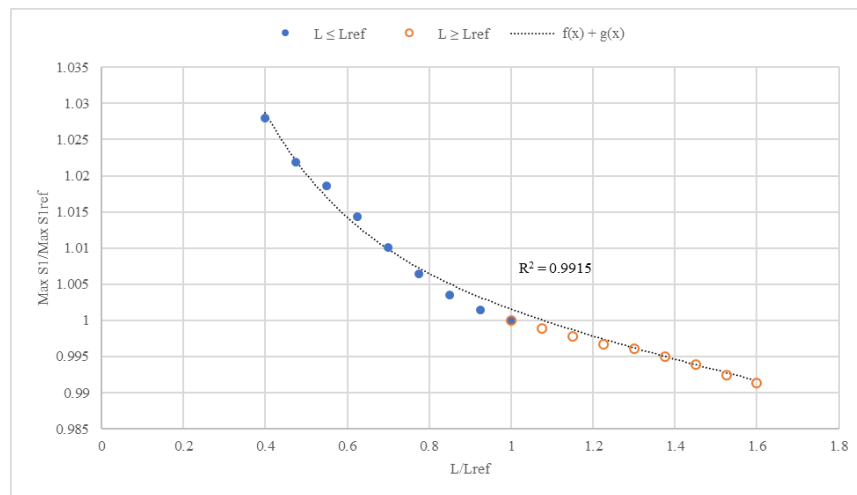
Figure 133 - Adimensional stress vs. adimensional length (upward loading scenario).

Table 14 - Curve fitting results for the a_f, b_f, a_g, and b_g coefficients (upward loading scenario).

a_f	b_f	a_g	b_g
-0.0141	1.0142	0.1132	-4.3068

6.3. Rail's Thickness and Web-Flange Corner Radius

The next parameters subjected to this study were the rail's thickness, t, and the rail's web-flange corner radius, R. While varying these parameters, the presented base model was used to extract the maximum value of the maximum principal stresses, S_1^{max} (located in the web-flange corner, where cracking occurred during experimental fatigue testing). The previous parameters were kept constant (Table 15).

Table 16 presents the results extracted from the presented base model. Figure 134 and Figure 135 show the plots of the mentioned results. As seen by the figures, S_1^{max} varies linearly in R, and non-linearly (power curve) in t:

$$S_1^{max} = S_1^{max}(R, t)$$

<div align="right">**Equation 25**</div>

As shown by Figure 136, this means that S_1^{max} varies non-linearly in the adimensional parameter R/t:

$$S_1^{max} = S_1^{max}(R/t)$$

<div align="right">**Equation 26**</div>

<div align="center">**Table 15 - Constant parameters for the rail's thickness and web-flange corner radius parametric study.**</div>

P [N]	d [mm]	L [mm]
5000	29.5 (middle of the flange)	880

<div align="center">**Table 16 - Stress results for the parametric study (rail's thickness and web-flange corner radius).**</div>

S_1^{max} [MPa]		t [mm]				
		1.5	2.5	3.5	4.5	5.5
R [mm]	6	1526	707.7	406.4	266.4	224.6
	7	1434	675.3	390.3	256.9	203.6
	8	1353	647.5	**376.4**	248.5	178.9
	9	1279	622.1	364.5	242.4	173.9
	10	1212	598.6	353.5	236	169.6
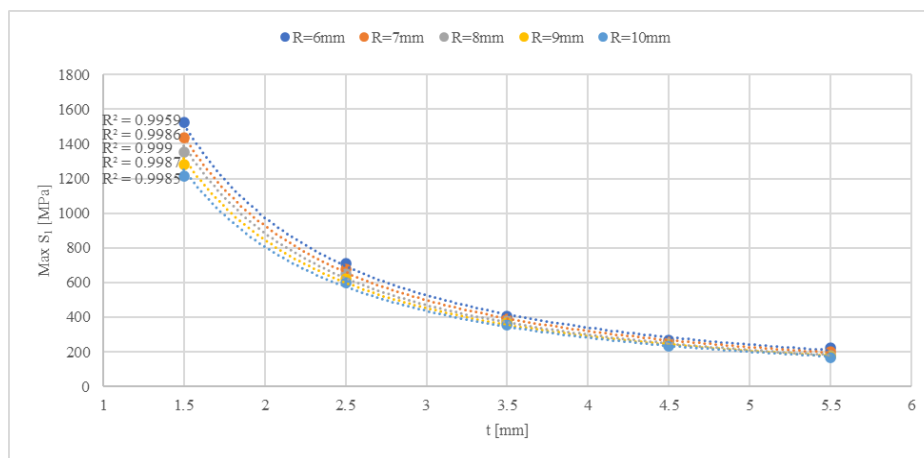
<div align="center">**Figure 134 - S_1^{max} vs. t (R series).**</div>
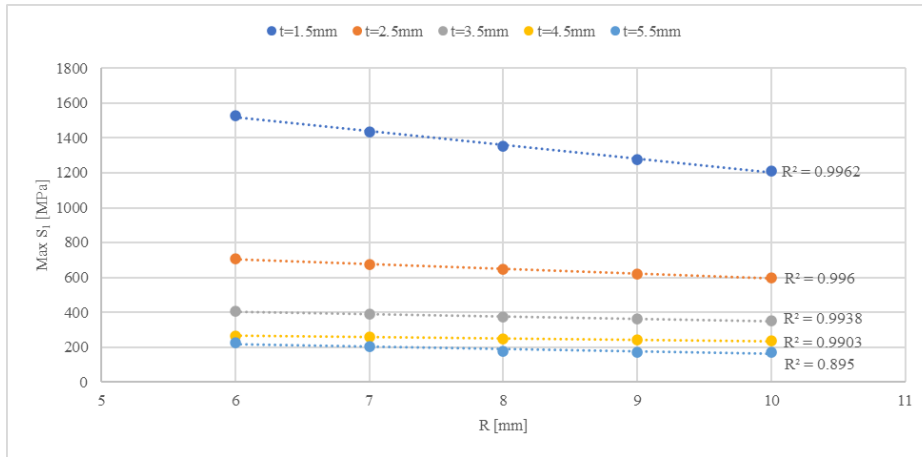
Figure 135 - S_1^{max} vs. R (t series)
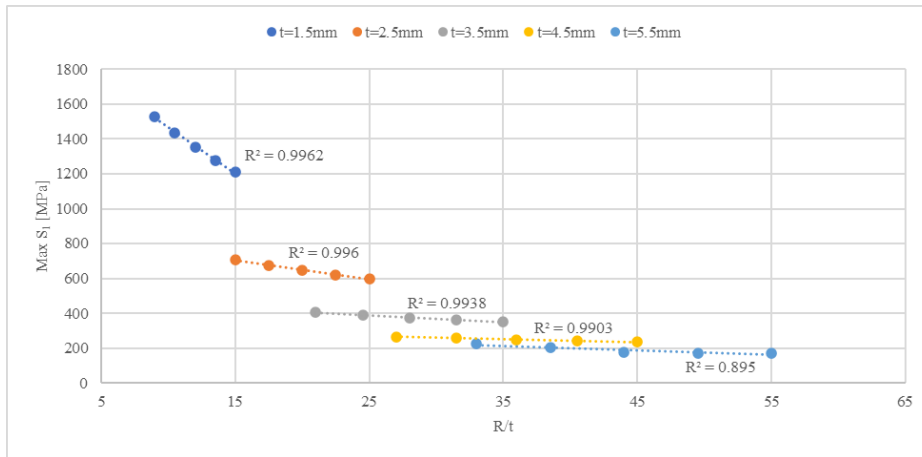
Figure 136 - S_1^{max} vs. R/t (t series).

Each one of the linear polynomials shown in Figure 136 can be written as:

$$S_1^{max} = a(t) \cdot \frac{R}{t} + b(t)$$

<div align="right">**Equation 27**</div>

where the coefficients a and b can be obtained through the following quadratic regression:
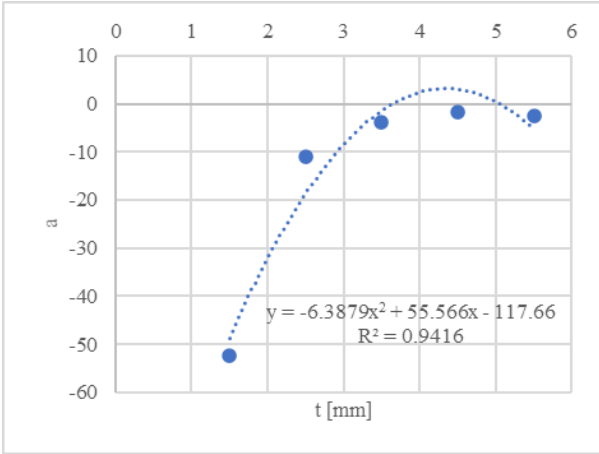
Figure 137 - Quadratic regression to obtain coefficient a.
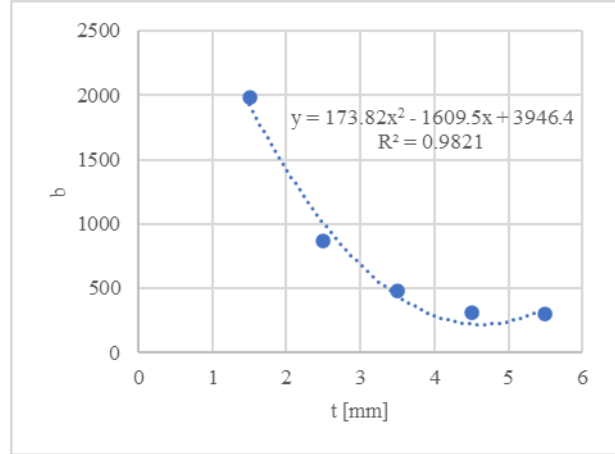
Figure 138 - Quadratic regression to obtain coefficient b.

Meaning that the coefficients a and b can be approximated through quadratic polynomials:

$$a = k_1 \cdot t^2 + k_2 \cdot t + k_3$$ **Equation 28**

$$b = k_4 \cdot t^2 + k_5 \cdot t + k_6$$ **Equation 29**

whose coefficients are presented in Table 17.

Table 17 - Results for k_1, k_2, k_3, k_4, k_5, and k_6 coefficients (quadratic regression).

k_1	k_2	k_3	k_4	k_5	k_6
-6.3879	55.566	-117.66	173.82	-1609.5	3946.4

In conclusion, S_1^{max} can be obtained through Equation 27, where a and b are obtained through Equation 28 and Equation 29, respectively, using the values in Table 17. However, using Equation 27, an average relative difference of 35% is achieved when comparing to the results obtained directly from Abaqus® (Table 16), which is unsatisfactory.

To remedy the above problem, a different approach was also tested. Up to now, S_1^{max} was considered as a function of a single independent adimensional variable, R/t (Equation 26). This idea is now replaced by considering S_1^{max} as a function of two independent variables, R and t (Equation 25).

MATLAB® was then used to surface fit the numerical data from Abaqus® using the following surface fit model, which is linear in R and cubic in t (Figure 139):

$$S_1^{max} = p_{00} + p_{10} \cdot R + p_{01} \cdot t + p_{11} \cdot R \cdot t + p_{02} \cdot t^2 + p_{12} \cdot R \cdot t^2 + p_{03} \cdot t^3$$ **Equation 30**

whose coefficients are presented in Table 18.

Table 18 - Coefficients used for surface fitting.

p_{00}	p_{10}	p_{01}	p_{11}	p_{02}	p_{12}	p_{03}
4902	-170.4	-2639	76.6	497.8	-8.825	-30.86
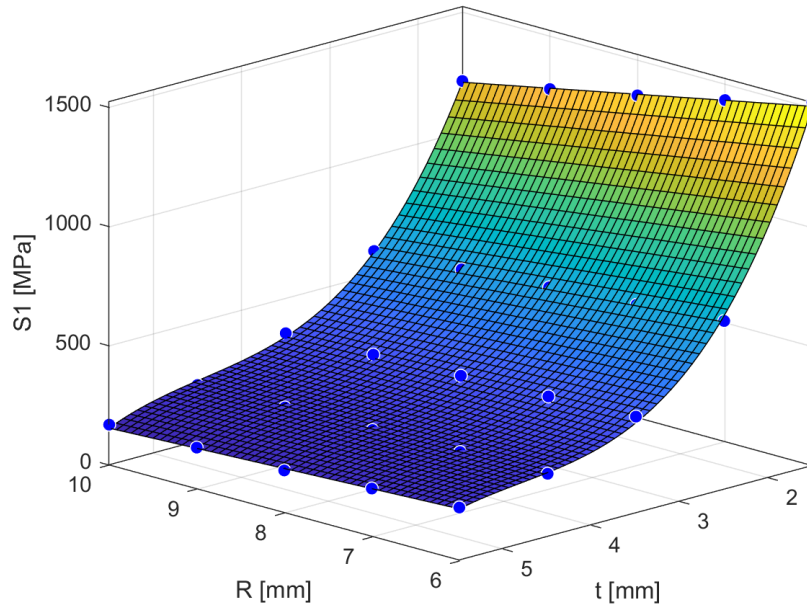
Figure 139 - $S_1^{max}(R, t)$ surface fitting.

Using Equation 30 with the coefficients from Table 18, a maximum relative difference of 8.6% is achieved (average relative difference of 3.2%) when comparing to the results obtained directly from Abaqus®.

Note that using this surface fitting approach for the previous presented study of the moment of force (section 6.1.), higher relative differences are obtained when comparing to the results from Abaqus® (when using a bi-linear surface model for surface fitting). So, this newer approach is not always the best nor the worst, but it always has the disadvantage of requiring longer polynomials (Equation 27 vs. Equation 30).

CHAPTER 7:   FATIGUE ANALYSIS OF THE Z-RAIL

In this chapter, the fatigue analysis conducted on the Z-rail is presented. The objective of this analysis is to obtain S-N fatigue design curves which can be used in the design of rack structures for shuttles. As stated before, current design codes, e.g. Eurocode 3, do not address thin, cold roll-formed structural elements. As presented before, these elements have internal residual stresses left over from their fabrication process. These internal residual stresses may play a significant role in the fatigue/structural performance of the Z-rail, which is another reason for the conducted fatigue analysis.

This chapter is divided into three sections: the first two sections present S-N fatigue design curves for the Z-rail without considering its internal residual stresses for the stress ranges calculations; the third section presents a Coffin-Manson fatigue life prediction for the Z-rail (considering its internal residual stresses), which is then compared to the obtained experimental results.

First, before presenting the fatigue analysis on the Z-rail, a note on its internal residual stresses. Based on Chapter 5, and referencing Figure 94, Figure 140 presents the Z-rail's tangential residual stresses on the web-flange corner's inner and outer surfaces (also known as R8 corner). As shown by this figure, residual stresses in the inner surface of the web-flange corner are tensile stresses, while at the outer surface they are compressive stresses (or close to zero). During fatigue cycling, it is expected that the mean stresses are influenced by the residual stresses. On effect, during the downward loading scenario (Figure 32), the mean stress will increase due to the tensile residual stresses at the inner surface, which is the crack initiation site; for the upward loading scenario (Figure 34), the mean stress will be reduced due to the expected compressive residual stresses at the outer surface. It is expected that this mean stress difference impacts differently on fatigue damage, i.e., it is expected different fatigue behaviors for the Z-rail when subjected to either a downward or an upward loading scenario.
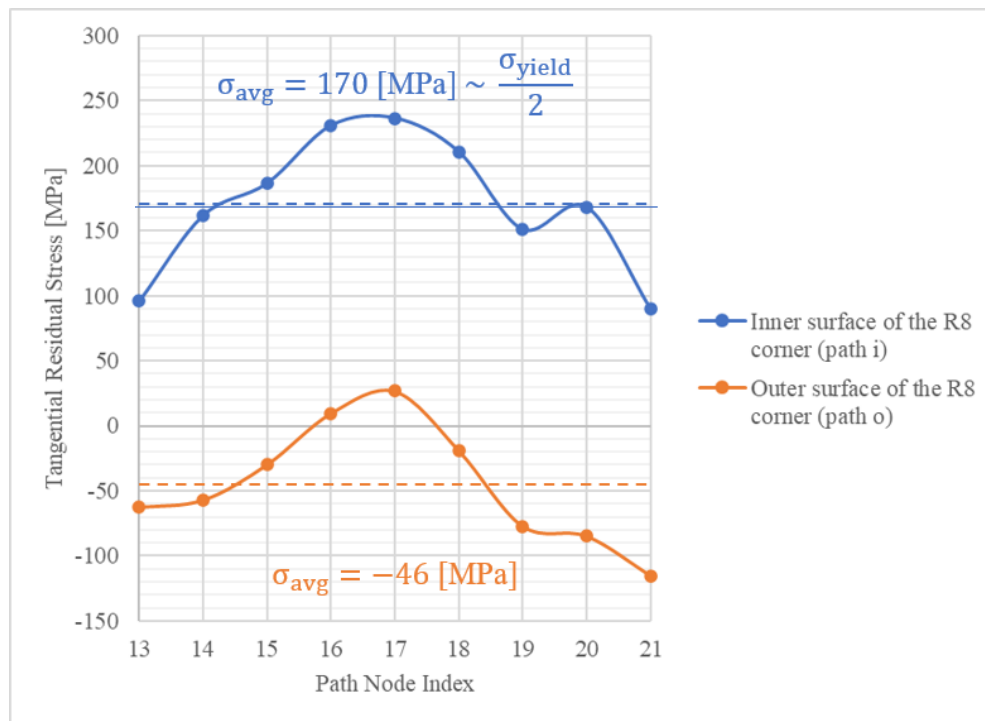

Figure 140 - Tangential residual stresses on the Z-rail's R8 corner.

7.1.   S-N Fatigue Design Curve Based on Elastic FEA

The first S-N fatigue design curve was proposed based on the following:

- Fatigue life, in terms of load cycles, was obtained through experimental testing (Chapter 4);
- Stress ranges were obtained through numerical simulations in Abaqus® (linear-elastic material).

In the mentioned numerical simulations, the experimental setup is replicated as closely as possible. The simulations consist in a 3D FEA model with the following characteristics:

- The rail has a total length of 880 mm (distance between bolt holes, Figure 23);
- The model considers the symmetry in the Z-rail's length axis (only half of the Z-rail's total length is modeled);
- The rail's S355MC material is considered elastic (elastic properties presented in Chapter 3). The rail's section is also considered solid and homogeneous;
- The numerical model includes hard normal contact and frictionless tangential contact (between the load actuator, or the load actuator's plate, and the rail's flange; surface-to-surface contact discretization, direct, or Lagrange multipliers method, contact enforcement);
- The Z-rail (and also for the upward loading scenario, the load actuator's plate and the mid-span cover plate) is discretized by the C3D8 element, a continuum hexahedral element with 8 nodes and 8 integration points (full integration);
- The model considers non-linear geometry effects (NLGEOM);
- The Z-rail's web is fixed on both ends with a mid-span support. The load actuator (considered an analytical, non-deformable, rigid part) is placed either on top or on the bottom of the rail's flange (downward and upward loading scenarios). As mentioned before, for the upward loading scenario, an additional steel plate is placed in between the load actuator and the rail's flange, as well as a steel cover to clamp the rail's web at the mid-span support. The actuator is free to rotate along the rail's length axis;
- Finally, the actuator is displaced until half of the intended load is achieved, due to symmetry. Then, the maximum value of the maximum principal stresses is extracted from the web-flange corner (where cracking occurred during experimental testing) for the S-N curve's stress ranges.

Figure 141 to Figure 144 show the mentioned FEA models to obtain the stress ranges for building an S-N curve. Appendix D presents the results for all the carried-out simulations. Table 19 presents the S-N data used to build the S-N curve. On this table's "Loading Scenario" column, the letter D stands for downward loading scenario, and the letter U stands for upward loading scenario. Based on Table 19, Figure 145 to Figure 147 present the obtained S-N curves. Note that the ASTM E739-91 standard was used to obtain the mean S-N curve, the standard deviation, and the coefficient of determination, as well as to establish confidence bands.
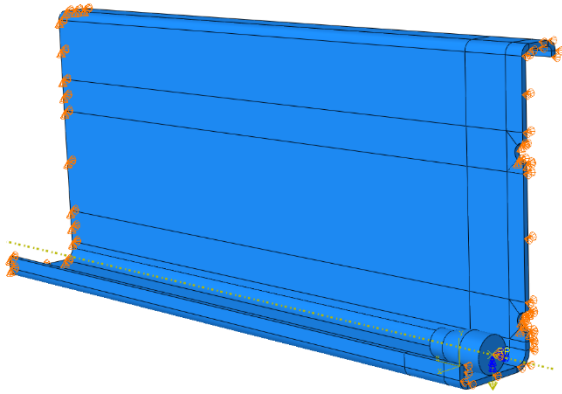
Figure 141 - FEA model for downward loading scenario stress ranges determination (geometry and boundary conditions).
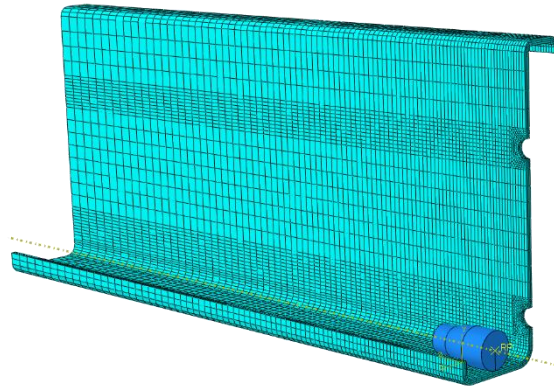
Figure 142 - FEA model for downward loading scenario stress ranges determination (mesh).
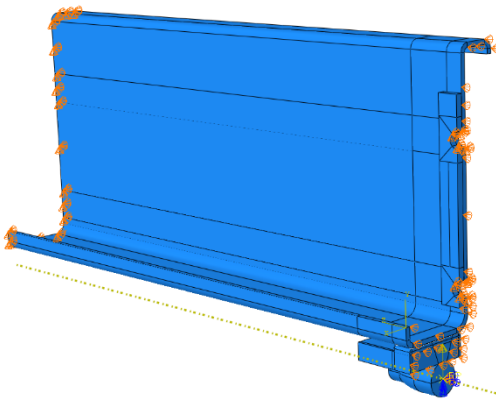
Figure 143 - FEA model for upward loading scenario stress ranges determination (geometry and boundary conditions).
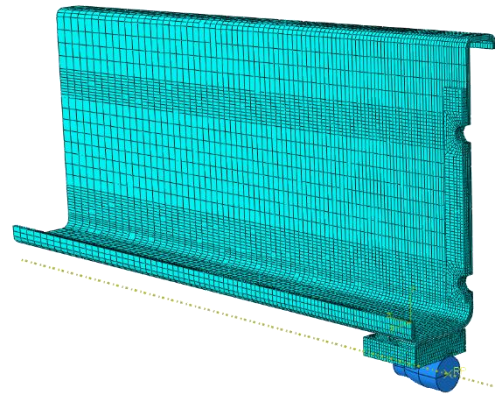
Figure 144 - FEA model for upward loading scenario stress ranges determination (mesh).

Table 19 - S-N data: experimental lifetime; stress ranges obtained through FEA (based on maximum principal stresses).

Loading Scenario	Specimen	Max Load [N]	Min Load [N]	Max Stress [MPa]	Min Stress [MPa]	Stress Range [MPa]	Lifetime	Comments
D	7	5,000	500	415.8	41.50	374.30	325,000	Outlier
D	8	5,000	500	415.8	41.50	374.30	5,000,000	Run out
D	9	5,000	500	415.8	41.50	374.30	5,000,000	Run out
D	10	5,000	500	415.8	41.50	374.30	5,000,000	Run out
D	11	7,500	750	624.5	62.26	562.24	160,000	-
D	12	7,500	750	624.5	62.26	562.24	120,000	-
D	13	7,500	750	624.5	62.26	562.24	200,000	-
D	14	7,500	750	624.5	62.26	562.24	95,000	-
D	17	9,000	900	749.9	74.71	675.19	75,000	-
D	18	9,000	900	749.9	74.71	675.19	42,500	-
D	19	6,250	625	520.1	51.88	468.22	580,000	-
D	20	6,250	625	520.1	51.88	468.22	325,000	-
D	21	9,000	900	749.9	74.71	675.19	90,000	-
D	22	9,000	900	749.9	74.71	675.19	45,000	-

| D	23	6,250	625	520.1	51.88	468.22	220,000	-
D	24	6,250	625	520.1	51.88	468.22	120,000	-
D	49	5,500	550	457.5	45.65	411.85	550,000	-
D	50	5,500	550	457.5	45.65	411.85	800,000	-
U	31	9,000	900	399.1	41.90	357.20	5,000,000	Run out
U	32	9,000	900	399.1	41.90	357.20	5,000,000	Run out
U	33	17,500	1,750	746.6	81.06	665.54	45,000	-
U	34	17,500	1,750	746.6	81.06	665.54	62,000	-
U	35	17,500	1,750	746.6	81.06	665.54	22,000	-
U	36	17,500	1,750	746.6	81.06	665.54	64,000	-
U	37	15,000	1,500	646.3	69.59	576.71	200,000	-
U	38	15,000	1,500	646.3	69.59	576.71	255,000	-
U	39	12,500	1,250	544.4	58.07	486.33	850,000	-
U	40	12,500	1,250	544.4	58.07	486.33	700,000	-
U	41	15,000	1,500	646.3	69.59	576.71	180,000	-
U	42	15,000	1,500	646.3	69.59	576.71	240,000	-
U	43	12,500	1,250	544.4	58.07	486.33	550,000	-
U	44	12,500	1,250	544.4	58.07	486.33	645,000	-
U	45	10,000	1,000	440.8	46.53	394.27	550,000	-
U	46	10,000	1,000	440.8	46.53	394.27	650,000	-
U	47	10,000	1,000	440.8	46.53	394.27	700,000	-
U	48	10,000	1,000	440.8	46.53	394.27	900,000	-
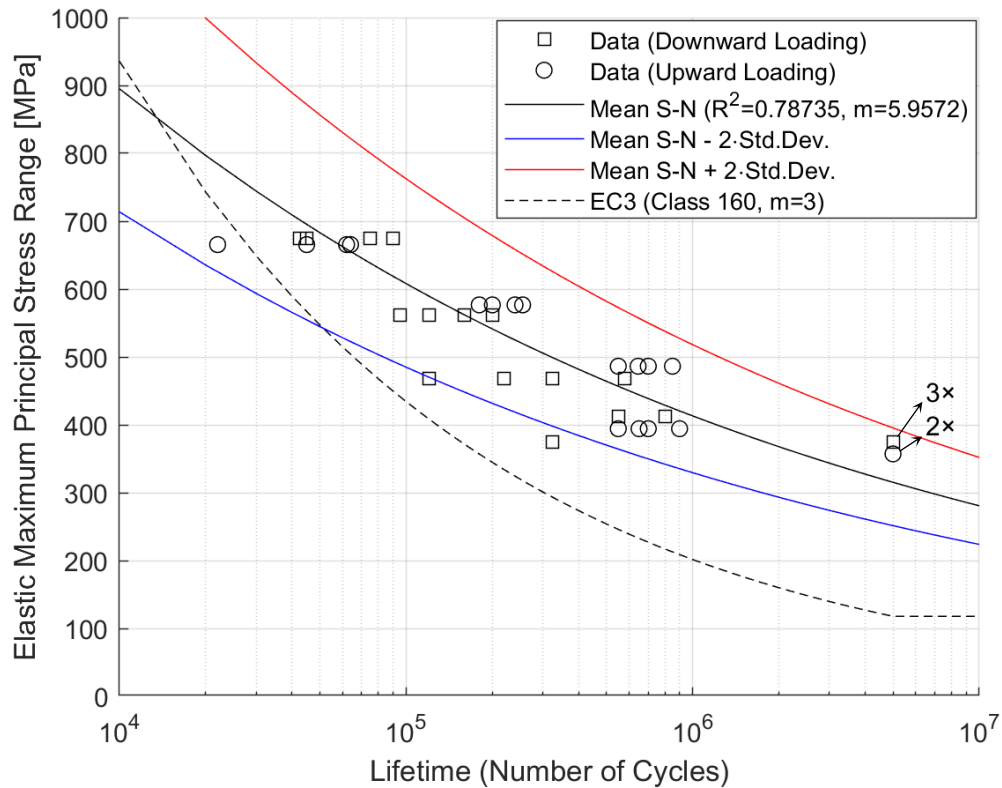
Figure 145 - S-N curve (experimental lifetime, stress ranges obtained through FEA).
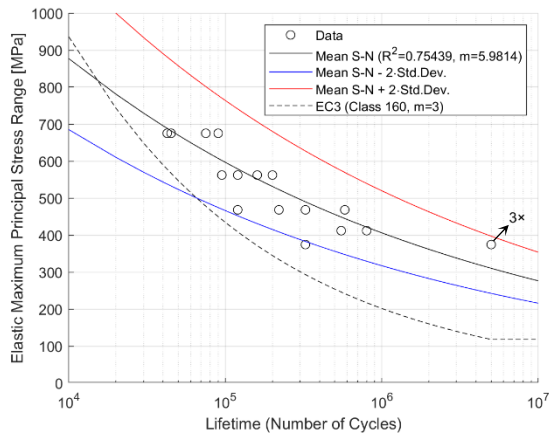
Figure 146 - Downward loading scenario S-N curve (experimental lifetime, stress ranges obtained through FEA).
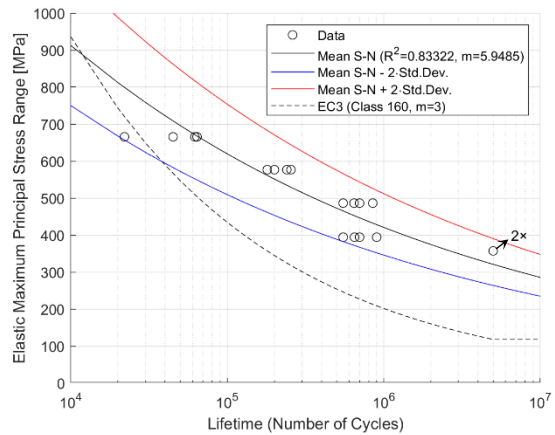

Figure 147 - Upward loading scenario S-N curve (experimental lifetime, stress ranges obtained through FEA).

As shown in Figure 145, the obtained data (except 1 point) fits on the safe-side of the Eurocode 3 class 160 MPa S-N curve, and in between the mean S-N curves with twice the standard deviation. The slope of the obtained fatigue strength curve is $m = 5.96$, which is higher than the reference values of the Eurocode 3 ($m = 3$ between 10^4 and 5×10^6 cycles). Finally, as shown in Figure 146 and Figure 147, there is no real distinction between an upward and a downward loading scenario, with both cases presenting similar fatigue strength curve slopes, as well as similar stress ranges.

7.2. S-N Fatigue Design Curve Based on the Z-Rail's Parametric Study

The second S-N fatigue design curve consisted in the following:

- Fatigue life, in terms of load cycles, was obtained through experimental testing (Chapter 4);
- Stress ranges were obtained through the use of Equation 19 (downward loading scenario) and Equation 22 (upward loading scenario), obtained during the Z-rail's parametric study (Chapter 6).

Based on the mentioned equations, Table 20 presents the S-N data for building the S-N curve. On this table's "Loading Scenario" column, the letter D stands for downward loading scenario, and the letter U stands for upward loading scenario. Based on Table 20, Figure 148 to Figure 150 present the obtained S-N curves. Note that the ASTM E739-91 standard was used again to obtain the mean S-N curve, the standard deviation, and the coefficient of determination, as well as to establish confidence bands.

Table 20 - S-N data: experimental lifetime; stress ranges obtained through analytical fitted equations.

Loading Scenario	Specimen	Max Load [N]	Min Load [N]	Max Stress [MPa]	Min Stress [MPa]	Stress Range [MPa]	Lifetime	Comments
D	7	5,000	500	359.06	37.931	321.13	325,000	Outlier
D	8	5,000	500	359.06	37.931	321.13	5,000,000	Run out
D	9	5,000	500	359.06	37.931	321.13	5,000,000	Run out
D	10	5,000	500	359.06	37.931	321.13	5,000,000	Run out
D	11	7,500	750	540.65	55.578	485.07	160,000	-
D	12	7,500	750	540.65	55.578	485.07	120,000	-
D	13	7,500	750	540.65	55.578	485.07	200,000	-
D	14	7,500	750	540.65	55.578	485.07	95,000	-

D	17	9,000	900	650.69	66.178	584.51	75,000	-
D	18	9,000	900	650.69	66.178	584.51	42,500	-
D	19	6,250	625	449.57	46.752	402.82	580,000	-
D	20	6,250	625	449.57	46.752	402.82	325,000	-
D	21	9,000	900	650.69	66.178	584.51	90,000	-
D	22	9,000	900	650.69	66.178	584.51	45,000	-
D	23	6,250	625	449.57	46.752	402.82	220,000	-
D	24	6,250	625	449.57	46.752	402.82	120,000	-
D	49	5,500	550	395.19	41.459	353.73	550,000	-
D	50	5,500	550	395.19	41.459	353.73	800,000	-
U	31	9,000	900	508.87	198.61	310.26	5,000,000	Run out
U	32	9,000	900	508.87	198.61	310.26	5,000,000	Run out
U	33	17,500	1,750	936.83	228.37	708.46	45,000	-
U	34	17,500	1,750	936.83	228.37	708.46	62,000	-
U	35	17,500	1,750	936.83	228.37	708.46	22,000	-
U	36	17,500	1,750	936.83	228.37	708.46	64,000	-
U	37	15,000	1,500	802.89	220.10	582.79	200,000	-
U	38	15,000	1,500	802.89	220.10	582.79	255,000	-
U	39	12,500	1,250	675.18	211.57	463.61	850,000	-
U	40	12,500	1,250	675.18	211.57	463.61	700,000	-
U	41	15,000	1,500	802.89	220.10	582.79	180,000	-
U	42	15,000	1,500	802.89	220.10	582.79	240,000	-
U	43	12,500	1,250	675.18	211.57	463.61	550,000	-
U	44	12,500	1,250	675.18	211.57	463.61	645,000	-
U	45	10,000	1,000	554.73	202.51	352.22	550,000	-
U	46	10,000	1,000	554.73	202.51	352.22	650,000	-
U	47	10,000	1,000	554.73	202.51	352.22	700,000	-
U	48	10,000	1,000	554.73	202.51	352.22	900,000	-

As shown in Figure 148, the obtained data (except 1 point) fits on the safe-side of the Eurocode 3 class 160 MPa S-N curve, and in between the mean S-N curves with twice the standard deviation. The slope of the obtained fatigue strength curve is $m = 4.66$, which is higher than the reference values of the Eurocode 3 ($m = 3$ between 10^4 and 5×10^6 cycles). As shown in Figure 149 and Figure 150, there is a slight difference between an upward and a downward loading scenario, where the downward loading scenario presents a higher slope and lower stress ranges, indicating that this loading scenario is the most damaging.

Finally, comparing Figure 148 to Figure 145, it is possible to see that both S-N curves are similar, even though the former S-N curve is based on the equations presented in Chapter 6, where the Z-rail's parametric study is based on very simple FEA models.
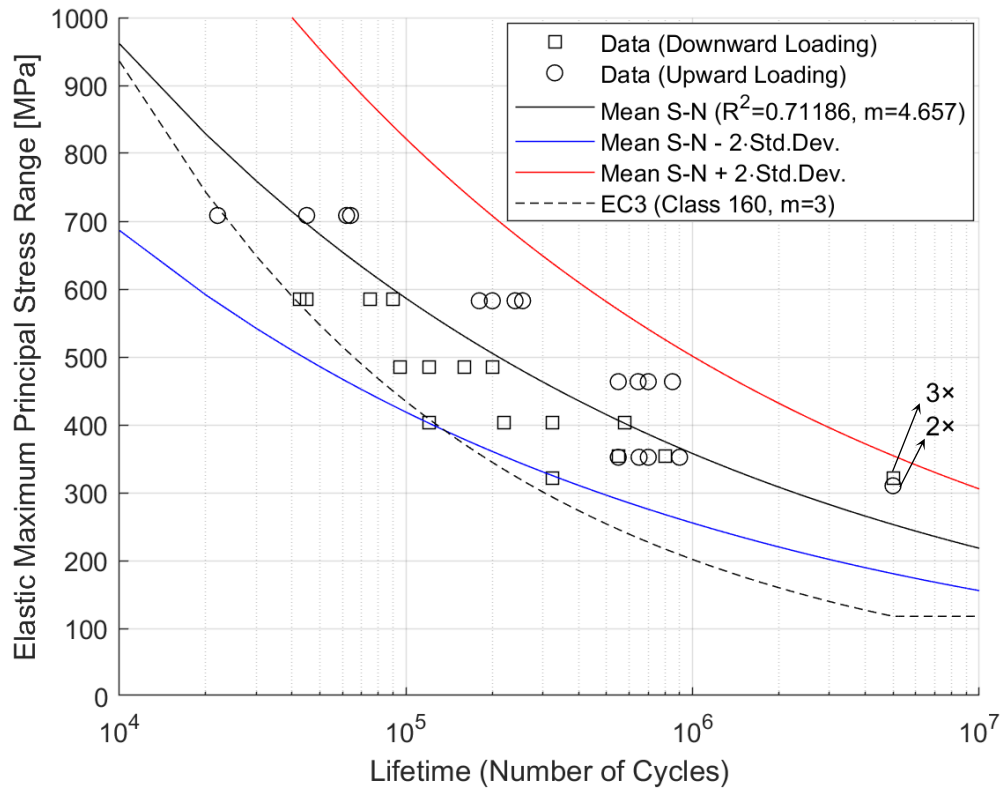
Figure 148 - S-N curve (experimental lifetime, stress ranges obtained through equations).
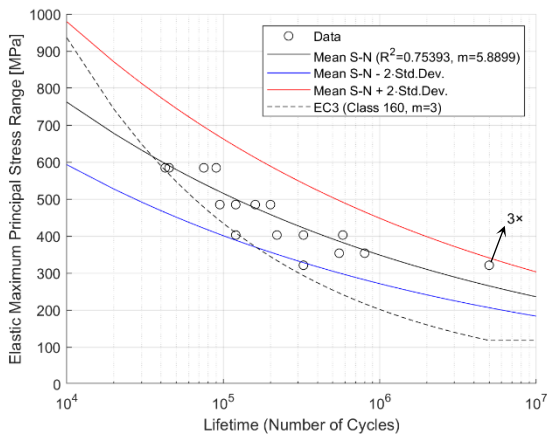

Figure 149 - Downward loading scenario S-N curve (experimental lifetime, stress ranges obtained through equations).
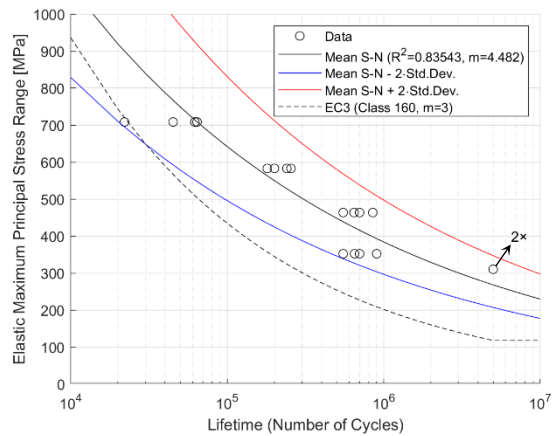
Figure 150 - Upward loading scenario S-N curve (experimental lifetime, stress ranges obtained through equations).

7.3.　Coffin-Manson Fatigue Life Prediction

In Marc®, after obtaining the Z-rail with internal residual stresses through the simulation of the cold roll-forming fabrication process using the base model from Chapter 5, additional load steps were created where the Z-rail is fixed on both ends and a point load is applied to the middle of the flange, at the mid-span of the rail. Figure 151 shows a downward loading scenario (9 kN load example), and Figure 152 shows an

upward loading scenario (9 kN load example). In these simulations, the manufacturing process and external structural loads are encompassed by a single model using elastoplastic FEA.
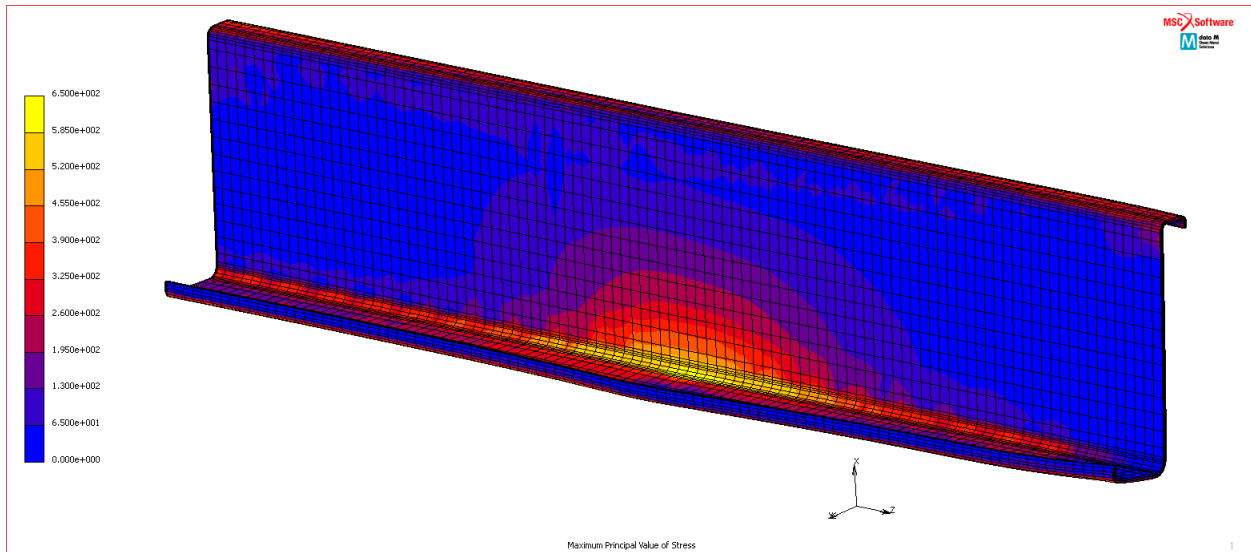

Figure 151 - Downward loading scenario point load with residual stresses superposition (maximum principal stress, example for 9 kN load).
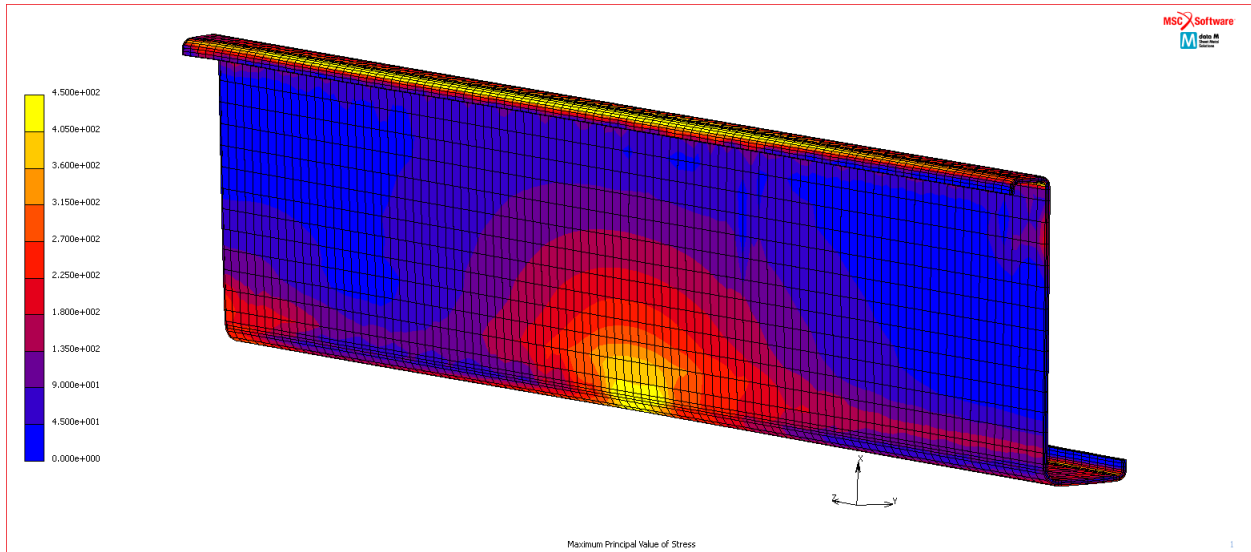

Figure 152 - Upward loading scenario point load with residual stresses superposition (maximum principal stress, example for 9 kN load).

The mentioned extra load steps are necessary to estimate the lifetime, in terms of load cycles, of the rail through the Coffin-Manson equation:

$$\frac{\Delta \varepsilon}{2} = \frac{\sigma_f' - \sigma_m}{E} \cdot (2N_f)^b + \varepsilon_f' \cdot (2N_f)^c \qquad \textbf{Equation 31}$$

Where:

- $\Delta\varepsilon = \varepsilon_{max} - \varepsilon_{min}$ is the strain range within the load cycle;
- $\sigma_m = 0.5 \cdot (\sigma_{max} + \sigma_{min})$ is the mean stress of the load cycle;
- N_f is the estimated lifetime in terms of load cycles;
- E is the Young's modulus of the material;
- σ'_f, ε'_f, b and c are empirically determined material constants, based on fatigue tests of smooth specimens.

Table 21 - Empirically determined material constants for the S355MC material (De Jesus, et al., 2012).

σ'_f [MPa]	ε'_f	b	c
952.2	0.7371	-0.089	-0.664

Using the material constants presented in Table 21, the Newton-Raphson method was employed to solve Equation 31, obtaining the Coffin-Manson lifetime predictions. Appendix E shows the used MATLAB® code. Table 22 presents the obtained results.

Table 22 - Results for the Coffin-Manson lifetime prediction

Loading Scenario	Specimen	Max Load [N]	Min Load [N]	Mean Stress [MPa]	Strain Range [mm/mm]	Experimental Lifetime	Coffin-Manson Lifetime
D	7	5,000	500	473.45	0.001430	325,000	910,246
D	8	5,000	500	473.45	0.001430	5,000,000	910,246
D	9	5,000	500	473.45	0.001430	5,000,000	910,246
D	10	5,000	500	473.45	0.001430	5,000,000	910,246
D	11	7,500	750	498.74	0.002729	160,000	28,738
D	12	7,500	750	498.74	0.002729	120,000	28,738
D	13	7,500	750	498.74	0.002729	200,000	28,738
D	14	7,500	750	498.74	0.002729	95,000	28,738
D	17	9,000	900	517.27	0.003596	75,000	11,970
D	18	9,000	900	517.27	0.003596	42,500	11,970
D	19	6,250	625	485.68	0.002060	580,000	91,327
D	20	6,250	625	485.68	0.002060	325,000	91,327
D	21	9,000	900	517.27	0.003596	90,000	11,970
D	22	9,000	900	517.27	0.003596	45,000	11,970
D	23	6,250	625	485.68	0.002060	220,000	91,327
D	24	6,250	625	485.68	0.002060	120,000	91,327
D	49	5,500	550	478.40	0.001679	550,000	284,686
D	50	5,500	550	478.40	0.001679	800,000	284,686
U	31	9,000	900	333.02	0.002123	5,000,000	287,366
U	32	9,000	900	333.02	0.002123	5,000,000	287,366
U	33	17,500	1,750	447.42	0.005564	45,000	4,825
U	34	17,500	1,750	447.42	0.005564	62,000	4,825
U	35	17,500	1,750	447.42	0.005564	22,000	4,825
U	36	17,500	1,750	447.42	0.005564	64,000	4,825
U	37	15,000	1,500	432.99	0.004332	200,000	9,233

U	38	15,000	1,500	432.99	0.004332	255,000	9,233
U	39	12,500	1,250	422.29	0.003043	850,000	27,892
U	40	12,500	1,250	422.29	0.003043	700,000	27,892
U	41	15,000	1,500	432.99	0.004332	180,000	9,233
U	42	15,000	1,500	432.99	0.004332	240,000	9,233
U	43	12,500	1,250	422.29	0.003043	550,000	27,892
U	44	12,500	1,250	422.29	0.003043	645,000	27,892
U	45	10,000	1,000	361.38	0.002358	550,000	119,499
U	46	10,000	1,000	361.38	0.002358	650,000	119,499
U	47	10,000	1,000	361.38	0.002358	700,000	119,499
U	48	10,000	1,000	361.38	0.002358	900,000	119,499

Figure 153 presents the results of Table 22. To have a good fatigue life prediction, all points in Figure 153 should fall in between a double-half band, which, unfortunately, does not happen. However, all points, except one, fall on the safe side of the plot. This point that falls on the unsafe side is the point marked as "outlier" in the S-N data.
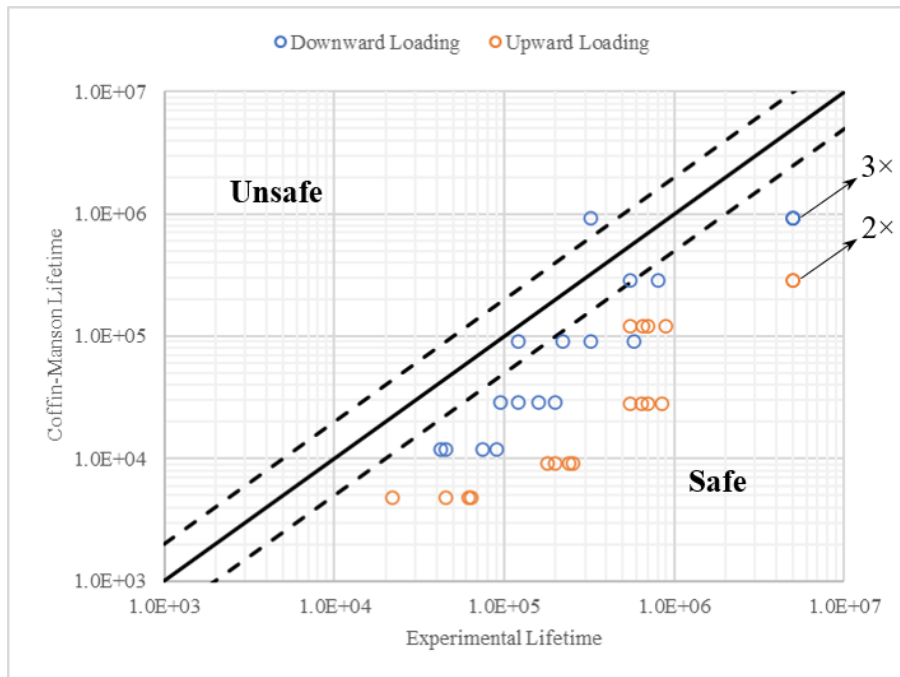
Figure 153 - Coffin-Manson vs. experimental lifetimes.

CHAPTER 8: CONCLUSIONS

In this day and age, rack structures prepared for automatic shuttles are vastly used in the logistics engineering field. These shuttles carry pallets loaded with various goods and products. Z-rails are commonly used as tracks for these shuttles to move through the rack structure. However, even though Z-rails (and other similar thin cold roll-formed structural elements) are commonly used today, design codes, like the Eurocode 3, do not yet take into consideration thin cold roll-formed structural elements, which contain internal residual stresses leftover from their fabrication process. The FASTCOLD project aims to provide a solution to this problem, whose aim (among others) is to define fatigue design curves for thin cold roll-formed structural elements, so that rack structures, and the warehouse where these reside, are safer working zones.

In order to provide insight on the fatigue behavior of the mentioned type of structural elements, one must first understand and analyze the cold roll-forming fabrication process. As stated, this fabrication process is quite complex, where the end product has an extensive history of residual stresses, which are due to transversal bending and shaping of the strip's cross section, and to the longitudinal coiling and uncoiling cycles of the raw material to be used in the forming process.

Modern day tools must also be employed to fully understand the impact of residual stresses on fatigue behavior. The famous Finite Element Method is, arguably, the best numerical tool to deal with complex engineering problems, giving the users the possibility to simulate real physical processes, like the roll-forming fabrication process. In this dissertation, the Finite Element Method was used to combine the manufacturing process of the Z-rail with the application of external structural loads. With the presented procedures, a FEA model that contains the Z-rail's plastic stress and strain history (which was obtained through the simulation of the cold roll-forming process) is used to simulate structural loading on the Z-rail, while also taking into account its internal residual stresses.

Finally, the important field of material fatigue comes into play, where standardized procedures are used in order to construct S-N fatigue design curves. For this, a completely new experimental fatigue testing setup was created at the Faculty of Engineering of the University of Porto in order to conduct full scale fatigue tests to obtain experimental fatigue life of rail specimens. As presented, the Finite Element Method was, yet again, employed to simulate (as closely as possible) the experimental fatigue testing setup, obtaining elastic stress ranges to construct the presented S-N curves. A local approach, the Coffin-Manson approach, was also included to compare theoretical fatigue life predictions with the obtained experimental data.

8.1. Chapter 1, 2, and 3

In Chapter 1, the background and scope of this dissertation is presented. In Chapter 2, a literature review is presented, where the reader has the opportunity to delve into the basic and fundamental concepts of the cold roll-forming fabrication process, the fatigue analysis, and the finite element method topics. The understanding of these three topics are crucial in order to follow along this dissertation.

In Chapter 3, the Z-rail, which is a case study for this whole dissertation, is presented. Its geometric properties are stated and the S355MC elastoplastic properties are defined for further use in FEA models.

8.2. Chapter 4

In Chapter 4, the complete process of creating and refining the experimental fatigue testing setup for full scale fatigue tests on Z-rail specimens is presented. This was an arduous and time-consuming task, but in the end, the setup is able to generate representative fatigue cracks on the Z-rail. Numerical simulations replicating the experimental fatigue testing setup were also conducted and presented to identify and resolve issues with the setup.

As referenced several times in this dissertation, two loading scenarios were repeatedly analyzed: a downward and an upward loading scenario. The experimental fatigue testing setup is capable of testing

both scenarios. The idea behind these two loading scenarios is to verify if the transversal residual stresses at the Z-rails web-flange corner, which are tensile in its inner surface and compressive in its outer surface, affect differently on the Z-rails fatigue behavior.

It is concluded, through thoughtful trial and error, that a smooth steel actuator avoids fretting and local indentations on the rail's flange contact zone, which tend to lead to poor results and cracking at the flange, which is undesired. It is also concluded that a pin-joint connection between the loading device and the load cell, combined with testing through load control, allow two rails to be tested at the same time with independent fatigue life results, where an even load distribution is obtained for both rails, as well as a constant load during experiments. As presented, a strain gauge can be used as a crack detection method to evaluate and determine fatigue life of a specimen. Finally, the behavior of the Z-rail changes when an upward loading fatigue test is being conducted. To fix this issue, for this scenario, a steel plate is placed in between the steel load actuator and the Z-rail's flange, as well as a steel cover to clamp the Z-rail's web more effectively at the mid-span support. This mid-span support is also included to simulate the worst-case scenario of which the Z-rail is subjected to (when a shuttle wheel passes through the rails-upright bolted connection).

Overall, the development of the presented experimental setup for full scale fatigue tests on Z-rail specimens was a success, where this setup is able generate representative fatigue cracks on the Z-rail for both mentioned loading scenarios, which occur at the Z-rail's web-flange corner.

8.3.   Chapter 5

In Chapter 5, the procedures to simulate the cold roll-forming fabrication process to obtain the Z-rail with internal residual stresses are presented. The simulations are conducted based on the Finite Element Method, through the COPRA® software, a global leading specialized software for the simulation of the cold roll-forming fabrication process. A base FEA model for these simulations is defined and presented and further parametric studies are conducted on the roll-forming process.

The real roll-forming machine was referenced and replicated in COPRA® in order to simulate the manufacturing process as closely as possible. However, a very common simplification of the cold roll-forming fabrication process was used. This simplification consists in fixing the metal strip in space, impeding any rigid-body movements, while advancing the rolls towards the strip. With this simplification, the rolls do not actually roll, and the hard contact is considered frictionless.

Although a very common manufacturing process and widely used nowadays, the roll-forming process is hard to numerically simulate, where numerical convergence issues happen too often, and simulations are very time consuming.

In this chapter, a parametric study was presented in order to determine the optimal number of element layers to use in the meshing of the metal strip. It is concluded that 3 element layers is the ideal number of layers (even better than 4 elements layers, which was not expected).

A parametric study on isotropic versus kinematic hardening rules was also conducted and presented. It is concluded that some differences in residual stress results do arise, where using a kinematic hardening rule results in smoother stress values across the domain. However, when comparing residual stress results, both hardening rules present the same tendencies of higher absolute residual stress values in the bend-zones of the rail's section.

Two models were also compared in this chapter, a "full-length model", where the strip has twice the length of the intended rail's final length (a final load step to cut the rail in half is done in order to remove over deformed ends), and a "pre-cut model", where the strip already has the final desired length (the final load step to cut the rail is avoided). It is concluded that the lighter "pre-cut model" is much faster in terms of simulation times (2 days vs. 2 weeks, a huge advantage), but it is less numerically stable. It is also concluded that residual stress results are very similar between the two models, justifying the use of the lighter model.

Finally, in this chapter, a comparison between experimental and numerical residual stress results is presented. It is concluded that a decent match of transversal residual stress results is obtained for both procedures, considering the scatter in experimental results. However, the same cannot be said for longitudinal residual stress results. This can possibly be explained by the missing coiling and uncoiling effects in the numerical model. It is also stated that the inclusion of coiling and uncoiling effects is very hard, since the raw material is subjected to various coiling-uncoiling cycles. This number of cycles also varies considering if the strip is pre-coated or painted before the forming process. The industry is also not very clear on how many coiling-uncoiling cycles a regular strip goes through before the cold roll-forming fabrication process. Finally, it is stated that the transversal residual stresses are the most important ones in the study of the Z-rail's fatigue behavior, and again, these match well with experimental data.

8.4. Chapter 6

In Chapter 6, a stress analysis on the Z-rail was conducted and presented through a parametric study. With this analysis, mathematical equations where fitted to calculate the maximum value of the elastic maximum principal stresses that occur in the Z-rail's web-flange corner (where cracking appeared during experimental fatigue testing) when loaded through its flange. With these equations, one can use them very easily instead of simulating the downward or upward loading scenarios in a FEA program each time a design calculation is needed. It was shown that relative differences between using these equations and the stress results from Abaqus® are very minor (maximum of 2.5% and 1.5% for downward and upward loading scenarios, respectively).

In this chapter, a parametric study on the Z-rail's length was also conducted and presented. It was concluded that, for both downward and upward loading scenarios, a rail with a length (in between support holes) of 880 mm can be considered as a rail with "infinite length", i.e., the stresses are very little affected by increasing the rail's length (varying linearly due to the global deflection of the rail), however, the stresses are more sensitive to the decrease in the rail's length, increasing exponentially.

Finally, a parametric study on the Z-rail's web-flange corner radius and its thickness was conducted. It was concluded that stresses increase linearly by decreasing the web-flange corner radius. They also increase non-linearly (power curve) when decreasing the rail's thickness. A surface polynomial equation was also presented to account for these parameters. The use of this equation grants an average relative difference of 3.2% when comparing to FEA simulations.

8.5. Chapter 7

In Chapter 7, a fatigue analysis on the Z-rail was presented. In this chapter, two S-N curves were presented based on elastic maximum principal stress ranges. The first S-N curve was based on numerical simulations in Abaqus®, where the experimental fatigue testing setup was replicated as closely as possible. The second S-N curve was based on the presented mathematical equations from Chapter 6, which were obtained through simplified numerical models (point loads and simply fixed rail ends). These two mentioned S-N curves are very similar, proving the usefulness of the obtained equations from Chapter 6, which make the elastic stress range calculation much easier. It was also concluded that both S-N curves present higher slopes than the reference values from Eurocode 3. With the exception of one point, the S-N data fits in between the mean S-N curves with twice the standard deviation. The data also fits on the safe side of the Eurocode 3 class 160 MPa S-N curve. Finally, in the first S-N curve (elastic stress ranges obtained through numerical simulations), no real distinction can be made between an upward or a downward loading scenario, where fatigue behavior is more or less the same. But in the second S-N curve (elastic stress ranges obtained through the use of Chapter 6 equations) there is a slight difference between an upward and a downward loading scenario, where the downward loading scenario presents a higher slope and lower stress ranges, indicating that this loading scenario is the most damaging.

A Coffin-Manson fatigue life prediction was presented and compared to the experimental data. To have a good fatigue life prediction, all points in Figure 153 should fall in between a double-half band, which,

unfortunately, does not happen. However, all points, except one, fall on the safe side of the plot. This point that falls on the unsafe side is the point marked as "outlier" in the S-N data.

As shown in Appendix F, using elastoplastic stresses for the S-N curves is not recommended, since, during testing, the material plasticizes locally. On effect, the obtained data is arranged in a very horizontal trend ($m = 9.9$, which is arguably too high of a value). The coefficient of determination is also much worse ($R^2 = 0.38$). To account for this problem, elastic stress ranges should be considered. Alternatively, ε-N (strain vs. endurance) curves could be used instead. When computing stress ranges, maximum principal stress ranges where used since cracks developed in a perpendicular direction to the maximum principal stress, approximately. This is expected based on the basic concepts of Fracture Mechanics.

8.6.   Future Work

In the scope of this dissertation and the FASTCOLD project, some recommendations on future work/investigations is provided as follows:

- Update the fatigue analysis of the Z-rail with new Eurocode 3 evolutions. A current draft made available by the CEN Technical Committee 250 (CEN/TC250) aiming the revision of Eurocode 3 EN1993-1-9 states new detail categories with inverse slopes of $m = 5$, which would match better with the presented S-N curves on this dissertation;
- Further analyze and investigate the impact of other parameters (besides the ones already presented) in the stress analysis of the Z-rail;
- Analyze and compare results between cold roll-forming simulations with driving rolls and friction considerations and the presented simulations (no friction, strip is fixed in space with no rigid-body movements, and rolls move towards the strip without rolling);
- Include at least one coiling-uncoiling cycle to the numerical residual stress results, either through the mentioned closed-form analytical solution (Quach, Teng, & Chung, 2004) or through numerical simulations, and check if residual stress results match better with experimental ones;
- Further explore the local fatigue approach to evaluate the fatigue performance of Z-rails;
- Develop a methodology for fatigue design of Z-rails to incorporate in future Eurocode 3 revisions.

REFERENCES

ASTM E1049-85. (2017). Standard Practices for Cycle Counting in Fatigue Analysis. ASTM International, West Conshohocken, PA.

ASTM E739-91. (2004). Standard Practice for Statistical Analysis of Linear or Linearized Stress-Life (S-N) and Strain-Life (ε-N) Fatigue Data. ASTM International, West Conshohocken, PA.

Coffin, L. (1954). A Study of the Effects of Cyclic Thermal Stresses on a Ductile Metal. *The American Society of Mechanical Engineers Journal*, 76:931-50.

data M Sheet Metal Solutions GmbH. (2020). *COPRA RF Software - Roll Forming the Future*. Retrieved from https://www.copra.info/en/crf

De Jesus, A., Matos, R., Fontoura, B., Rebelo, C., Da Silva, L., & Veljkovic, M. (2012). A comparison of the fatigue behavior between S355 and S690 steel grades. *Journal of Constructional Steel Research*, 79:140-150.

EN1993-1-9. (2014). Eurocode 3: Design of steel structures - Part 1-9: Fatigue. European Committee for Standardization, Brussels.

FASTCOLD-RFCS. (2020). *FASTCOLD - Research Fund for Coal and Steel*. Retrieved from https://fastcold-rfcs.com/

Gülçeken, E., Abeé, A., Sedlmaier, A., & Livatyali, H. (2007). Finite Element Simulation of Flexible Roll Forming: A Case Study on Variable Width U Channel. *4th International Conference and Exhibition on Design and Production of Machines and Dies/Molds*.

Halmos, G. (2006). *Roll Forming Handbook.* Taylor & Francis.

Hosford, W. (2005). *Mechanical Behavior of Materials.* Cambridge University Press.

Kuna, M. (2012). *Finite Elements in Fracture Mechanics.* Springer.

Lindgren, M. (2013). *Workbook: COPRA® RF and COPRA® FEA RF.* data M Scandinavia AB.

Manson, S. (1954). Behavior of Materials Under Conditions of Thermal Stress. *NACA TN-2933. USA: National Advisory Committee for Aeronautics.*

Martins, A. (2018). Simulation of cold rolling process of steel profiles for shelter applications. *MSc. thesis, Faculty of Engineering of the University of Porto.*

Matsuishi, M., & Endo, T. (1968). Fatigue of metals subjected to varying stress. *Japan Society of Mechanical Engineering.*

Miner, M. (1945). Cumulative Damage in Fatigue. *Journal of Applied Mechanics*, vol. 12, no. 3, pp. A159-A164.

Quach, W., Teng, J., & Chung, K. (2004). Residual stresses in steel sheets due to coiling and uncoiling: a closed-form analytical solution. *Engineering Structures*, 26:1249-1259.

Schijve, J. (2008). *Fatigue of Structures and Materials.* Springer.

Souto, C. (2019). *Omicron - A Free Finite Element Analysis Software*. Retrieved from https://sites.google.com/view/omicron-fea/home

Souto, C., Correia, J., De Jesus, A., & Calçada, R. (2019). Fatigue Damage Tool (FDT) - A tool for fatigue damage assessment. *Procedia Structural Integrity*, 22:376-385.

APPENDIX A: Z-RAILS' STRAIN GAUGE DATA

For plotting purposes, strains where converted into stresses by the constitutive law presented in Equation A 1, where $E = 200$ GPa is the Young's modulus for the Z-rail's material (S355MC).

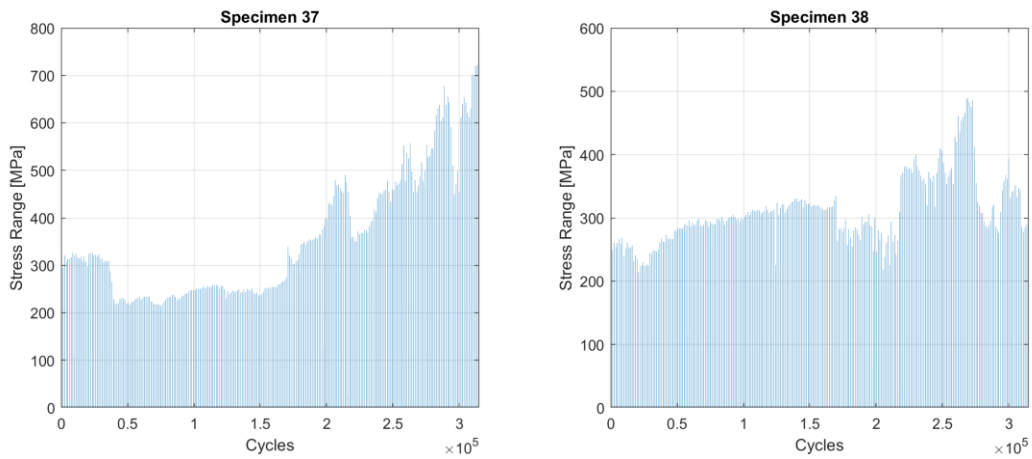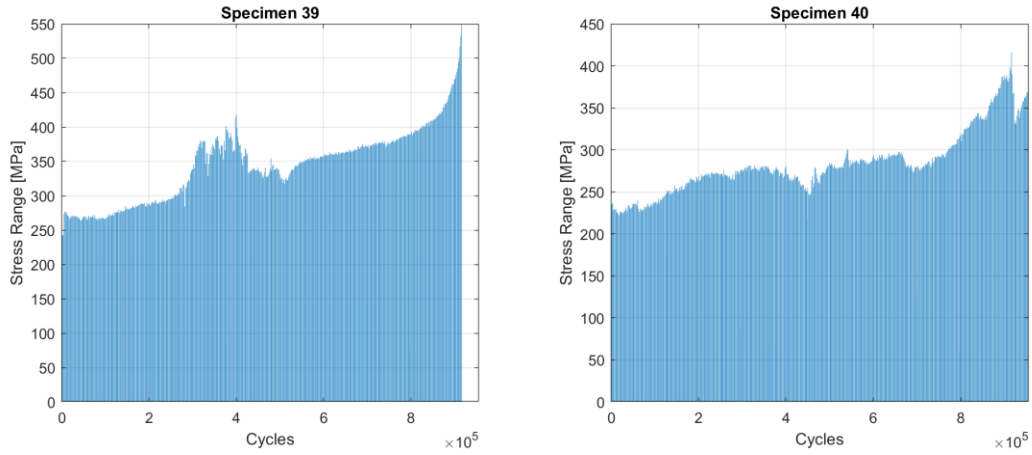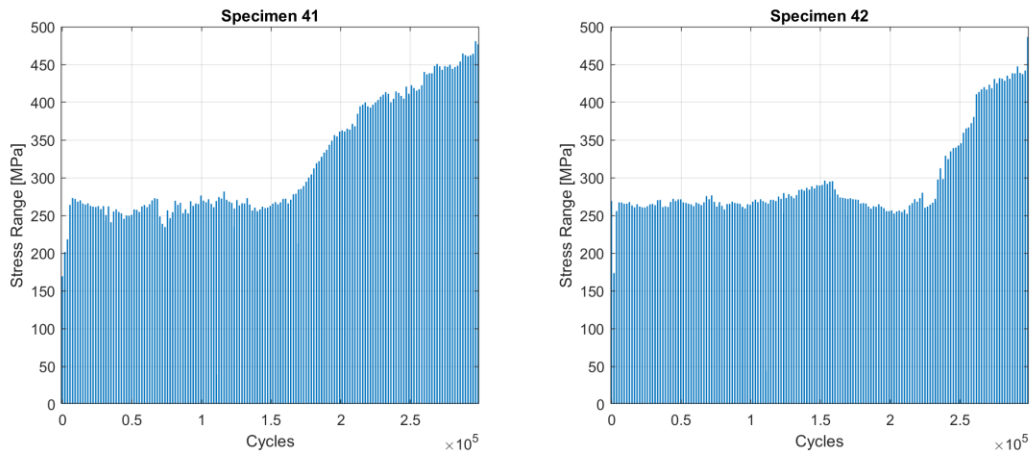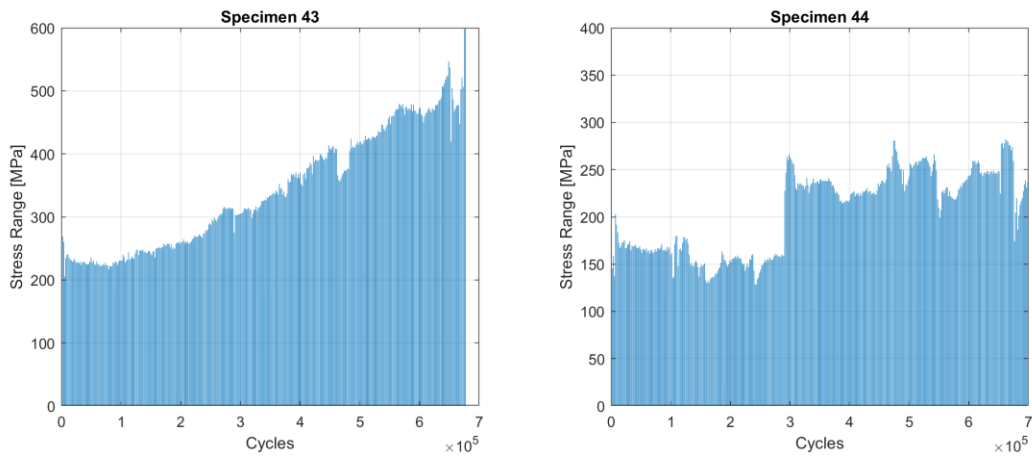$$\sigma = E \cdot \varepsilon$$

Equation A 1
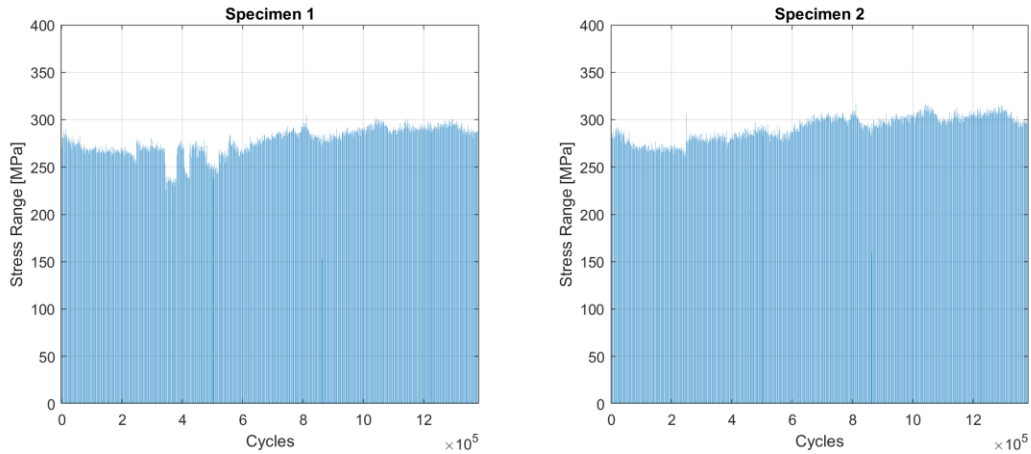
Figure A 1 - Strain gauge's data for specimens 1 and 2.
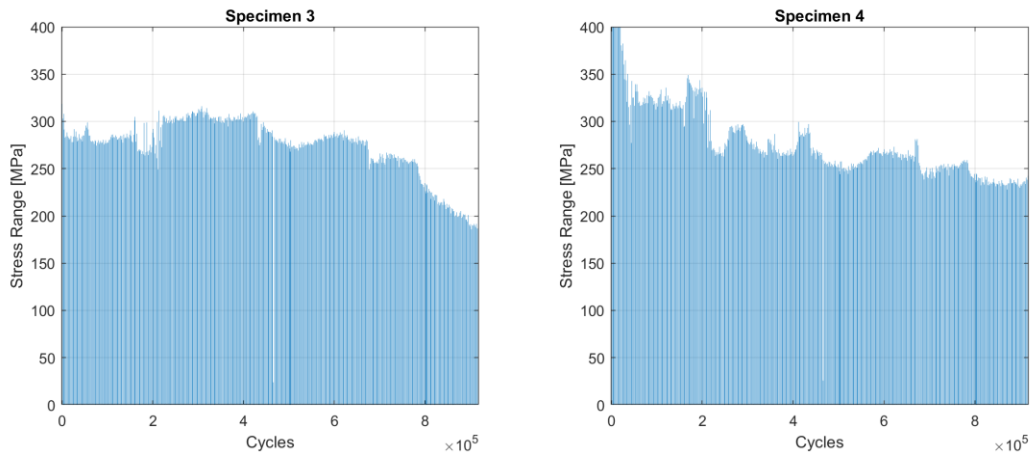
Figure A 2 - Strain gauge's data for specimens 3 and 4.
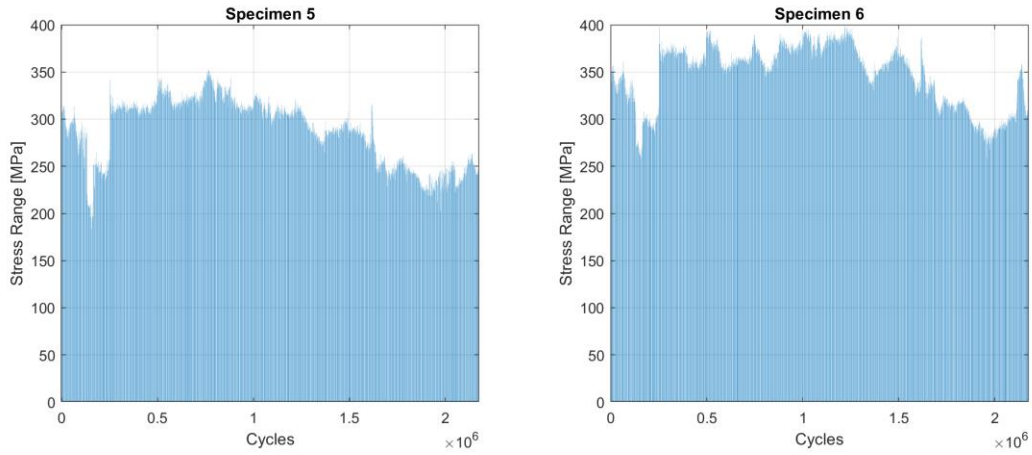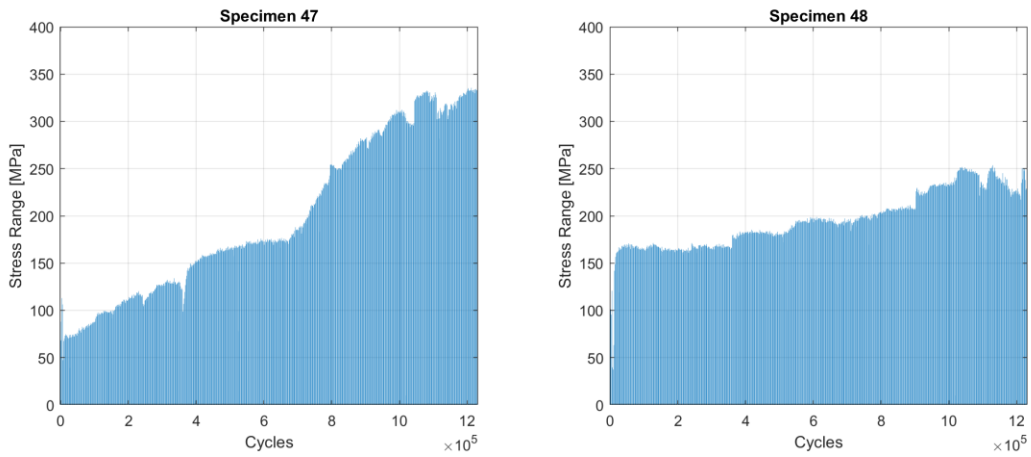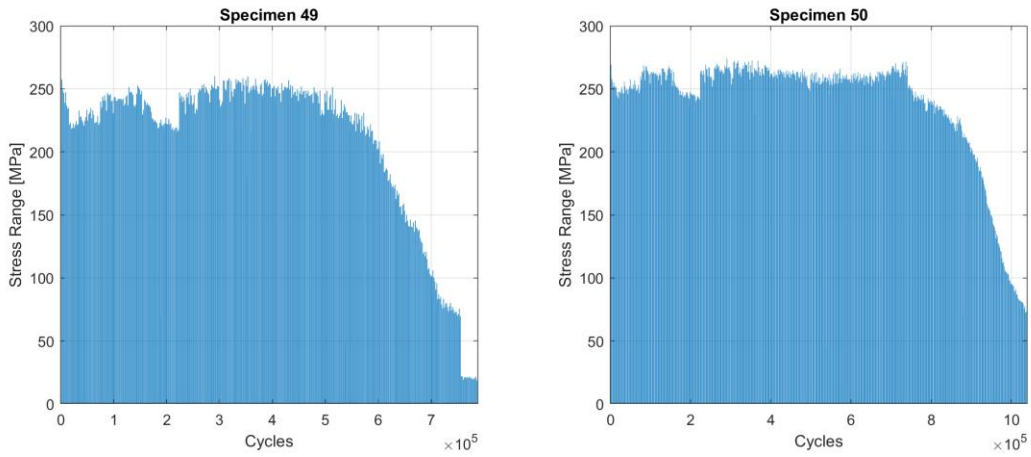
Figure A 3 - Strain gauge's data for specimens 5 and 6.
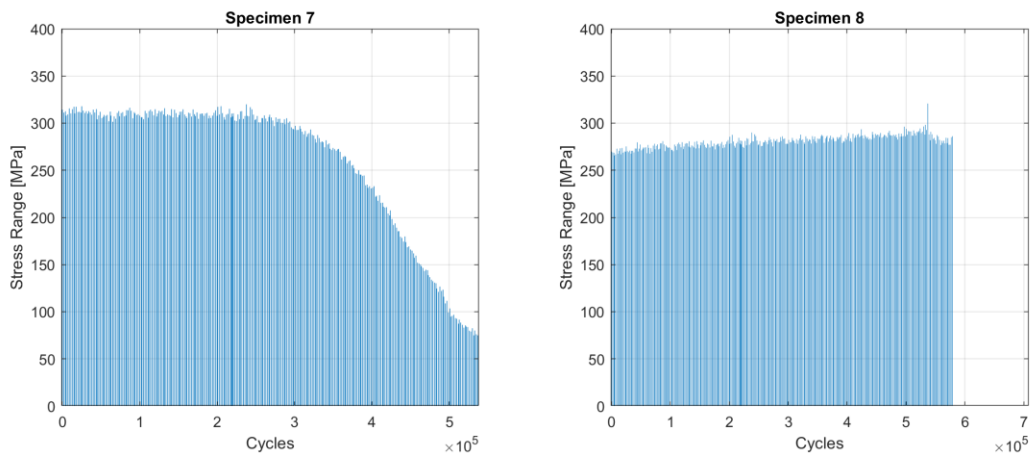
Figure A 4 - Strain gauge's data for specimens 7 and 8.
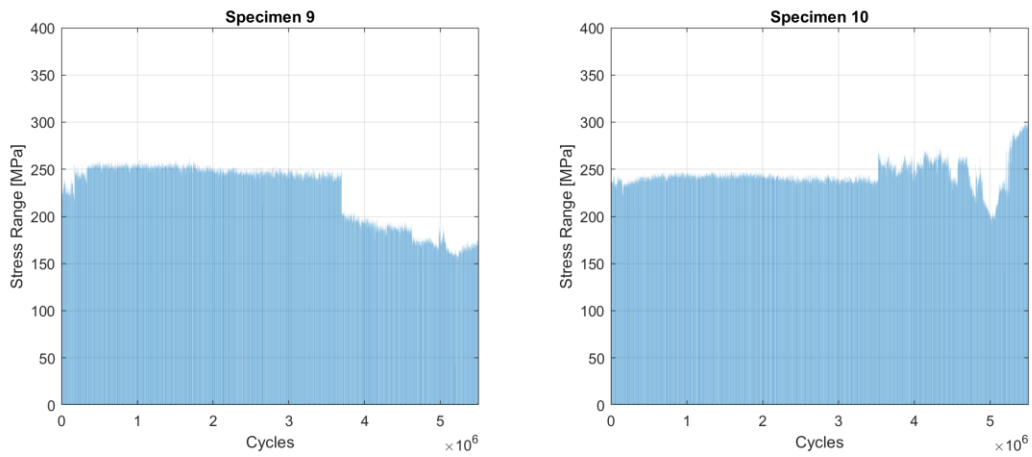
Figure A 5 - Strain gauge's data for specimens 9 and 10.
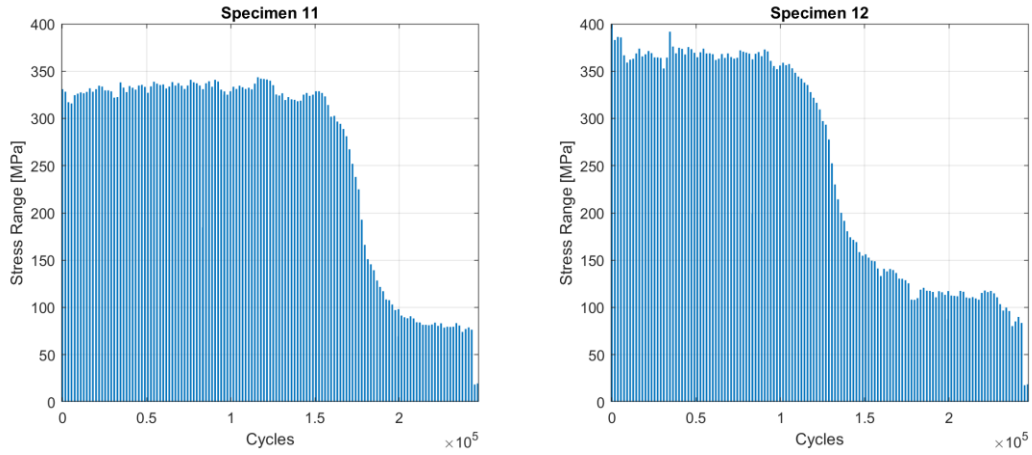
Figure A 6 - Strain gauge's data for specimens 11 and 12.
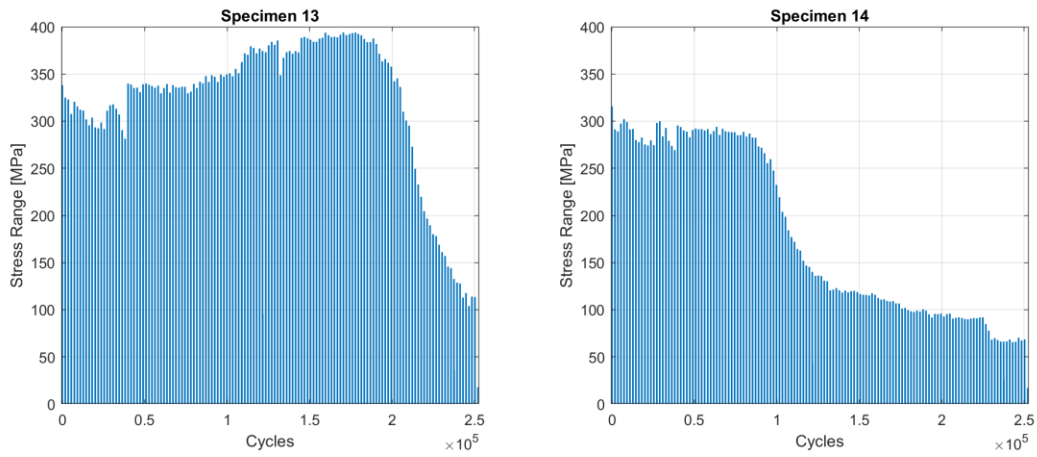
Figure A 7 - Strain gauge's data for specimens 13 and 14.
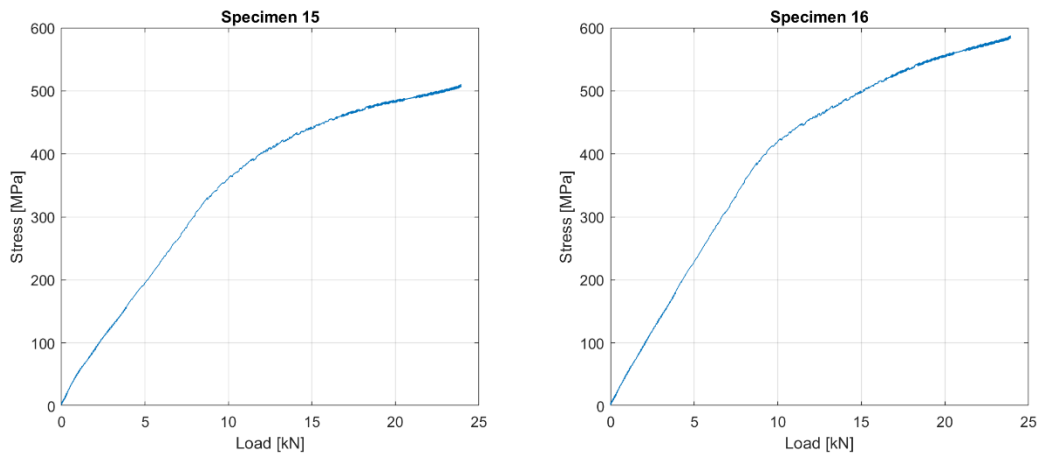
Figure A 8 - Strain gauge's data for specimens 15 and 16 (monotonic).
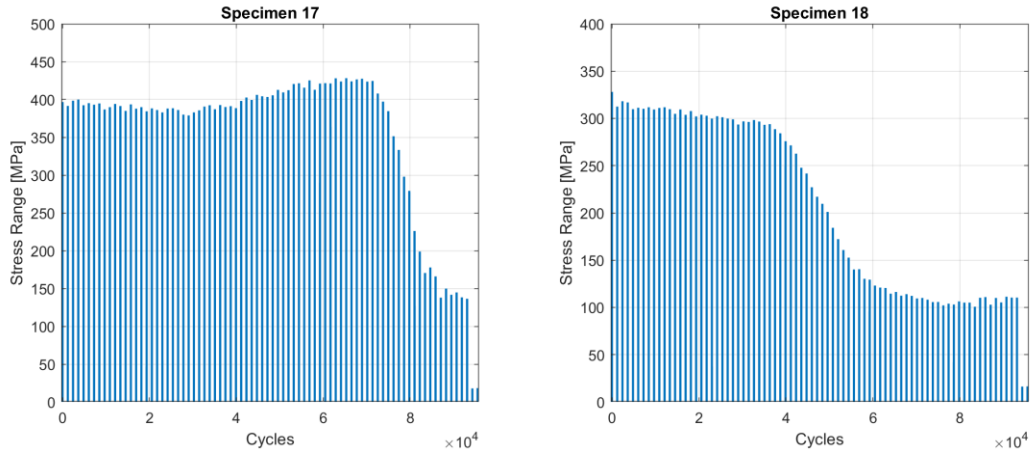
Figure A 9 - Strain gauge's data for specimens 17 and 18.
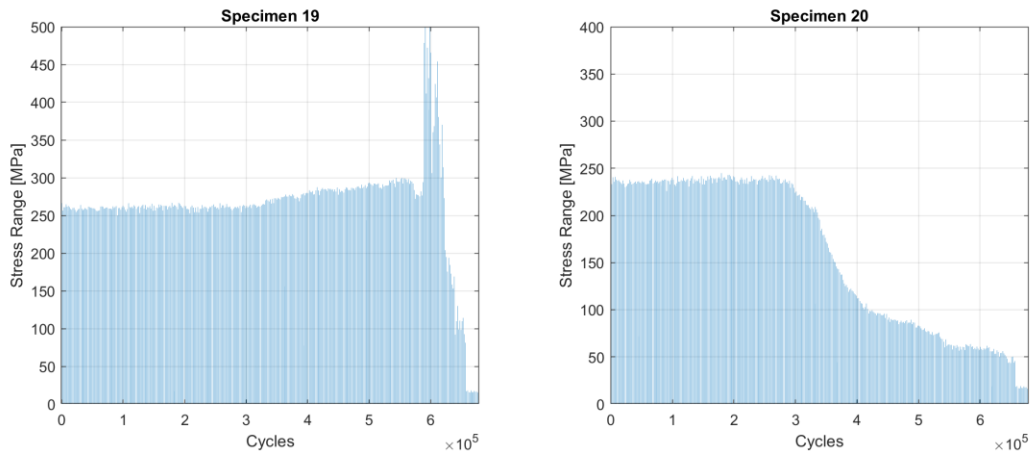
Figure A 10 - Strain gauge's data for specimens 19 and 20.
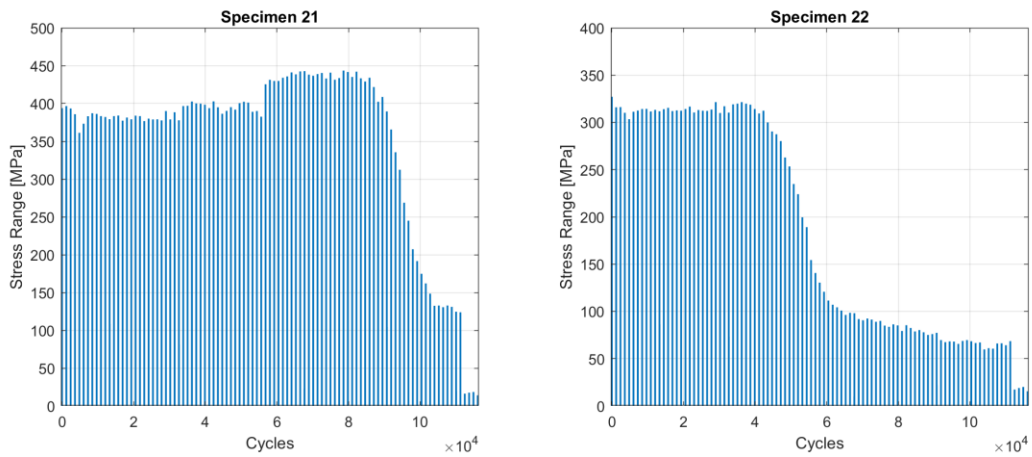
Figure A 11 - Strain gauge's data for specimens 21 and 22.
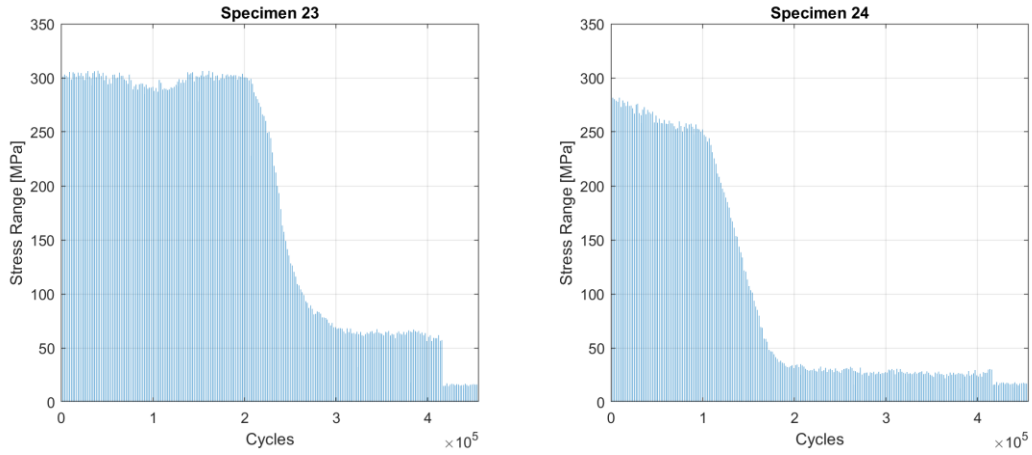
Figure A 12 - Strain gauge's data for specimens 23 and 24.
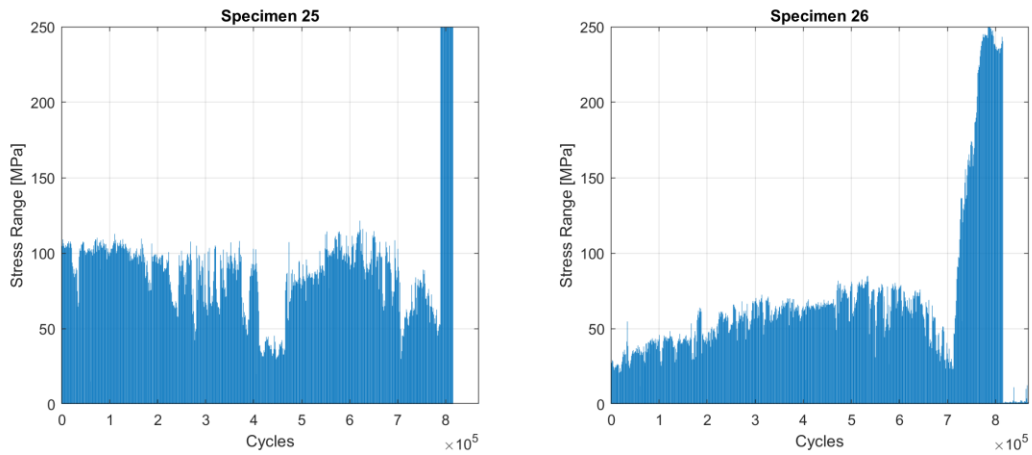
Figure A 13 - Strain gauge's data for specimens 25 and 26.
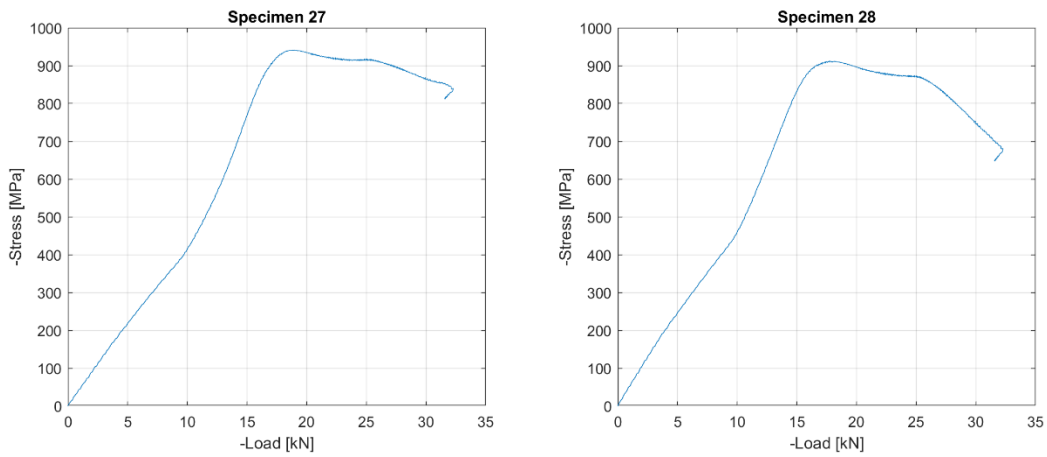
Figure A 14 - Strain gauge's data for specimens 27 and 28 (monotonic).
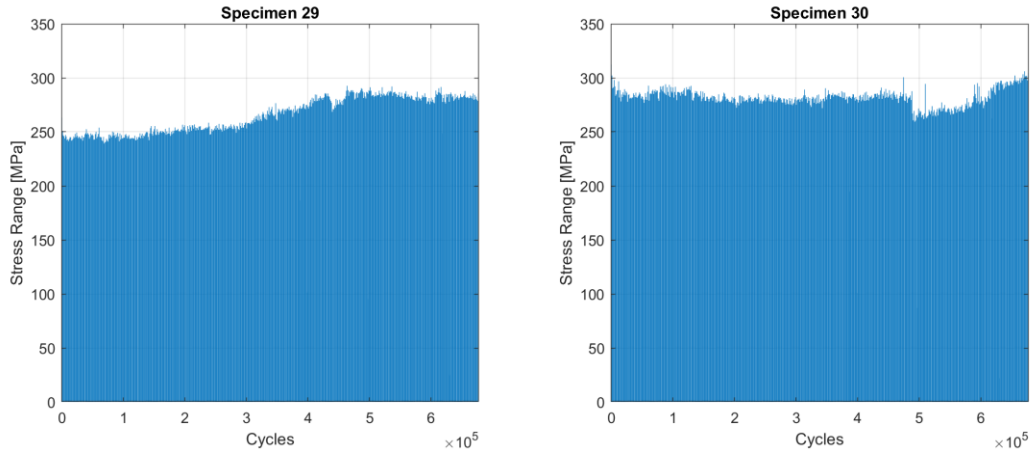
Figure A 15 - Strain gauge's data for specimens 29 and 30.
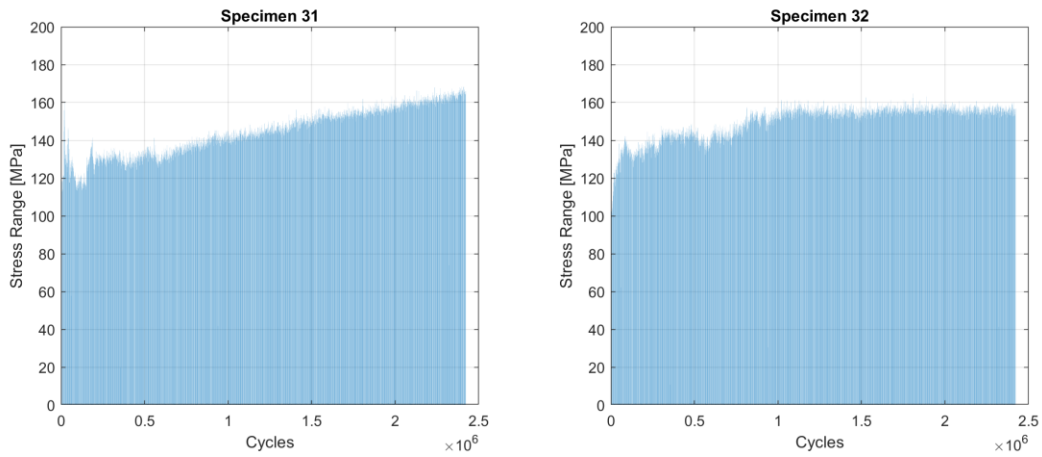
Figure A 16 - Strain gauge's data for specimens 31 and 32.
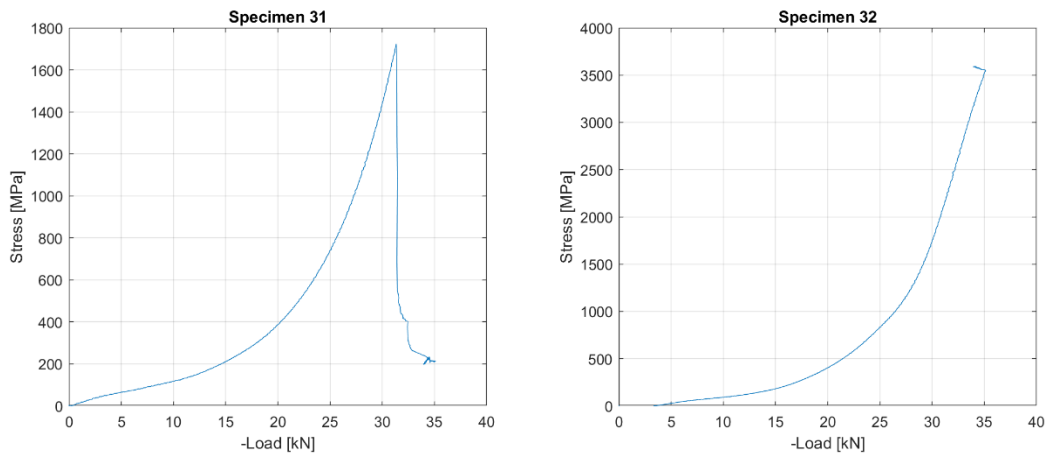
Figure A 17 - Strain gauge's data for specimens 31 and 32 (monotonic).

A-6
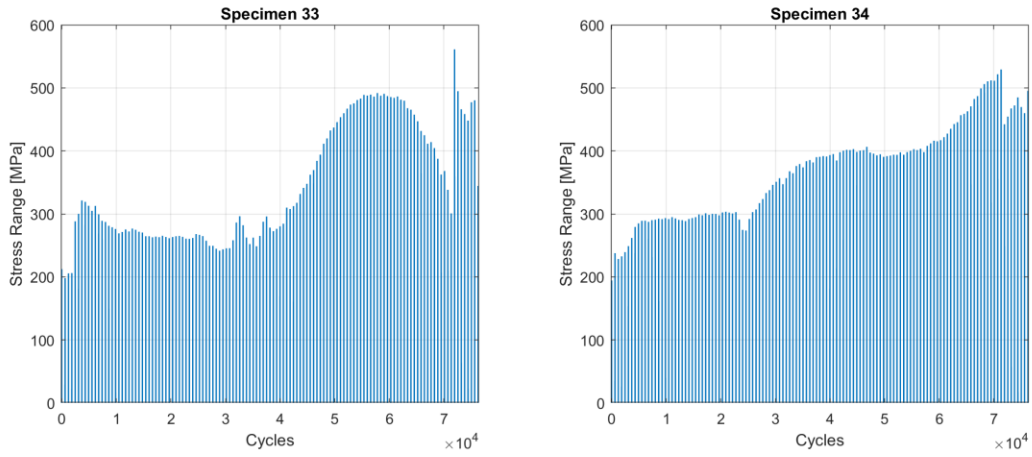
Figure A 18 - Strain gauge's data for specimens 33 and 34.
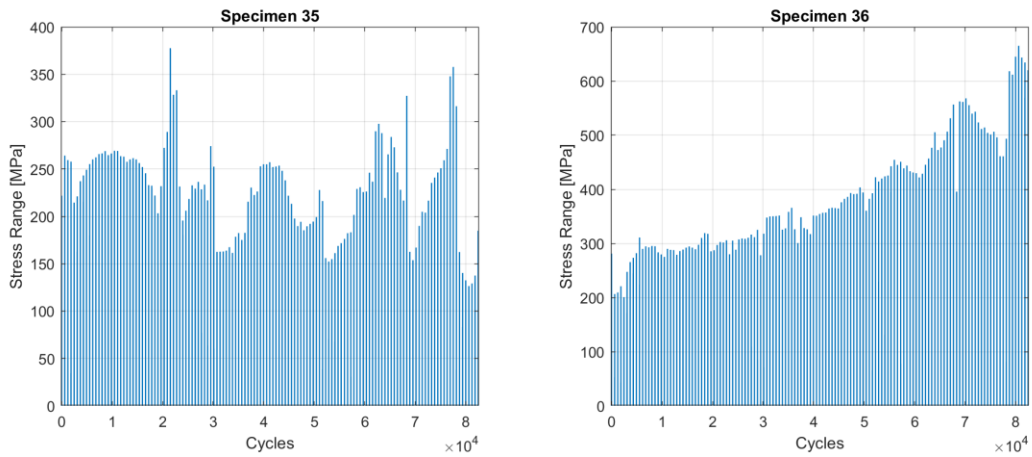
Figure A 19 - Strain gauge's data for specimens 35 and 36.

Figure A 20 - Strain gauge's data for specimens 37 and 38.

Figure A 21 - Strain gauge's data for specimens 39 and 40.

Figure A 22 - Strain gauge's data for specimens 41 and 42.

Figure A 23 - Strain gauge's data for specimens 43 and 44.
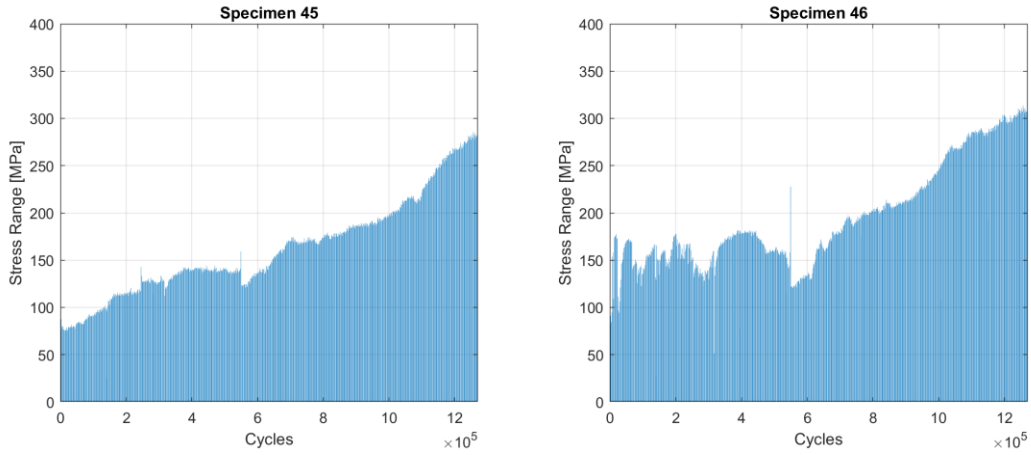
Figure A 24 - Strain gauge's data for specimens 45 and 46.

Figure A 25 - Strain gauge's data for specimens 47 and 48.

Figure A 26 - Strain gauge's data for specimens 49 and 50.

APPENDIX B: PHOTOGRAPHS OF THE RAIL SPECIMENS

Figure B 1 - Specimen 1 (bottom view).

Figure B 2 - Specimen 2 (bottom view).

Figure B 3 - Specimen 3 (bottom view).

Figure B 4 - Specimen 4 (top view).

Figure B 5 - Specimen 5 (bottom view).

Figure B 6 - Specimen 6 (bottom view).

Figure B 7 - Specimen 7 (top view).

Figure B 8 - Specimen 8 (top view).

Figure B 9 - Specimen 9 (top view).

Figure B 10 - Specimen 10 (top view).

Figure B 11 - Specimen 11 (top view).

Figure B 12 - Specimen 12 (top view).

Figure B 13 - Specimen 13 (top view).

Figure B 14 - Specimen 14 (top view).

Figure B 15 - Specimen 15 (monotonic).

Figure B 16 - Specimen 16 (monotonic).

Figure B 17 - Specimen 17 (top view).

Figure B 18 - Specimen 18 (top view).

Figure B 19 - Specimen 19 (top view).

Figure B 20 - Specimen 20 (top view).

Figure B 21 - Specimen 21 (top view).

Figure B 22 - Specimen 22 (top view).

Figure B 23 - Specimen 23 (bottom view).

Figure B 24 - Specimen 24 (top view).

Figure B 25 - Specimen 25 (top view).

Figure B 26 - Specimen 26 (top view).

Figure B 27 - Specimen 27 (monotonic).

Figure B 28 - Specimen 28 (monotonic).

Figure B 29 - Specimen 29 (bottom view).

Figure B 30 - Specimen 30 (bottom view).

Figure B 31 - Specimen 31 (top view).

Figure B 32 - Specimen 32 (top view).

Figure B 33 - Specimen 33 (top view).

Figure B 34 - Specimen 34 (top view).

Figure B 35 - Specimen 35 (top view).

Figure B 36 - Specimen 36 (top view).

Figure B 37 - Specimen 37 (top view).

Figure B 38 - Specimen 38 (top view).

Figure B 39 - Specimen 39 (top view).

Figure B 40 - Specimen 40 (top view).

Figure B 41 - Specimen 41 (top view).

Figure B 42 - Specimen 42 (top view).

Figure B 43 - Specimen 43 (top view).
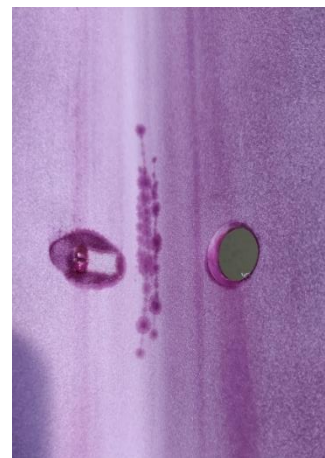
Figure B 44 - Specimen 44 (top view).
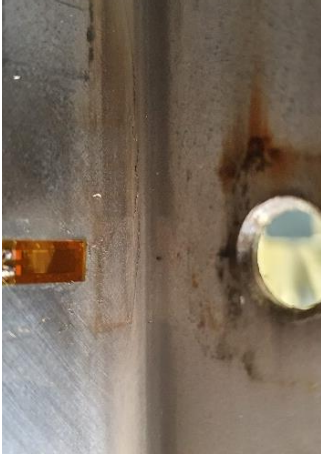
Figure B 45 - Specimen 45 (top view).

Figure B 46 - Specimen 46 (top view).

Figure B 47 - Specimen 47 (top view).

Figure B 48 - Specimen 48 (top view).

Figure B 49 - Specimen 49 (top view).

Figure B 50 - Specimen 50 (top view).

APPENDIX C: ROLL-FORMING MACHINE STATIONS
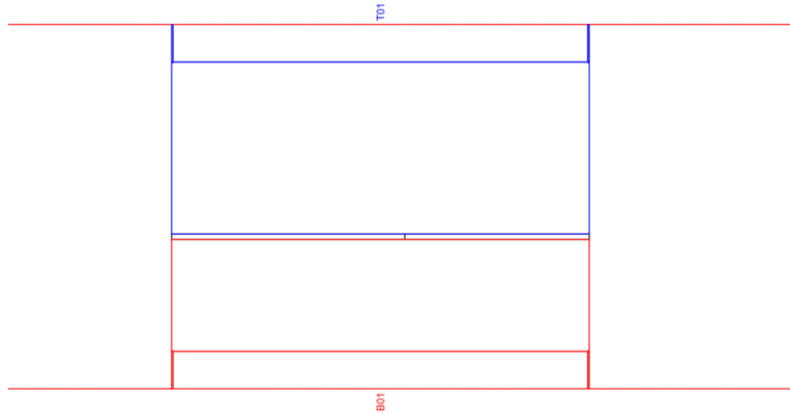
Figure C 1 - Station 1.
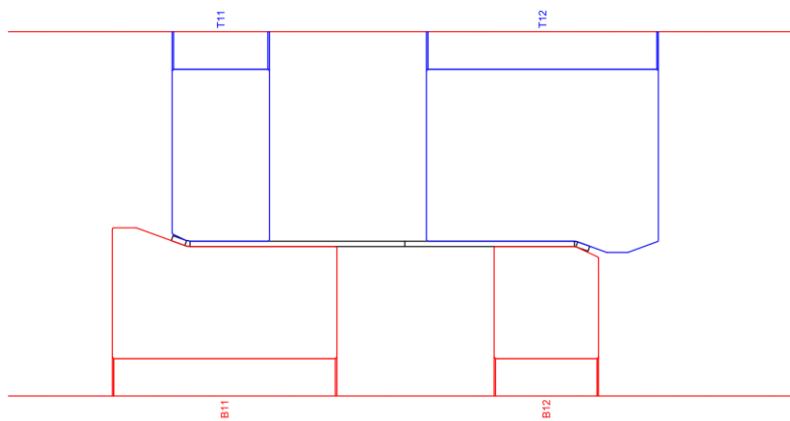
Figure C 2 - Station 2.
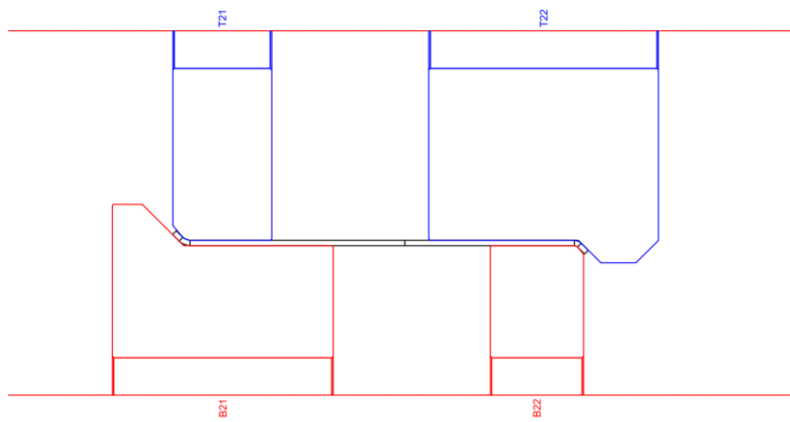
Figure C 3 - Station 3.
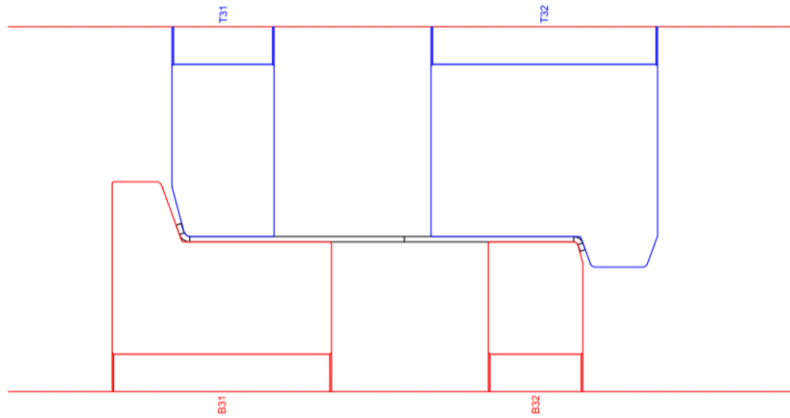
Figure C 4 - Station 4.
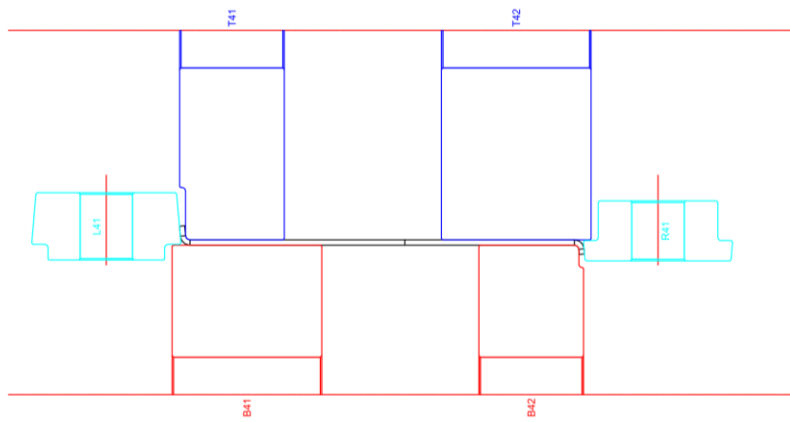
Figure C 5 - Station 5.
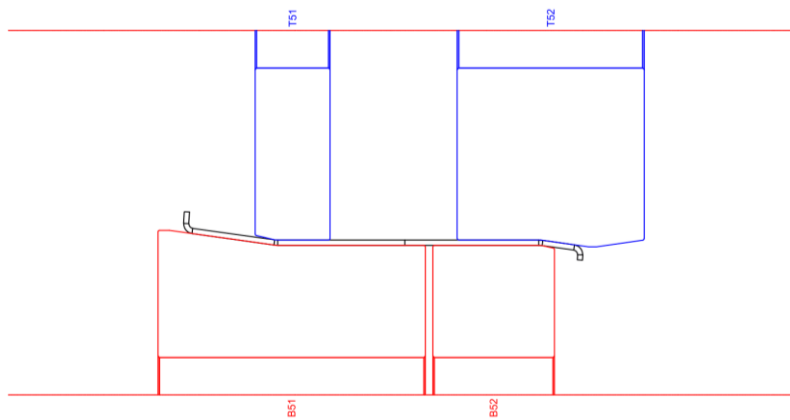
Figure C 6 - Station 6.
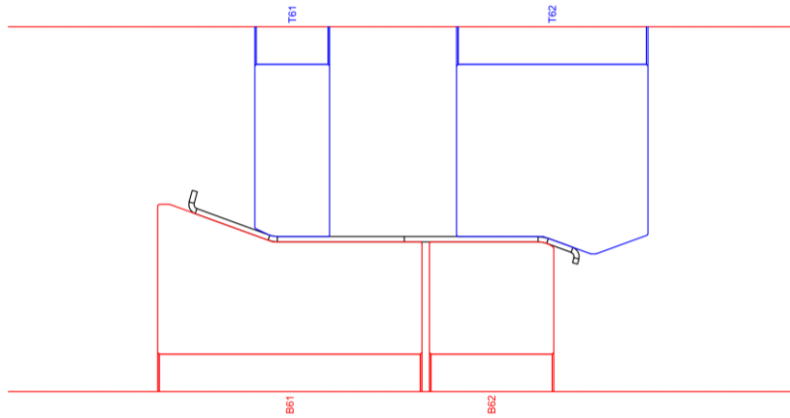
Figure C 7 - Station 7.
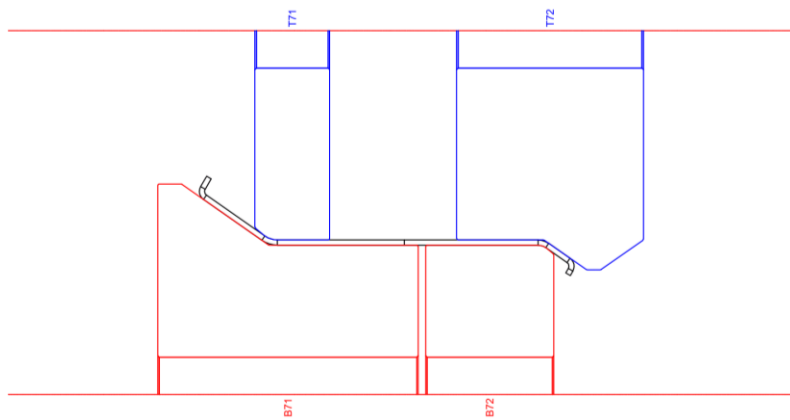
Figure C 8 - Station 8.
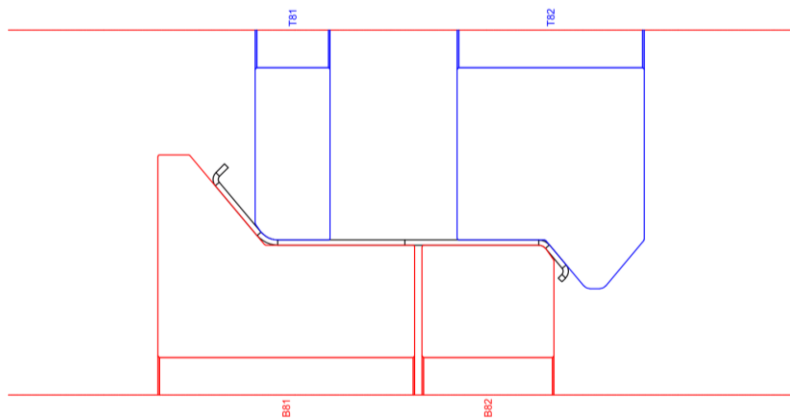
Figure C 9 - Station 9.
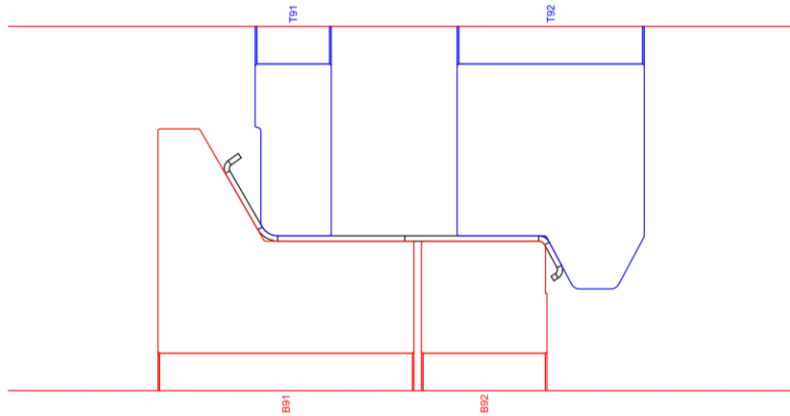
Figure C 10 - Station 10.
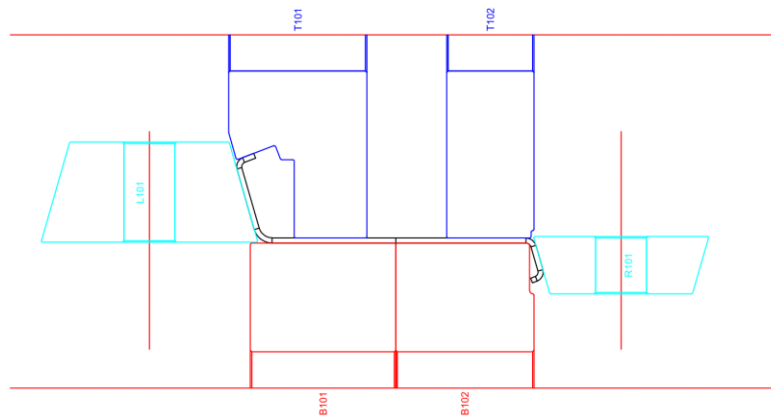
Figure C 11 - Station 11.
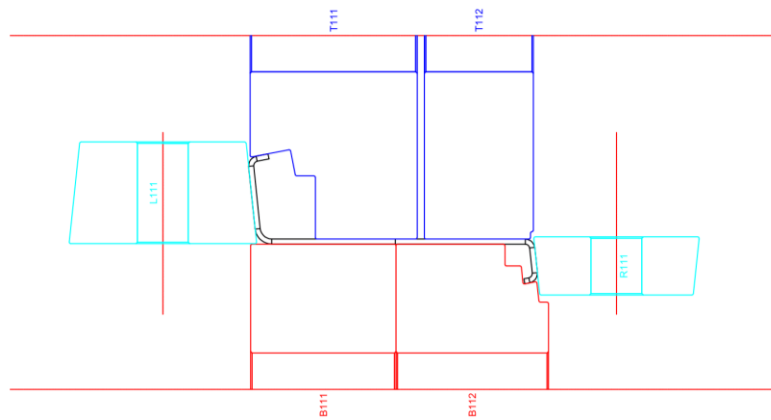
Figure C 12 - Station 12.
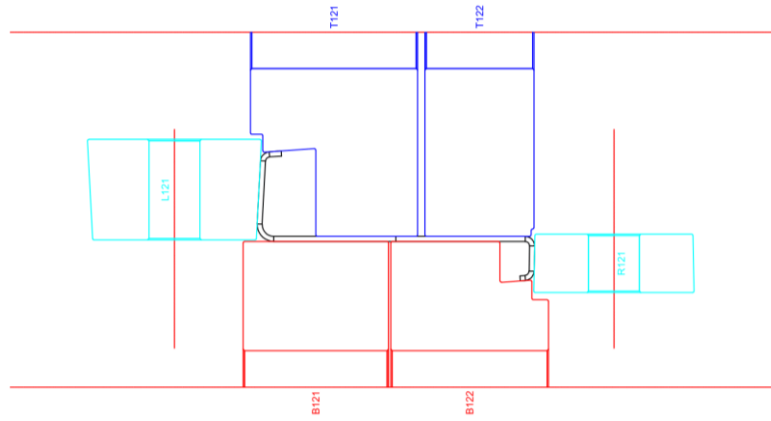
Figure C 13 - Station 13.
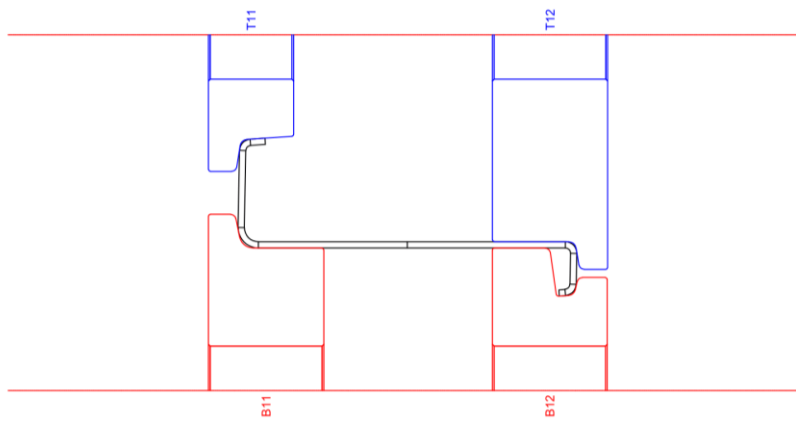
Figure C 14 - Station 14.
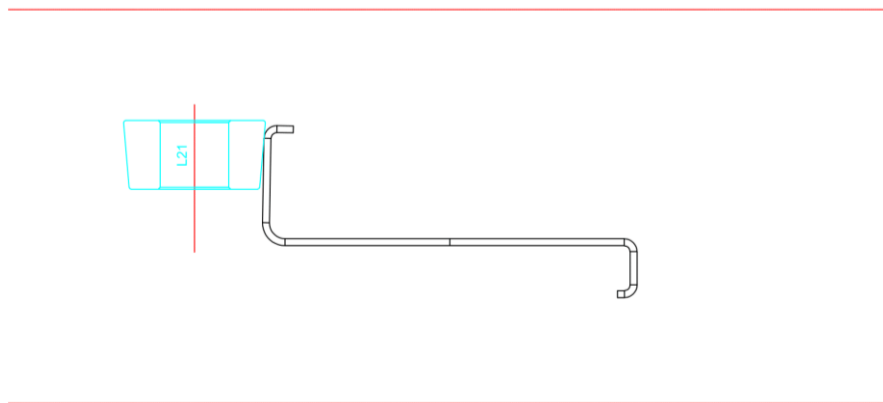
Figure C 15 - Station 15.
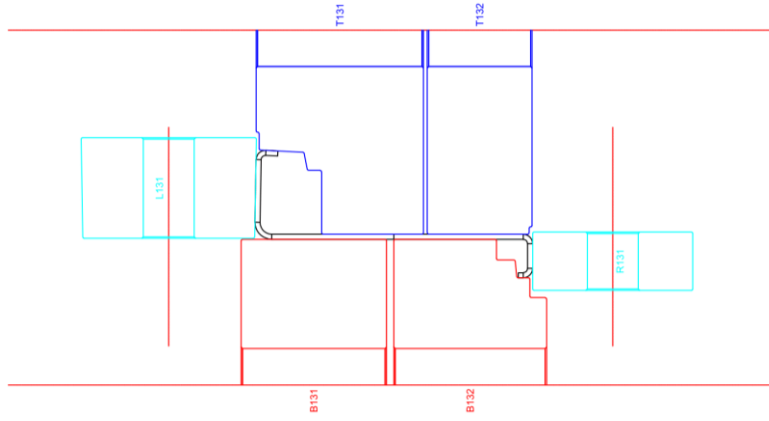
Figure C 16 - Station 16.
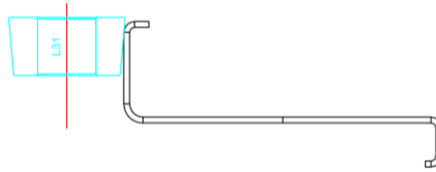
Figure C 17 - Station 17.
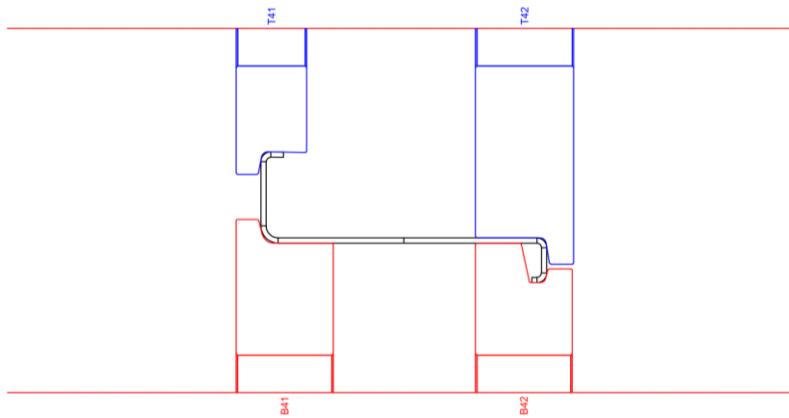
Figure C 18 - Station 18.

APPENDIX D: SIMULATIONS FOR S-N STRESS RANGES
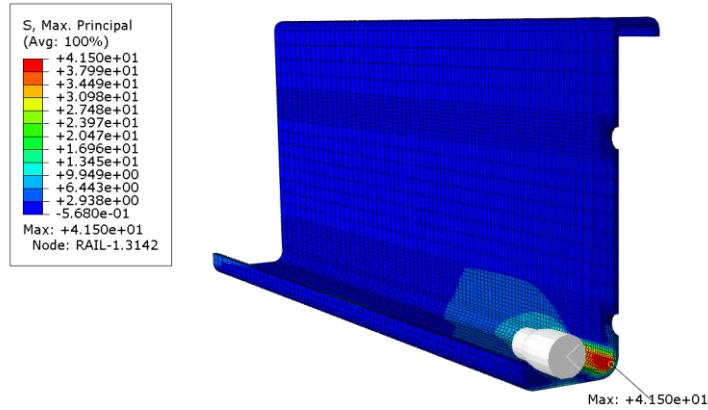
Figure D 1 - Downward loading scenario (500 N).
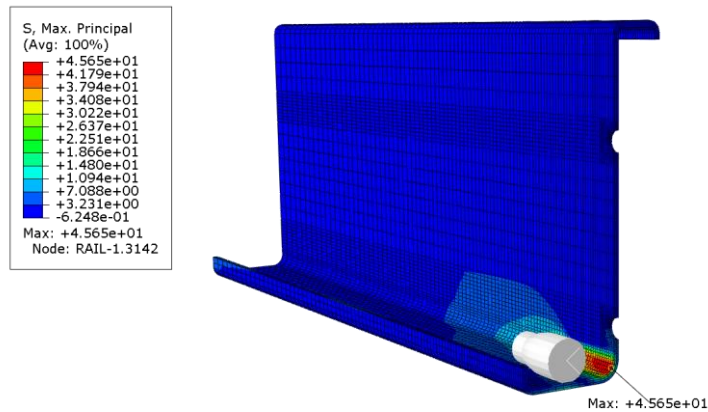
Figure D 2 - Downward loading scenario (550 N).
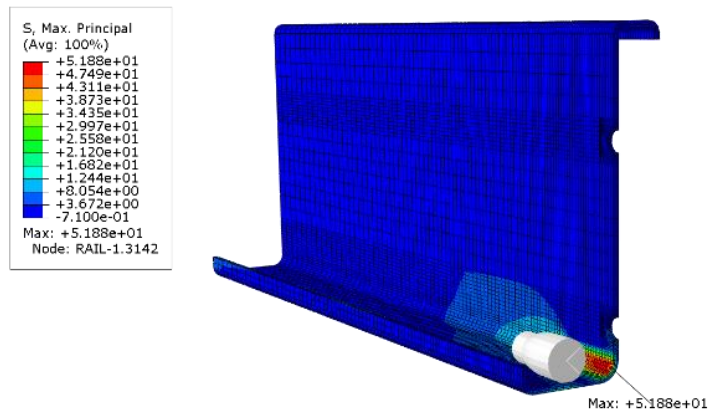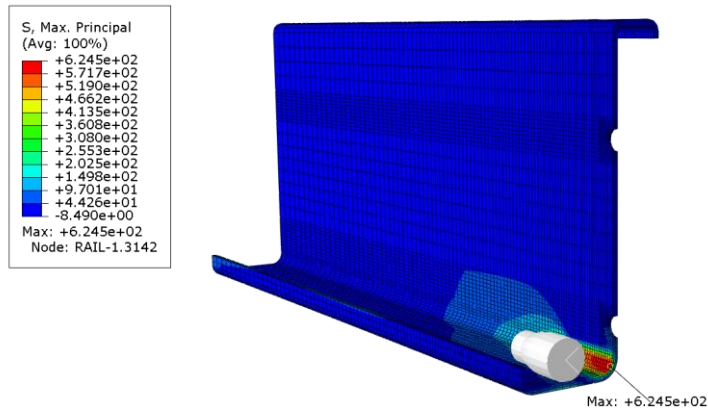

Figure D 3 - Downward loading scenario (625 N).
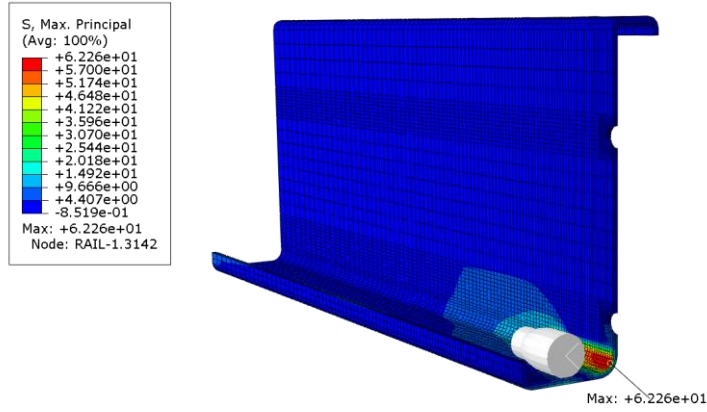
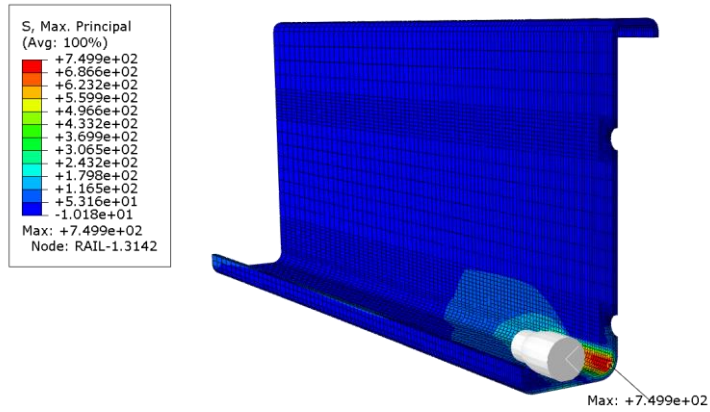**Figure D 4 - Downward loading scenario (750 N).**
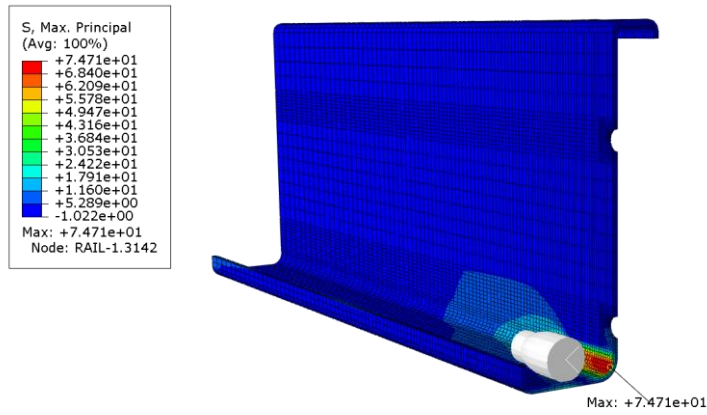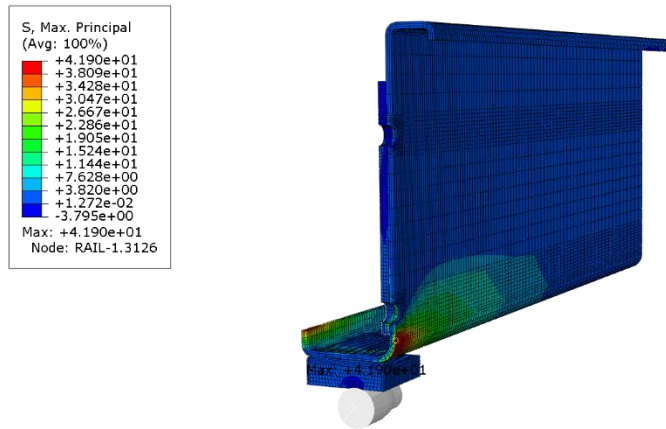

Figure D 5 - Downward loading scenario (900 N).
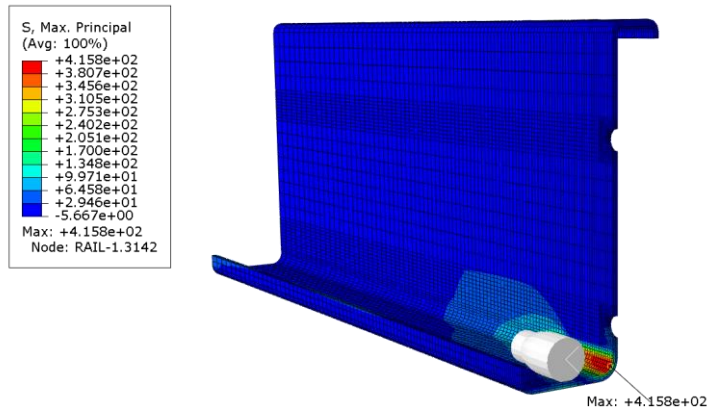
Figure D 6 - Downward loading scenario (5000 N).
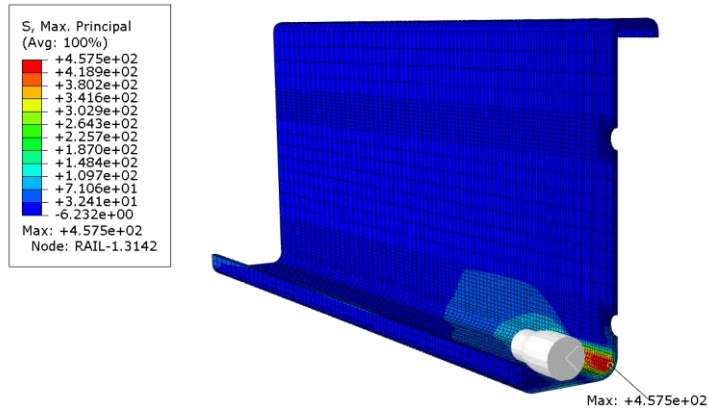
Figure D 7 - Downward loading scenario (5500 N).
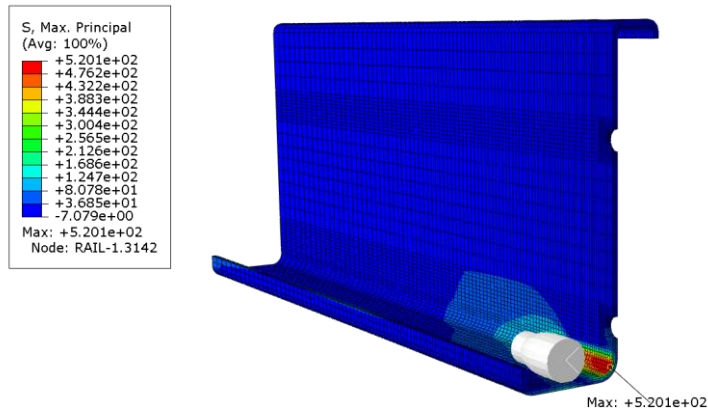
Figure D 8 - Downward loading scenario (6250 N).

Figure D 9 - Downward loading scenario (7500 N).

Figure D 10 - Downward loading scenario (9000 N).
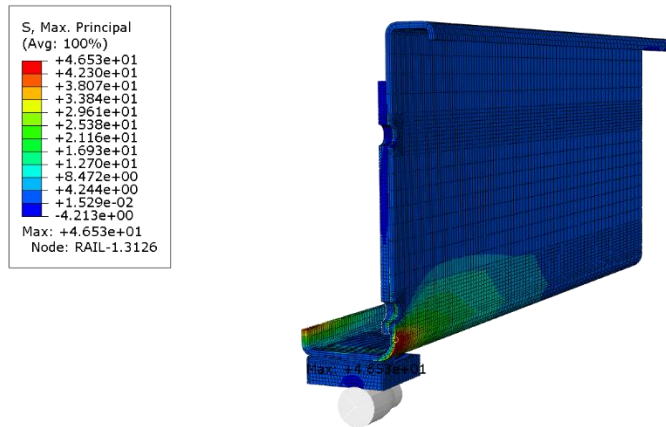

Figure D 11 - Upward loading scenario (900 N).

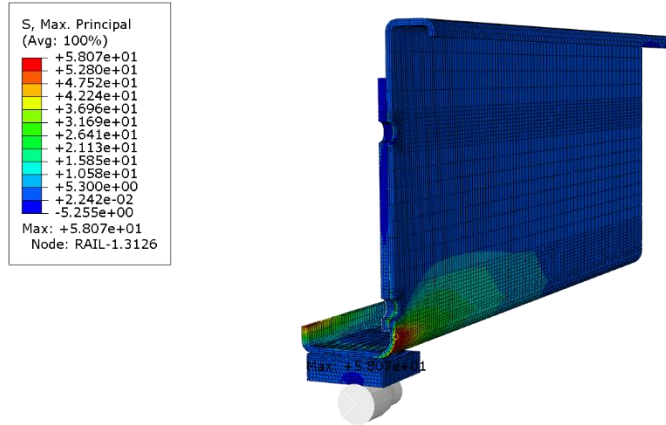**Figure D 12 - Upward loading scenario (1000 N).**

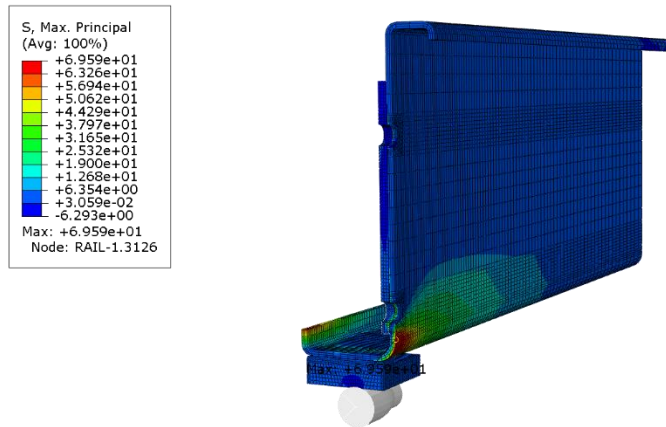**Figure D 13 - Upward loading scenario (1250 N).**
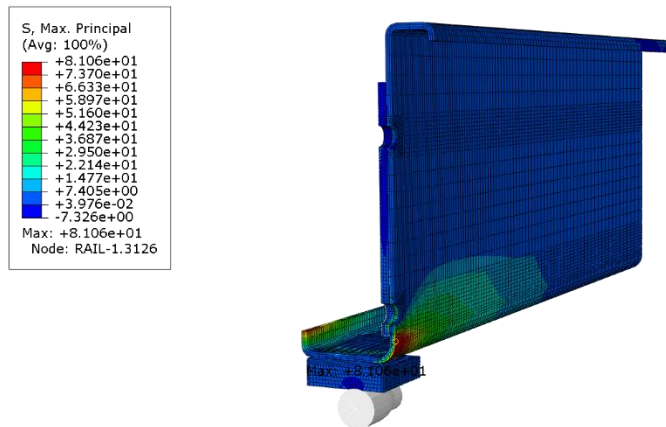

Figure D 14 - Upward loading scenario (1500 N).

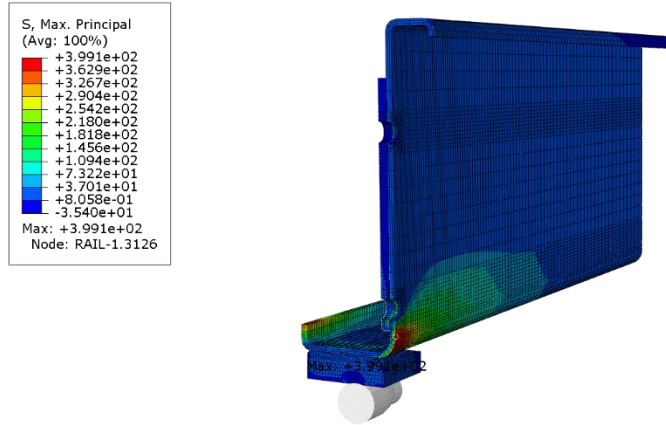**Figure D 15 - Upward loading scenario (1750 N).**

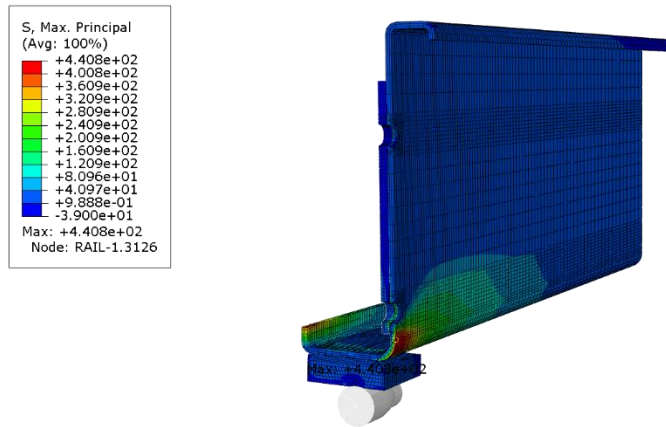**Figure D 16 - Upward loading scenario (9000 N).**

Figure D 17 - Upward loading scenario (10000 N).
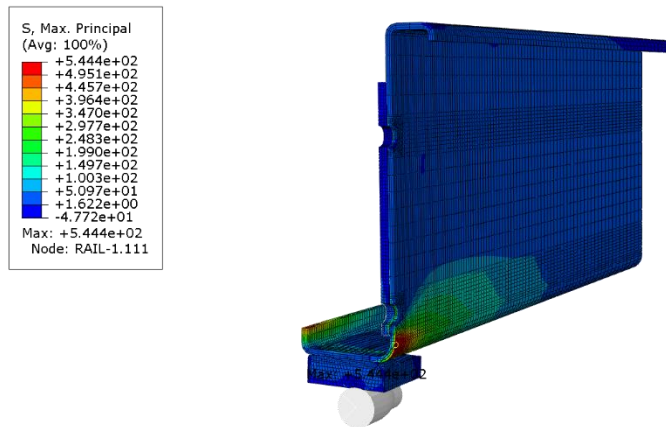

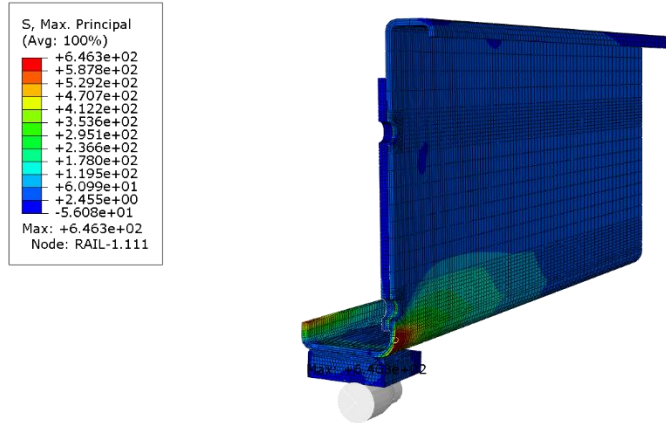**Figure D 18 - Upward loading scenario (12500 N).**

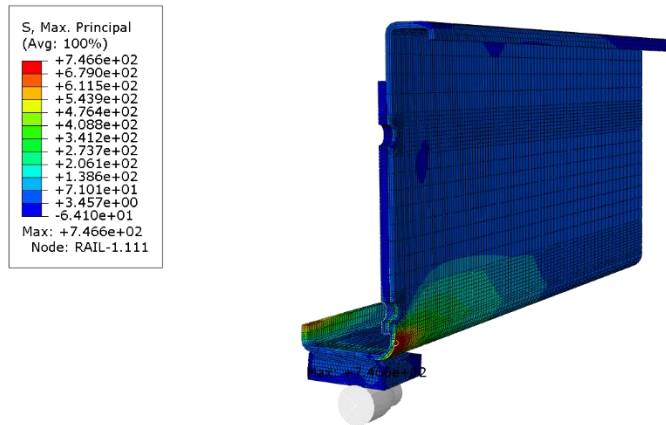**Figure D 19 - Upward loading scenario (15000 N).**

Figure D 20 - Upward loading scenario (17500 N).

APPENDIX E: NEWTON-RAPHSON METHOD TO SOLVE THE COFFIN-MANSON EQUATION - MATLAB®

```matlab
% ------------------------------------------------------------------ %
% Vectorized Newton-Raphson Method to Solve the Coffin-Manson Equation %
% ------------------------------------------------------------------ %
%    By: Carlos Daniel Santos Souto                                  %
% Email: csouto@fe.up.pt                                             %
% ------------------------------------------------------------------ %
clear; clc; close all;

% Material constants
E  = +200000; % [MPa]
sf = +952.20; % [MPa]
ef = +0.7371; % [mm/mm]
b  = -0.0890;
c  = -0.6640;

% Numerical data: strain range [mm/mm]
de = [0.001430, 0.001430, 0.001430, 0.001430, 0.002729, 0.002729, 0.002729, ...
      0.002729, 0.003596, 0.003596, 0.002060, 0.002060, 0.003596, 0.003596, ...
      0.002060, 0.002060, 0.001679, 0.001679, 0.002123, 0.002123, 0.005564, ...
      0.005564, 0.005564, 0.005564, 0.004332, 0.004332, 0.003043, 0.003043, ...
      0.004332, 0.004332, 0.003043, 0.003043, 0.002358, 0.002358, 0.002358, ...
      0.002358]';

% Numerical data: mean stress [MPa]
sm = [473.45, 473.45, 473.45, 473.45, 498.74, 498.74, 498.74, 498.74, ...
      517.27, 517.27, 485.68, 485.68, 517.27, 517.27, 485.68, 485.68, ...
      478.40, 478.40, 333.02, 333.02, 447.42, 447.42, 447.42, 447.42, ...
      432.99, 432.99, 422.29, 422.29, 432.99, 432.99, 422.29, 422.29, ...
      361.38, 361.38, 361.38, 361.38]';

% Coffin-Manson equation (function handle)
f = @(Nf) (sf - sm)/E.*(2*Nf).^b + ef*(2*Nf).^c - de/2;

% Numerical derivative of the Coffin-Manson equation
h  = +1.0E-06;
df = @(Nf) (f(Nf + h) - f(Nf - h))/(2*h);

% Find the solutions using the Newton-Raphson method
initial_guesses = ones(size(de))*1000.0;
results = newton_raphson(initial_guesses, f, df);

% Plot roots (results)
x = linspace(+1.0E+03, +1.0E+06, 1000);
figure(1);
hold on;
plot(x, f(x), 'HandleVisibility', 'off');
```

```matlab
scatter(results, f(results), '.k', 'DisplayName', 'Roots');
hold off;
xlim([+1.0E+03, +1.0E+06]);
ylim([-2.0E-03, +2.0E-03]);
grid on;
legend show;
set(gca, 'XScale', 'log');

% Vectorized Newton-Raphson method
function x1 = newton_raphson(x0, f, df)
        maxit = 1000;     % maximum number of iterations (stopping criteria #1)
        tol   = +1.0E-15; % tolerance to assume zero     (stopping criteria #2)
        for i = 1:1:maxit
                x1 = x0 - f(x0)./df(x0);
                if norm(f(x1)) < tol
                        break
                else
                        x0 = x1;
                end
        end
        disp(['Used iterations: ', num2str(i), ' out of ', num2str(maxit)]);
end
```
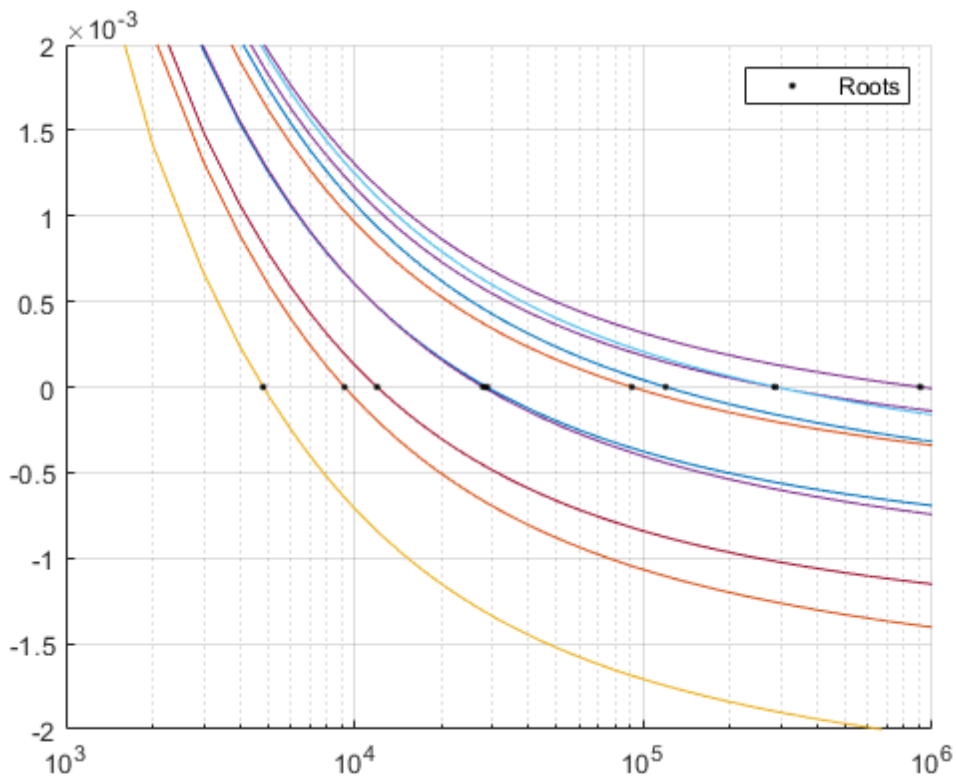
Used iterations: 13 out of 1000

Figure E 1 - Obtained roots for the multiple Coffin-Manson equations.

APPENDIX F: S-N CURVE BASED ON ELASTOPLASTIC FEA

In Chapter 7 of this dissertation, an S-N fatigue design curve based on experimental lifetimes and stress ranges computed through elastic FEA was presented:
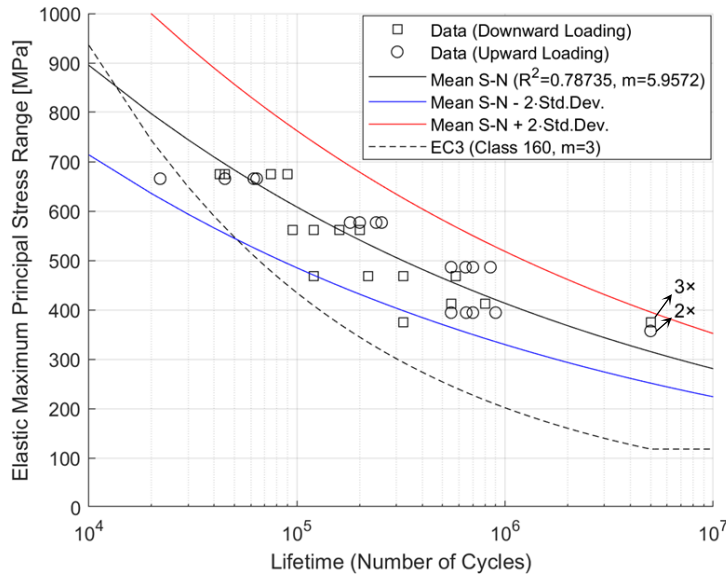

Figure F 1 - S-N fatigue design curve based on experimental lifetime and stress ranges computed through elastic FEA.

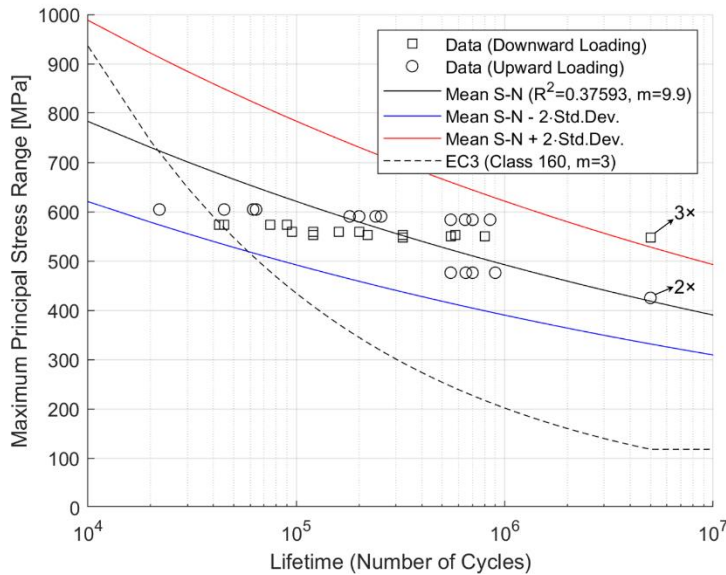Now, including material plasticity considerations, the S-N fatigue design curve is the following:

Figure F 2 - S-N fatigue design curve based on experimental lifetime and stress ranges computed through elastoplastic FEA.